Nanowire Magnetic Force Microscopy

Inauguraldissertation

zur Erlangung der Würde eines Doktors der Philosophie

vorgelegt der
Philosophisch-Naturwissenschaftlichen Fakultät
der Universität Basel

von

Hinrich Mattiat

Basel, 2023

Genehmigt von der Philosophisch-Naturwissenschaftlichen Fakultät auf Antrag von

Prof. Dr. Martino Poggio
Erstbetreuer/in

Prof. Dr. Richard Warburton
Zweitbetreuer/in

Dr. Thomas Mühl.
Externe/r Experte/in

Basel, den 20. Juni 2023

Prof. Dr. Marcel Mayor
Dekan/in

Abstract

Local imaging of surface stray fields on the nanoscale is fundamental for understanding magnetism. With advancements in fabrication techniques a plethora two-dimensional magnetic materials are now readily available. By design they call for ultrasensitive imaging techniques, since their reduced volume leads to relatively weak magnetic stray fields. One of the established magnetic imaging technique on the nanoscale is magnetic force microscopy (MFM). It employs micron-sized cantilevers as mechanical force transducers and offers the desired spatial resolution. However, it is lacking in terms of field sensitivity. Additionally, conventional MFM cantilever tips contain a considerable amount of hard magnetic material and hence can quickly disturb the subtle magnetization of weak magnetic samples.

This project focuses on improving the field sensitivity by employing nanowires (NWs) as magnetic force microscopy probes. Free standing NWs in the pendulum geometry naturally present themselves as extremely sensitive mechanical force sensors. Their high aspect ratios and low masses immediately lead to thermally limited force sensitivities of at least two orders of magnitude better than those of standard MFM cantilevers. In order to achieve magnetic imaging contrast we make use of focused electron beam induced deposition (FEBID) of cobalt, resulting either in a fully magnetic NW or a magetic tip on top of an existing structure.

We find that the magnetic image formation for a sufficiently long cylindrical Co tip can be approximated by a simple point-pole model, where only the magnetic surface charge at the free extremity of the tip needs to be considered. As a consequence the NWs' frequency shifts are proportional to the in-plane magnetic field gradients. In terms of field sensitivity the best characterized sensor achieves a value slightly better than $2\,\mathrm{nT}/\sqrt{\mathrm{Hz}}$ at resonance.

These results present a significant improvement in field sensitivity and pave the way for ultrasensitive magnetic stray field and dissipation imaging at the nanoscale.

Contents

Figures and Tables

List of Figures

List of Tables

Introduction

Imaging has always been at the heart of science, fostering understanding of the previously inaccessible. The advent of the atomic force microscope (AFM), first demonstrated in 1986 by Binnig et al. [1] as an advancement of the scanning tunneling microscope (STM) [2], gave researches a tool to study surfaces and surface interactions with unprecedented sensitivity and lateral resolution. In AFM a mechanical cantilever is used to transduce forces and force gradients arising from the interaction between a sharp tip and the sample surface to measurable deflections or a changes in the dynamic properties, while the tip is rastered across the sample, creating a two-dimensional image. A natural extension of the AFM is the use of magnetic tips, inviting magnetic contrast formation as first demonstrated by Martin and Wickramasinghe [3] in 1987. Magnetic force microscopy (MFM) has since become an indispensable experimental technique to study magnetic thin films and their domain structures. Inherent challenges in interpreting MFM data include the disentanglement between topographic and magnetic signal, the possibility of sample and tip mutually influencing their magnetization states during a measurement, and that the observed contrast highly depends on the specific magnetization of a given tip. However, a lot of work has been put into understanding the exact mechanisms of magnetic contrast formation, resulting in different tip models [4–6] and calibration procedures [7–9] which deal effectively with most of the issues mentioned above and allow, within limits, for a quantitative explanation of the stray field data.

One aspect of standard MFM that can be improved is its sensitivity to magnetic field. Feng et al. recently presented MFM cantilevers with an estimated sensitivity of around $80\,\mu T/\sqrt{Hz}$ [10]. Our approach to push this number by at least one order of magnitude is to employ nanowire (NW) resonators as magnetic force sensors [11]. A typical NW-MFM probe consists of a NW with a length of about 10 to 25 µm and a diameter of 50 to 250 nm. Additionally it needs to be magnetically functionalized in order to attain the ability to probe magnetic stray fields. The main improvement lies in the lower mass of a NW and its high aspect ratio, offering a favorable scaling in terms of the quantities influencing the ultimate force sensitivity. Spring constants of typical NW probes are in the range of a few $mN\,m^{-1}$ instead of a few $N\,m^{-1}$ as for standard AFM/MFM cantilevers, yielding force sensitivities of a few $aN/\sqrt{Hz}$ instead of a few hundred $aN/\sqrt{Hz}$. There are a few differences between NW-MFM compared to the standard AFM techniques. For example the sensor will be operated in the pendulum geometry with the tip oscillating in parallel to the sample surface instead of perpendicularly as is standard in AFM/MFM, also avoiding that the softer NW snaps into contact with the surface. This way we probe in-plane force gradients along two orthogonal directions as compared to the out-of-plane force gradient.

The first NW probe demonstrating exquisite sensitivity to magnetic field gradients of

$11\,\mathrm{mT/m}\sqrt{\mathrm{Hz}}$ at resonance was demonstrated in our lab by Rossi et al. [12] and consisted of a GaAs NW with an MnAs tip. The next generation of sensors are made of fully magnetic Co NWs 3D-printed by focused electron beam induced deposition (FEBID) [13] and is presented in Section 3.1. Their sensitivity to magnetic fields at resonance amounts to $3\,\mathrm{nT}/\sqrt{\mathrm{Hz}}$ and is comparable with competing ultra-sensitive magnetic scanning probe techniques such as scanning superconducting quantum interference device[1] (SQUID) [14] or scanning nitrogen-vacancy (NV) center[2] [15]. In an effort to further improve the field sensitivity we turned to state of the art NW force sensors [16] and equipped them with Co FEBID tips in a bid to approach pico-tesla sensitivities. A first prototype of these latest generation probes will be characterized in Section 3.2 and hopefully pave the way to a new versatile and robust platform in the field of ultra-sensitive, high-resolution magnetic scanning probe microscopy.

[1] $5\,\mathrm{nT}/\sqrt{\mathrm{Hz}}$
[2] $100\,\mathrm{nT}/\sqrt{\mathrm{Hz}}$

1. Theory

In this chapter we will derive the basic theory necessary to understand nanowire magnetic force microscopy. At first the mode shape is found via Euler-Bernoulli beam theory. Afterwards we discuss force sensing and the application to magnetic fields, investigating the magnetic imaging contrast and different tip models for the tip magnetization. The last part is dedicated to measurement of dissipation.

1.1. Nanowire mechanics

1.1.1. Euler-Bernoulli beam theory

The deflection of a singly clamped beam of length L can be described by Euler-Bernoulli beam theory which assumes that shear deformation and rotational inertia can be neglected [18]. In order to derive the Euler-Bernoulli beam equation we follow the book *Vibration of continous systems* by S. S. Rao [19] using the variational approach. Figure 1.1 shows a bent element of a beam which is subject to a transverse force per unit length $f(x,t)$ along the z-axis. $w(x,t)$ is denoting the beams deflection away from the equilibrium position along the x-axis. Considering how point P is displaced to point P' we can define the axial deformation u in the small angle limit by noticing that the cross-section is bent with a slope $\partial w/\partial x$ with respect to the normal direction. Then u is given by

$$u = -z\frac{\partial w}{\partial x}. \tag{1.1}$$

under the assumptions that its length by far exceeds the cross section and that deflections are small. We can write down expressions for the axial strain and stress acting on the beam segment as follows

$$\epsilon_x = \frac{\partial u}{\partial x} = -z\frac{\partial^2 w}{\partial x^2} \tag{1.2}$$

$$\sigma_x = E\epsilon_x = -Ez\frac{\partial^2 w}{\partial x^2} \tag{1.3}$$

where E is the Young's modulus. All other elements of the strain and stress tensors are considered to be zero. The *strain energy density* of the deformed beam element is then

$$\pi_0 = \frac{1}{2}\sigma_x\epsilon_x = \frac{1}{2}Ez^2\left[\frac{\partial^2 w}{\partial x^2}\right]^2 \tag{1.4}$$

Integrating over the whole beam yields the *strain energy* as follows

$$\pi = \int_V \pi_0 \mathrm{d}V = \frac{1}{2}\int_0^L EI(x)\left[\frac{\partial^2 w}{\partial x^2}\right]^2 \mathrm{d}x \tag{1.5}$$

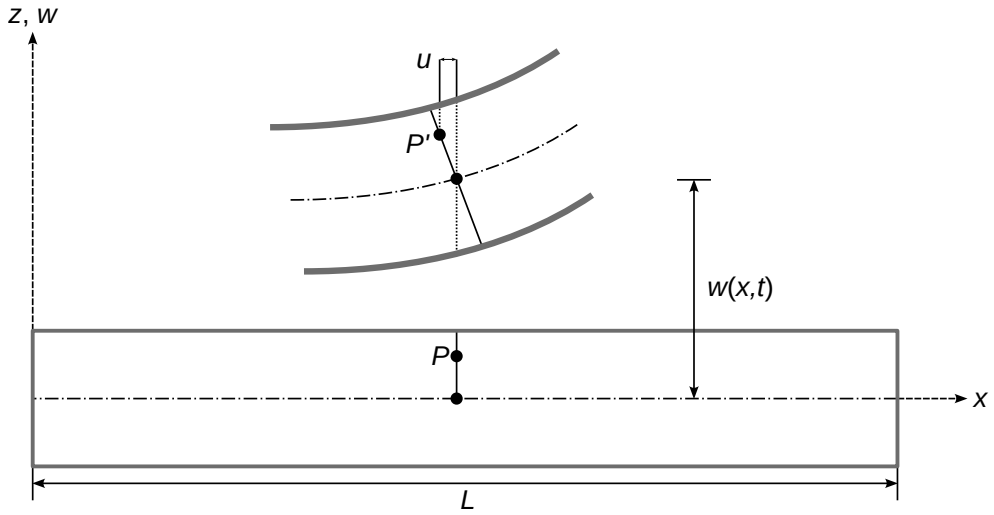

Figure 1.1. – Singly clamped beam
Figure adapted from [17].

with the *area moment of inertia*[1] of the beam cross section $A(x)$

$$I(x) = \int_A z^2 \mathrm{d}A(x). \tag{1.6}$$

Now that we know the strain energy of the system we need to derive expressions for the kinetic energy and the work applied by the force action on the beam of length L. The kinetic energy can be written as

$$\mathcal{T} = \frac{1}{2} \int_0^L m(x) \left[\frac{\partial w(x,t)}{\partial x} \right]^2 \mathrm{d}x \tag{1.7}$$

with the mass per unit length $m(x) = \rho A(x)$ and the mass density ρ. The work by the applied force can be denoted as

$$\mathcal{W} = \int_0^L f(x,t) w(x,t) \, \mathrm{d}x. \tag{1.8}$$

Applying Hamilton's principle, stating that the variation with respect to time of the Lagrangian vanishes, yields

$$\delta \int_{t_1}^{t_2} [\mathcal{T} - \pi + \mathcal{W}] \, \mathrm{d}t = 0. \tag{1.9}$$

[1] For a cylinder with radius R and constant cross section along x we find $I = \frac{1}{2}\pi R^4$

Computing all variations with respect to w and its derivatives using integration by parts multiple times finally leads to

$$\int_{t_1}^{t_2} \left\{ -\int_0^L m\frac{\partial^2 w}{\partial t^2}\delta w \; dx - EI\frac{\partial^2 w}{\partial x^2}\delta \left[\frac{\partial w}{\partial x}\right]\Big|_0^L + \frac{\partial}{\partial x}\left[EI\frac{\partial^2 w}{\partial x^2}\right]\delta w\Big|_0^L \right. \\ \left. -\int_0^L \frac{\partial^2}{\partial x^2}\left[EI\frac{\partial^2 w}{\partial x^2}\right]\delta w \; dx + \int_0^L f \; \delta w \; dx \right\} \mathrm{d}t = 0. \tag{1.10}$$

Comparing terms of the same order yields the equation of motion and two general boundary conditions

$$\frac{\partial^2}{\partial x^2}\left[EI\frac{\partial^2 w}{\partial x^2}\right] + m\frac{\partial^2 w}{\partial t^2} - f = 0, \quad 0 < x < L \tag{1.11}$$

$$EI\frac{\partial^2 w}{\partial x^2}\delta\left[\frac{\partial w}{\partial x}\right]\Big|_0^L = 0 \tag{1.12}$$

$$\frac{\partial}{\partial x}\left[EI\frac{\partial^2 w}{\partial x^2}\right]\delta w\Big|_0^L = 0. \tag{1.13}$$

The boundary conditions in equations (1.12) and (1.13) are fulfilled in a number of cases. Relevant here are the conditions for or the fixed end of the beam where

$$w = 0, \quad \left[\frac{\partial w}{\partial x}\right] = 0, \tag{1.14}$$

and a freely vibrating end satisfying

$$EI\frac{\partial^2 w}{\partial x^2} = 0 \tag{1.15}$$

$$\frac{\partial}{\partial x}\left[EI\frac{\partial^2 w}{\partial x^2}\right] = 0. \tag{1.16}$$

Equation (1.15) defines the *bending moment* and (1.16) the *shear force*, recovering the assumptions about Euler-Bernoulli beam theory made above. Rewriting equation (1.11) gives the equation of motion for an Euler-Bernoulli beam under a load $f(x,t)$

$$\frac{\partial^2}{\partial x^2}\left[EI(x)\frac{\partial^2 w(x,t)}{\partial x^2}\right] + \rho A(x)\frac{\partial^2 w(x,t)}{\partial t^2} = f(x,t). \tag{1.17}$$

Free vibration

The free vibration of an Euler-Bernoulli beam is described by setting $f(x,t) = 0$ in equation (1.17) [20]. Under the additional assumption of a uniform beam, dropping the dependence on x for $I(x)$ and $A(x)$, it simplifies to

$$EI\frac{\partial^4 w(x,t)}{\partial x^4} + \rho A\frac{\partial^2 w(x,t)}{\partial t^2} = 0. \tag{1.18}$$

By defining a constant c it takes the more convenient form of

$$c^2 \frac{\partial^4 w(x,t)}{\partial x^4} + \frac{\partial^2 w(x,t)}{\partial t^2} = 0, \quad \text{with } c = \sqrt{\frac{EI}{\rho A}}. \tag{1.19}$$

Separation of variables with the ansatz $w(x,t) = W(x)T(t)$ yields

$$\frac{c^2}{W(x)} \frac{\mathrm{d}^4 W(x)}{\mathrm{d}x^4} = -\frac{1}{T(t)} \frac{\mathrm{d}^2 T(t)}{\mathrm{d}t^2} \stackrel{!}{=} a = \omega^2 \tag{1.20}$$

where $a = \omega^2$ is a positive constant. Rearranging and defining a new constant β gives the two separate equations

$$\frac{\mathrm{d}^4 W(x)}{\mathrm{d}x^4} - \beta^4 W(x) = 0 \tag{1.21}$$

$$\frac{\mathrm{d}^2 T(t)}{\mathrm{d}t^2} - \omega^2 T(t) = 0, \tag{1.22}$$

$$\text{with} \quad \beta^4 = \frac{\omega^2}{c^2} = \frac{\rho A \omega^2}{EI}. \tag{1.23}$$

The general solution of the time-dependent part is given by

$$T(t) = A \cos \omega t + B \sin \omega t \tag{1.24}$$

where A and B are complex-valued constants that can be determined from the initial conditions. The ansatz for the spatial part takes the form $W(x) = Ce^{sx}$ leading to the general solution

$$W(x) = C_1 \cos \beta x + C_2 \sin \beta x + C_3 \cosh \beta x + C_4 \sinh \beta x \tag{1.25}$$

$$\begin{aligned} &= C_1[\cos \beta x + \cosh \beta x] + C_2[\cos \beta x - \cosh \beta x] \\ &+ C_3[\sin \beta x + \sinh \beta x] + C_4[\sin \beta x - \sinh \beta x] \end{aligned} \tag{1.26}$$

with the constants C_1 to C_4 again to be determined by the specific boundary conditions. Each beam has infinitely many solutions $W_n(x)$ called *normal modes*, oscillating with frequency ω_n. Their orthogonality will be discussed later. The composite solution then reads

$$w_n(x,t) = \sum_{n=1}^{\infty} W_n(x)[A_n \cos \omega_n t + B_n \sin \omega_n t] \tag{1.27}$$

and the *natural frequencies* of each normal mode are given by

$$\omega_n = \beta_n^2 \sqrt{\frac{EI}{\rho A}} = [\beta_n L]^2 \sqrt{\frac{EI}{\rho A L^4}}. \tag{1.28}$$

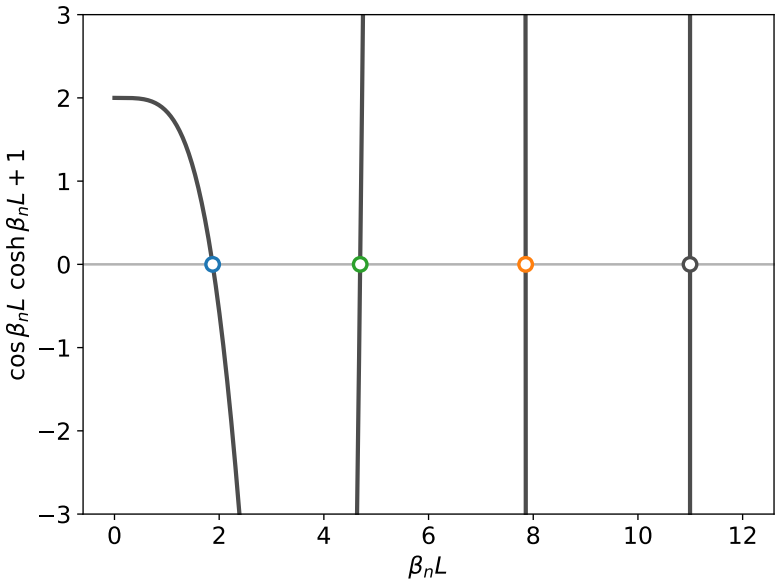

Figure 1.2. – **Euler-Bernoulli frequency equation for a singly clamped beam**

Singly clamped beam

In our case we consider a singly clamped NW with a vibrating free end. Imposing the boundary conditions at the clamped and free end from the above equations (1.14), (1.15) and (1.16) onto the mode shape we have

$$W(0) = 0, \qquad \left.\frac{\mathrm{d}W(x)}{\mathrm{d}x}\right|_{x=0} = 0 \tag{1.29}$$

$$\text{and} \qquad \left.\frac{\mathrm{d}^2W(x)}{\mathrm{d}x^2}\right|_{x=L} = 0, \qquad \left.\frac{\mathrm{d}^3W(x)}{\mathrm{d}x^3}\right|_{x=L} = 0 \tag{1.30}$$

From the first two boundary conditions it follows immediately that $C_1 = C_3 = 0$ in equation (1.26). The third and fourth condition lead to the frequency equation

$$\cos\beta_n L \ \cosh\beta_n L + 1 = 0 \tag{1.31}$$

and the relation

$$C_4 = -\frac{\cos\beta_n L + \cosh\beta_n L}{\sin\beta_n L + \sinh\beta_n L} C_2 \tag{1.32}$$

between the two remaining coefficients. Equation (1.31) defines the natural resonance frequencies of the n-th mode via equation (1.28). It can be solved numerically and the first four solutions are illustrated in Figure 1.2. They are given by

$$\beta_n L = 1.8751,\ 4.6941,\ 7.8547,\ 10.9956,\ \ldots \tag{1.33}$$

$$\frac{\omega_n}{\omega_1} = 1, \qquad 6.2669,\ 17.5473,\ 34.3828,\ \ldots \tag{1.34}$$

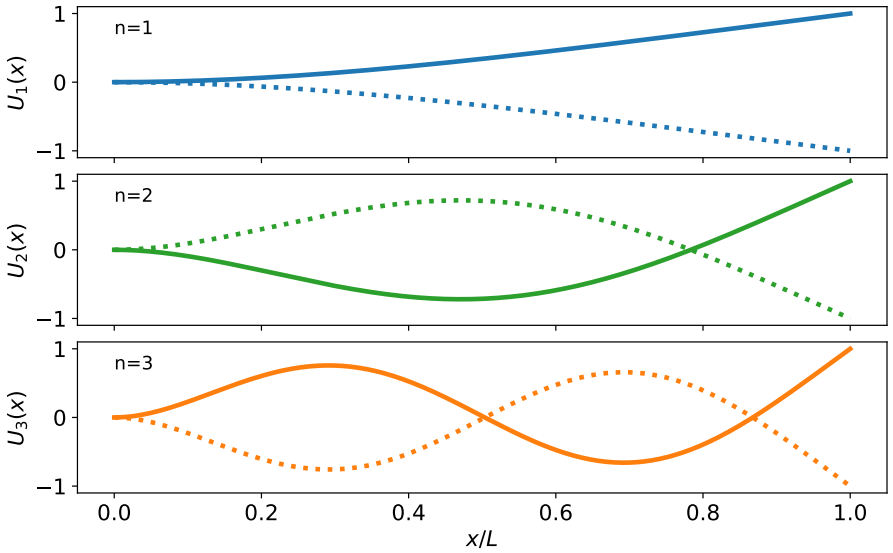

Figure 1.3. – **Normalized mode shapes of a singly clamped beam**

and higher values can be approximated by $\beta_n L \simeq [2n-1]\pi/2$ and $\omega_n/\omega_1 \simeq [(2n-1)\pi/2\beta_1]^2$. The solution for the mode shape can then be given as

$$W_n(x) = C_2\{\cos\beta_n x - \cosh\beta_n x - \frac{[\cos\beta_n L + \cosh\beta_n L]}{\sin\beta_n L + \sinh\beta_n L}[\sin\beta_n x - \sinh\beta_n x]\}. \quad (1.35)$$

Usually the mode shape equation is cast into a more convenient form by normalizing it in the following way [18]

$$W_n(x) = W_{0,n}U_n(x) \quad (1.36)$$

with

$$U_n(x) = \frac{1}{2}\{\cos\beta_n x - \cosh\beta_n x - \frac{[\cos\beta_n L + \cosh\beta_n L]}{\sin\beta_n L + \sinh\beta_n L}[\sin\beta_n x - \sinh\beta_n x]\} \quad (1.37)$$

fulfilling $U_n(L) = 1$. The normalized mode shapes for the first three values of n are plotted in Figure 1.3.

Orthogonality of normal modes

In equation (1.27) we wrote down the composite solution as a sum of its normal modes. These normal modes can be shown to be mutually orthogonal. By inserting the solution of the time dependent part and using the normalized mode shapes $U_n(x)$, the free equation of motion (1.17) can be brought to a harmonic form

$$\frac{\mathrm{d}^2}{\mathrm{d}x^2}\left[EI(x)\frac{\mathrm{d}^2U_n(x)}{\mathrm{d}x^2}\right] - \omega_n^2\rho A(x)U_n(x) = 0. \quad (1.38)$$

Inspecting equation (1.38) we can identify the inertia and stiffness operators as follows [21]

$$\mathcal{M} = \rho A(x) \tag{1.39}$$

$$\mathcal{K} = \frac{\mathrm{d}^2}{\mathrm{d}x^2} EI(x) \frac{\mathrm{d}^2}{\mathrm{d}x^2} \tag{1.40}$$

leading to

$$[\mathcal{K} - \omega_n^2 \mathcal{M}] U_n(x) = 0. \tag{1.41}$$

Additionally we can define a weighted inner product of the normal modes

$$\langle U_m(x) U_n(x) \rangle_{\mathcal{A}} = \int_0^L U_m(x) \mathcal{A} U_n(x) \, \mathrm{d}x \tag{1.42}$$

integrating over the length of the beam with an operator $\mathcal{A}$ acting on the mode shape. By picking two frequencies ω_i and ω_j without loss of generality and using the fact that the eigenvalues are distinct one can derive the following two orthogonality relations [20]

$$\int_0^L \rho A(x) U_i(x) U_j(x) \, \mathrm{d}x = M_i \delta_{ij} \tag{1.43}$$

$$\int_0^L U_j(x) \frac{d^2}{dx^2} \left[EI(x) \frac{d^2 U_i(x)}{dx^2} \right] \mathrm{d}x = M_i \omega_i^2 \delta_{ij} \tag{1.44}$$

where δ_{ij} is the Kronecker delta and $M_i = \langle U_i(x) U_i(x) \rangle_{\mathcal{M}} = \int_0^L \rho A(x) U_i^2(x) dx$ the generalized mass of the i^{th} mode. As a consequence of the expansion theorem any possible displacement $W(x)$ of the beam can be decomposed into the normal modes [22]

$$W(x) = \sum_{n=1}^{\infty} c_n W_n(x) \tag{1.45}$$

with the constant coefficients

$$c_n = \langle W_n(x) W(x) \rangle_{\mathcal{M}} \tag{1.46}$$

$$\omega_n^2 c_n = \langle W_n(x) W(x) \rangle_{\mathcal{K}}. \tag{1.47}$$

1.1.2. Equation of motion

The composite solution (1.27) can be rewritten in terms of the normalized mode shapes, by absorbing the constants into the time dependent part yielding

$$w(x,t) = \sum_{n=0}^{\infty} U_n(x) R_n(t) \tag{1.48}$$

where $R_n(t) = A'_n \cos \omega_n t + B'_n \sin \omega_n t = C'_n e^{i\omega t}$. The exact expressions for A'_n and B'_n or C'_n depend on the initial conditions of the problem at $t = 0$. If we insert the above solution into the general Euler-Bernoulli equation of motion (1.17) one gets

$$\sum_{n=1}^{\infty} \left\{ R_n(t) \frac{\partial^2}{\partial x^2} \left[EI(x) \frac{\partial^2 U_n(x)}{\partial x^2} \right] + \ddot{R}_n(t) \rho A(x) W_n(x) \right\} = f(x,t). \tag{1.49}$$

Multiplying by $U_m(x)$ and integrating along the beam gives

$$\int_0^L \sum_{n=1}^{\infty} \left\{ R_n(t) U_m(x) \frac{\partial^2}{\partial x^2} \left[EI(x) \frac{\partial^2 U_n(x)}{\partial x^2} \right] + \ddot{R}_n(t) \rho A(x) U_m(x) U_n(x) \right\} \mathrm{d}x = \int_0^L U_m(x) f(x,t) \, \mathrm{d}x \tag{1.50}$$

where $\ddot{R}_n(t)$ denotes the second order time derivative. Now we can exchange sum and integral on the left hand side, make use of the orthogonality relations (1.43) and (1.44) to recover the *modal equations of motion*, dropping the summation symbol

$$M_n \ddot{R}_n(t) + \omega_n^2 M_n R_n(t) = F_n(t). \tag{1.51}$$

The *modal mass*, *modal stiffness* (*spring constants*) and *modal force* for the n^{th} mode are given by the following inner products

$$M_n = \langle U_n(x) U_n(x) \rangle_{\mathcal{M}} \tag{1.52}$$

$$k_n = \omega_n^2 M_n = \langle U_n(x) U_n(x) \rangle_{\mathcal{K}} \tag{1.53}$$

$$F_n(t) = \langle U_n(x) f_n(x,t) \rangle. \tag{1.54}$$

The modal equations of motion simplify the problem of a vibrating beam tremendously, decoupling the general equation of motion by virtue of the orthogonality relations. Every mode can be treated as a simple harmonic oscillator with the effective parameters defined above. Writing down the kinetic energies of the beam and a lumped-element model gives [18, 23]

$$\frac{1}{2} \int_0^L \rho A(x) \left[\dot{R}_n(t) U_n(x) \right]^2 dx = \frac{1}{2} M_{\text{eff},n} \dot{R}_n^2(t). \tag{1.55}$$

The left hand side describes how every segment along the beam contributes to the inertial mass of the beam in the kinetic energy and the right hand side assumes an *effective mass* instead. Comparing yields the definition

$$M_{\text{eff},n} = \rho A \int_0^L U_n^2(x) \, \mathrm{d}x \tag{1.56}$$

for a homogeneous beam which is exactly the definition of the modal mass given above. Carrying out the integration and using the normalization condition $|U_n(L)| = 1$ we get [23, 24]

$$M_n = M_{\text{eff},n} = \rho A \frac{L}{4} = \frac{M_{\text{tot}}}{4} \stackrel{!}{=} M_{\text{eff}} \tag{1.57}$$

Since this identity holds for every mode we drop the index and denote the modal mass as M_{eff}. Important to note is that the above result is true for $x = L$ due to the normalization condition. Probing the mass of a NW resonator on a different position $0 \leq x_0 \leq L$ requires to take the mode shape into account and the resulting mass will be overestimated ($\propto 1/U_n^2(x_0)$).

1.1.3. Mechanical dissipation and quality factor

So far we have excluded the role of dissipation in the discussion. Every realistic system is subject to damping. Here we will make use of the Zener model of an anelastic solid to incorporate dissipation into the equation of motion derived in the previous section, following [25, 26]. In a purely elastic solid stress and strain are related by $\sigma = E\epsilon$, essentially stating Hooke's law. Zener generalizes this expression by including rates of change so that

$$\sigma + \tau_\sigma \frac{\mathrm{d}\sigma}{\mathrm{d}t} = E_\mathrm{R}\left[\epsilon + \tau_\epsilon \frac{\mathrm{d}\epsilon}{\mathrm{d}t}\right] \tag{1.58}$$

where E_R is the relaxed Young's modulus and τ_σ and τ_ϵ are phenomenological constants. Assuming harmonic variations in stress and strain given by $\sigma(t) = \sigma_0 e^{i\omega t}$ and $\epsilon(t) = \epsilon_0 e^{i\omega t}$ yields

$$\begin{aligned} E(\omega) = \frac{\sigma_0}{\epsilon_0} &= E_\mathrm{R}\frac{1+i\omega\tau_\epsilon}{1+i\omega\tau_\sigma} \\ &= E_\mathrm{eff}(\omega)\left[1 + \frac{i\omega\bar{\tau}}{1+\omega^2\bar{\tau}^2}\Delta\right] \end{aligned} \tag{1.59}$$

with the definitions $\bar{\tau} = \sqrt{\tau_\epsilon \tau_\sigma}$ and $\Delta = [\tau_\epsilon - \tau_\sigma]/\bar{\tau}$. The real and imaginary parts of the new frequency dependent Young's modulus are given by

$$\Re(E(\omega)) = E_\mathrm{eff}(\omega) = E_\mathrm{R}\frac{1+\omega^2\bar{\tau}^2}{1+\omega^2\tau_\sigma^2} = E' \tag{1.60}$$

$$\Im(E(\omega)) = E_\mathrm{eff}(\omega)\left[\frac{\omega\bar{\tau}}{1+\omega^2\bar{\tau}^2}\Delta\right] = E'' \tag{1.61}$$

For a given harmonic strain the stress has an in-phase and a quadrature component as can be easily seen from equation (1.59). It can be expressed as $\epsilon_0[E' + iE'']e^{i\omega t}$. In the next part we will connect the imaginary part with the quality factor that is defined as $Q = 2\pi W/\Delta W$, where W is the total energy stored in an oscillation cycle and ΔW the occurring losses. The work done by the stress is given by $\mathrm{d}W = \sigma \mathrm{d}\epsilon/\mathrm{d}t$, with the real parts of ϵ and σ. Inserting and integrating over one oscillation cycle yields

$$\Delta W = -\epsilon_0^2\omega \int_0^{2\pi/\omega} \left[E' \cos\omega t \sin\omega t + E'' \sin^2\omega t\right] \mathrm{d}t = \epsilon_0^2 \pi E''. \tag{1.62}$$

In order to get an expression for the maximum energy stored per oscillation we can integrate the in-phase term of the integral over a quarter period [18] noticing that it is oscillating with the frequency 2ω

$$W = -\epsilon_0^2\omega \int_0^{\pi/(2\omega)} E' \cos\omega t \sin\omega t \ \mathrm{d}t = \frac{1}{2}\epsilon_0^2 E'. \tag{1.63}$$

Inserting into the definition of the quality factor results in

$$\frac{1}{Q} = \frac{\Delta W}{2\pi W} = \frac{E''}{E'} = \frac{\omega\bar{\tau}}{1+\omega^2\bar{\tau}^2}\Delta. \tag{1.64}$$

The dissipation is frequency dependent and exhibits a maximum at $\omega\bar{\tau} = 1$ whereas at very high and low frequency values it approaches zero. We can rewrite the Young's modulus as

$$E(\omega) = E_{\text{eff}} \left[1 + \frac{i}{Q}\right]. \tag{1.65}$$

Coming back to the Euler-Bernoulli beam equation (1.18) for the free vibration and inserting the redefined Young's modulus gives, after the separation of variables, a modified relation between the constants β and ω

$$\beta_n^4 = \frac{\omega_n'^2}{c^2} = \frac{\rho A \omega_n'^2}{E_{\text{eff}} I \left[1 + \frac{i}{Q}\right]}. \tag{1.66}$$

Rearranging yields a modified expression for the natural frequencies

$$\begin{aligned} \omega_n' &= \beta_n^2 \sqrt{\frac{I}{\rho A} E_{\text{eff}} \left[+\frac{i}{Q}\right]} \\ &\simeq \beta_n^2 \sqrt{\frac{I}{\rho A} E_{\text{eff}}} \left[1 + \frac{i}{2Q}\right] \\ &= \omega_n \left[1 + \frac{i}{2Q}\right] \end{aligned} \tag{1.67}$$

where we made use of the square root expansion[2] in the limit high quality factor. Inserting the modified natural frequencies into the composite solution (1.48) to the Euler-Bernoulli beam equation gives

$$w(x,t) = \sum_{n=0}^{\infty} U_n(x) R_n(t) e^{-\frac{\omega_n}{2Q} t}. \tag{1.68}$$

with the last exponential factor describing the exponential damping. Following the same procedure as before and plugging the modified solutions into the driven Euler-Bernoulli beam equation 1.17 we can derive modified modal equations of motion of the form

$$M_{\text{eff}} \ddot{R}_n(t) + \Gamma_n \dot{R}_n(t) + \omega_n^2 M_{\text{eff}} R_n(t) = F_n(t) \tag{1.69}$$

where we ignored terms $\propto 1/Q^2$ again in the limit of $Q \gg 1$ and defined the *mechanical dissipation* $\Gamma = \frac{M_{\text{eff}} \omega_n}{Q}$. The quality factor generally depends on frequency and is different for each mode. For singly clamped cantilevers it is shown to increase with the mode number [27–29] whereas in stressed doubly clamped beams it decreases [30]. The exact behavior depends on many contributions and the the quality factor is usually split into different parts $1/Q = \sum_i 1/Q_i$. Possible sources of dissipation in nanomechanical systems are for example thermo-elastic losses, clamping losses, viscous damping, material defects and surface contributions [31, 32]. The latter play an increasing role for

[2] $\sqrt{1+x} = 1 + \frac{1}{2}x - \frac{1}{8}x^2 \ldots$

ultra thin structures due to their surface to volume ratio. Specific surface treatments such as annealing can increase the quality factor substantially [31, 33–35] showing that surface losses are the dominant contribution in this regime. Viscous damping due to the surrounding gas medium can be neglected in our experiments since we work at pressures below 1×10^{-6} mbar [36, 37].

1.2. Force sensing

1.2.1. Response function of the simple harmonic oscillator

In the last section we have derived an equation of motion (1.69) valid for each mode of a singly clamped beam resonator. Noticing its form we can treat the dynamic behavior of the beam as a simple damped harmonic oscillator

$$M\ddot{r}(t) + \Gamma\dot{r}(t) + M\omega_0^2 r(t) = F(t) \tag{1.70}$$

with the difference that $M = M_{\text{eff}}$ and in the limit of high quality factors $Q \gg 1$. Here $\Gamma = \frac{M\omega_0}{Q}$ and we will from now on consider the problem in the form given above, dropping the mode index.

Analyzing the response of a linear time-invariant system, such as the simple harmonic oscillator, to a periodic external driving force $F(t)$ is conveniently performed in Fourier space since $F(t)$ can always be decomposed into its Fourier components. Transforming the harmonic oscillator equation gives

$$-M\omega^2\hat{r}(\omega) - i\Gamma\omega\hat{r}(\omega) + M\omega_0^2\hat{r}(\omega) = \hat{F}(\omega) \tag{1.71}$$

where $\mathscr{F}[r] = \hat{r}(\omega)$ denotes the Fourier transform[3] and we have used some of its properties[4]. Rearranging in the framework of transfer functions yields

$$\chi(\omega) = \frac{\hat{r}(\omega)}{\hat{F}(\omega)} = \frac{1}{M[\omega_0^2 - \omega^2] - i\Gamma\omega}. \tag{1.72}$$

The function $\chi(\omega)$ is the *mechanical susceptibility* and describes the spectral response of the simple damped harmonic oscillator to an external driving force of frequency ω. The time domain signal is given by the inverse Fourier transform acting on $\hat{r}(\omega)$. In order to describe the relation purely in the time domain one would need to consider the convolution $r(t) = (\chi(t) * F(t)) = \int_{-\infty}^{\infty} \chi(\tau)F(t-\tau)\,\mathrm{d}\tau$, which in Fourier space becomes a simple multiplication[5] as exploited above.

It is instructive to split the mechanical susceptibility into its real and imaginary parts

$$\chi'(\omega) = \Re(\chi(\omega)) = \frac{M[\omega_0^2 - \omega^2]}{M^2[\omega_0^2 - \omega^2]^2 + \omega^2\Gamma^2} \tag{1.73}$$

$$\chi''(\omega) = \Im(\chi(\omega)) = \frac{\omega\Gamma}{M^2[\omega_0^2 - \omega^2]^2 + \omega^2\Gamma^2} = |\chi(\omega)|^2\omega\Gamma \tag{1.74}$$

[3] $\mathscr{F}[f] = \hat{f}(\omega) = \int_{-\infty}^{\infty} f(x)e^{i\omega t}\mathrm{d}t$, $\mathscr{F}^{-1}[\hat{f}] = f(t) = \frac{1}{2\pi}\int_{-\infty}^{\infty} f(x)e^{-i\omega t}\mathrm{d}\omega$

[4] $\mathscr{F}[\frac{\mathrm{d}^n f}{\mathrm{d}x^n}] = (-i\omega)^n\hat{f}(\omega)$

[5] $\mathscr{F}[f * g] = \hat{f}(\omega)\hat{g}(\omega)$

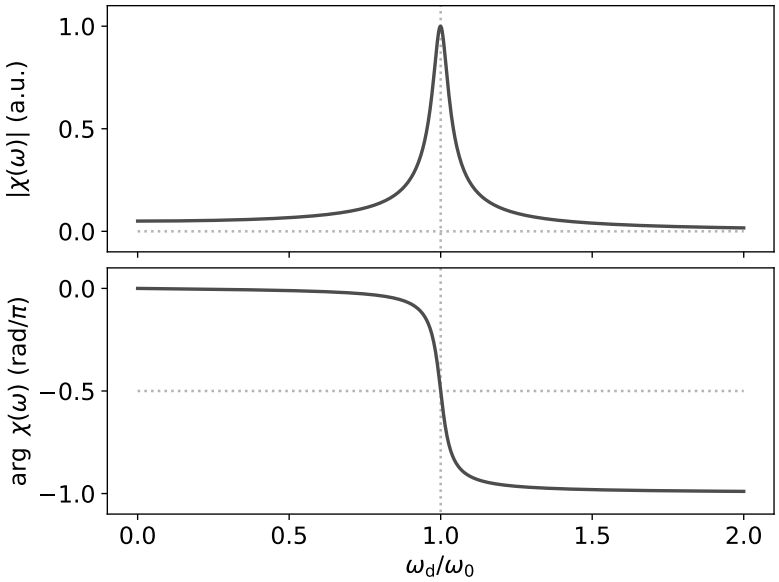

Figure 1.4. – **Mechanical susceptibility of the damped harmonic oscillator** Plotted for $Q = 20$. The amplitude exhibits a peak at $\omega_\mathrm{d} = \omega_0$ and the phase undergoes a π-shift.

and represent the response in polar form with amplitude and phase

$$|\chi(\omega)| = \frac{1}{\sqrt{M^2[\omega_0^2 - \omega^2]^2 + \omega^2\Gamma^2}} \tag{1.75}$$

$$\arg\chi(\omega) = \mathrm{arctan2}\ (\chi'', \chi'). \tag{1.76}$$

The response to an arbitrary drive tone of the form $F_\mathrm{d}(t) = F_0\cos(\omega_\mathrm{d}t + \phi_\mathrm{d})$[6,7] is plotted in Figure 1.4 for a quality factor of $Q = 20$. The amplitude response is peaked at the resonance frequency[8] $\omega_\mathrm{d} \approx \omega_0$, slightly below the natural resonance frequency ω_0. Its approximate value for small damping is $|\chi(\omega_0)| = 1/(\omega_0\Gamma) = Q/k$, where $k = M\omega_0^2$ is the *spring constant*. In DC at $\omega_\mathrm{d} = 0$ the response is given by $|\chi(0)| = 1/k$. This demonstrates that the harmonic oscillator response is amplified by a factor of Q for dynamic forces at resonance as compared to static forces and aiming for a high quality factor greatly improves the dynamic force sensitivity.

The phase response is first in-phase with the driving force at frequencies $\omega_\mathrm{d} \ll \omega_0$. At resonance it exhibits a $\pi/2$ lag with respect to the driving force and at high frequencies $\omega_\mathrm{d} \gg \omega_0$ it is following out of phase (π-shift).

[6] $\hat{F}(\omega) = F_0\pi(\delta(\omega - \omega_\mathrm{d}) + \delta(\omega + \omega_\mathrm{d}))e^{i\phi_\mathrm{d}}$, setting $\phi_\mathrm{d} = 0$ and omitting the negative frequency part.
[7] $\delta(x-a) = \frac{1}{2\pi}\int_{-\infty}^{\infty} e^{i(x-a)t}\mathrm{d}t$, $\int_{-\infty}^{\infty}\delta(x-a)f(x)\mathrm{d}x = f(a)$, $\int_{-\infty}^{\infty}\delta(x)\mathrm{d}x = 1$
[8] $\omega_\mathrm{d} = \omega_0\sqrt{1 - \frac{\Gamma^2}{2Mk}}$

1.2.2. Thermal noise

In order to estimate the ultimate force sensitivity of a NW resonator it is necessary to consider its response to small fluctuations at finite temperature. Consider a resonator coupled to an infinite reservoir of temperature T, driven by the thermal force $F_{\mathrm{th}}(t)$. Its corresponding temporal amplitude fluctuation can be characterized by the difference between their instant value and their time average

$$\tilde{r}(t) = r(t) - \langle r(t) \rangle \tag{1.77}$$

where $\langle r(t) \rangle$ denotes the time average. The time average of the fluctuation itself can be shown to be zero[9]. However we can define their variance

$$\langle \tilde{r}^2(t) \rangle = \langle [r(t) - \langle r(t) \rangle]^2 \rangle = \langle r^2(t) \rangle - \langle r(t) \rangle^2 \tag{1.78}$$

as a useful quantity to capture the nature of the fluctuations. Under the condition that the resonators amplitude is subject to small statistical fluctuations with zero average about its equilibrium position, we can assume that $\langle r(t) \rangle = 0$ and the fluctuations are entirely characterized by their variance. A generalization of the variance is given by the *auto-correlation function*

$$K_r(\tau) = \langle r(t+\tau) r(t) \rangle = \int_{-\infty}^{\infty} r(t) r^*(t-\tau) \, \mathrm{d}t \tag{1.79}$$

where the * denotes the complex conjugate. Note that $K_r(0)$ recovers the variance. The auto-correlation function describes how much a signals amplitude is still correlated after a time interval τ. For thermal fluctuations we assume that they are very short lived i.e. their correlation time τ is way smaller than the response time of the harmonic oscillator[10]. Additionally we assume that the thermal fluctuations are time invariant, that is $K_r(\tau) = K_r(-\tau)$.

Next we are interested in the spectral nature of the fluctuations. The natural approach is to consider the Fourier transform

$$\begin{aligned}
\langle \hat{r}(\omega) \hat{r}^*(\omega') \rangle &= \int_{-\infty}^{\infty} \int_{-\infty}^{\infty} \langle r(t) r(t') \rangle e^{i\omega t - i\omega' t'} \mathrm{d}t' \mathrm{d}t \\
&= \int_{-\infty}^{\infty} \int_{-\infty}^{\infty} K_r(\tau) e^{i(\omega-\omega')t'} e^{i\omega\tau} \mathrm{d}t' \mathrm{d}\tau \\
&= \int_{-\infty}^{\infty} K_r(\tau) e^{i\omega\tau} \mathrm{d}\tau \int_{-\infty}^{\infty} e^{i(\omega-\omega')t'} \mathrm{d}t' \\
&= S_r(\omega) 2\pi\delta(\omega - \omega').
\end{aligned} \tag{1.80}$$

[9] $\langle r(t) - \langle r(t) \rangle \rangle = \langle r(t) \rangle - \langle r(t) \rangle = 0$
[10] $\tau = 2Q/\omega_0 = 2M/\Gamma$

The relation derived above is the *Wiener-Khinchin theorem* and it states that the correlation function and the *spectral density* $S_r(\omega)$ are Fourier transform pairs

$$S_r(\omega) = \int_{-\infty}^{\infty} K_r(\tau) e^{i\omega\tau} \mathrm{d}\tau \tag{1.81}$$

$$K_r(\tau) = \frac{1}{2\pi} \int_{-\infty}^{\infty} S_r(\omega) e^{-i\omega\tau} \mathrm{d}\omega. \tag{1.82}$$

Consider again the special $\tau = 0$ which yields

$$K_r(0) = \langle r^2(t) \rangle = \frac{1}{2\pi} \int_{-\infty}^{\infty} S_r(\omega)\ \mathrm{d}\omega \tag{1.83}$$

relating the variance of the fluctuations to the spectral density. Next we will make use of the equipartition theorem. Under the assumption that the resonator is in thermal equilibrium ($k_B T \gg \hbar\omega_0$) every degree of freedom contributes $\frac{1}{2} k_B T$ to the average energy and we can write for the potential energy [38]

$$\frac{1}{2} M \omega_0^2 \langle r^2(t) \rangle = \frac{1}{2} k_B T. \tag{1.84}$$

With the Wiener-Khinchin theorem (1.83) it follows that

$$\begin{aligned} \langle r^2(t) \rangle &= \frac{1}{2\pi} \int_{-\infty}^{\infty} \langle |\hat{r}(\omega)|^2 \rangle\ \mathrm{d}\omega \\ &= \frac{1}{2\pi} \int_{-\infty}^{\infty} |\chi(\omega)|^2 \langle |\hat{F}_{\mathrm{th}}(\omega)|^2 \rangle\ \mathrm{d}\omega = \frac{k_B T}{M\omega_0^2} \end{aligned} \tag{1.85}$$

where we additionally used the definition of the harmonic oscillator susceptibility (1.72). Noting that the integrand is strongly peaked around ω_0 and using equation (1.74) allows us to write [38]

$$\frac{k_B T}{M\omega_0^2} = \frac{\langle |\hat{F}_{\mathrm{th}}(\omega_0)|^2 \rangle}{2\Gamma} \int_{-\infty}^{\infty} \frac{1}{\pi} \frac{\chi''(\omega)}{\omega}\ \mathrm{d}\omega = \frac{\langle |\hat{F}_{\mathrm{th}}(\omega_0)|^2 \rangle}{2\Gamma M\omega_0^2} \tag{1.86}$$

where in the last step we exploited the *Kramers-Kronig relations*[11] for χ' and χ'' by extending $\chi(\omega)$ to the complex plane. Rearranging gives the following link between the force noise spectrum and the mechanical dissipation

$$S_F(\omega) = \langle |\hat{F}_{\mathrm{th}}(\omega_0)|^2 \rangle = 2\Gamma k_B T \tag{1.87}$$

known as the *fluctuation-dissipation theorem* [39–41]. The expression turns out to be *independent* of frequency, meaning that the spectrum of the thermal noise force driving the resonator is white. Assuming that Γ is universal for a given resonator and does not

[11] $\chi(z) = \int_{-\infty}^{\infty} \frac{1}{\pi} \frac{1}{\omega - z} \chi''(\omega)\ \mathrm{d}\omega$ and $-\frac{1}{\pi}\chi''(\omega)\ \mathrm{d}\omega$ = residue of poles between ω and $\omega + \mathrm{d}\omega$. The integral is also solved in [24].

change with frequency we can extend the relation above to hold for arbitrary ω_0. Using the Wiener-Khinchin theorem once again gives

$$\langle r(t)r(t')\rangle = \frac{1}{2\pi}\int_{-\infty}^{\infty} e^{-i\omega(t-t')}\langle|\hat{F}_{\mathrm{th}}(\omega_0)|^2\rangle = 2\Gamma k_B T\delta(t-t'). \tag{1.88}$$

Now we can derive the noise spectrum of a harmonic oscillator subject to thermal fluctuations [38]

$$\begin{aligned} S_r(\omega) = \langle|r(\omega)|^2\rangle &= |\chi(\omega)|^2\langle|F_{\mathrm{th}}(\omega)|^2\rangle = \langle|F_{\mathrm{th}}(\omega)|^2\rangle\frac{\chi''(\omega)}{\omega\Gamma} = \frac{2k_BT}{\omega}\chi''(\omega) \\ &= 2k_BT\frac{\Gamma}{M^2[\omega_0^2-\omega^2]^2+\omega^2\Gamma^2} \end{aligned} \tag{1.89}$$

In the derivation above we were considering the double-sided spectral density including the negative frequency part. For a real-valued function ($f^* = f$) we can use only the positive frequency half by folding over the negative part and gaining a factor of 2

$$S_r(\omega) = 4k_BT\frac{\Gamma}{M^2[\omega_0^2-\omega^2]^2+\omega^2\Gamma^2}. \tag{1.90}$$

which is called the *displacement noise power spectral density* (PSD). The maximum at $\omega = \omega_0$ gives the resonators maximal thermal amplitude $\langle r^2(\omega_0)\rangle = \frac{4k_BT}{\omega_0^2\Gamma}$ in units of $\mathrm{m^2\,Hz^{-1}}$.

1.2.3. Force sensitivity

The fluctuation-dissipation theorem shows that a mechanical oscillator in thermal equilibrium with its environment will always be subject to fluctuations proportional to its dissipation, independent of frequency. This means that its displacement amplitude fluctuations will settle to a non-zero value imposing a limit on the minimum detectable external force. Using the definition of the mechanical susceptibility again gives

$$\hat{r}(\omega) = \chi(\omega)[\hat{F}_{\mathrm{th}}(\omega) + \hat{F}(\omega)] \tag{1.91}$$

where we consider the thermal noise contribution and an external driving force that we want to measure. Again $F(t)$ may contain only a single frequency so that $\hat{F}(\omega) = F_0\delta(\omega-\omega_{\mathrm{d}})$ (see Section 1.2.1). In an actual measurement we are not able to characterize the full thermal noise frequency spectrum since any measurement is constrained by its bandwidth[12]. Instead we acquire the power spectrum within a certain bandwidth BW, which can be obtained by integrating the power spectral density

$$P_r(\omega) = \int_{\mathrm{BW}}[S_{r,\mathrm{th}}(\omega) + S_{r,\mathrm{d}}(\omega)]\,\mathrm{d}\omega \tag{1.92}$$

[12]It also would require an infinitely long measurement time.

Carrying out the integration and using the dissipation-fluctuation theorem gives

$$P_r(\omega_\mathrm{d}) = |\chi(\omega_\mathrm{d})|^2 4\Gamma k_B T \ \mathrm{BW} + |\chi(\omega_\mathrm{d})|^2 F_0^2 \tag{1.93}$$

and the power spectrum consists of the sum of thermal noise and signal. The ultimate sensitivity is then defined as the point where both contributions are equal, that is the signal-to-noise ratio (SNR) is equal to one. Equating both contributions leads to the following expression for the minimum detectable force

$$F_{0,\mathrm{min}} = \sqrt{4\Gamma k_B T \ \mathrm{BW}} = \sqrt{4 k_B T \frac{M\omega_0}{Q} \ \mathrm{BW}}. \tag{1.94}$$

In literature this quantity is usually normalized to a $\mathrm{BW} = 1\,\mathrm{Hz}$ and has units of $\mathrm{N}/\sqrt{\mathrm{Hz}}$ to be comparable. From the above expression we can easily recognize the prerequisites for an excellent force sensor. It ought to have a small mass, a low resonance frequency and a high quality factor, while being operated at low temperature.

In the derivation of the force sensitivity above we have ignored additional noise contributions in the signal. Apart from the thermal noise there usually is detector noise present in any setup. Possible sources of detection noise are shot noise of the photo diode or additional input noise from instruments or other sources. The detector noise power spectral density $S_{r,\mathrm{det}}(\omega)$ is assumed to be white in most cases.

1.2.4. Formalism for NW resonators

Nanowire resonators can be incorporated into the theory of oscillating beams by considering a symmetric cross-section with equal moments of inertia $I_y = I_z$. In this limit the Euler-Bernoulli beam theory derived in Section 1.1.1 can be modified to include two orthogonal superimposed modes oscillating along z and y, which are degenerate. In practice small asymmetries in the cross-section or the clamping lead to a splitting in frequency [11–13, 34, 42–51] usually by many times their linewidth. We can describe such a system by the superposition of two single Euler-Bernoulli modes with different resonance frequencies $\omega_{n,i}$ and dissipation coefficients $\Gamma_{n,i}$ $(i = 1, 2)$ but with the same effective mass. In the following we formulate expressions for the thermal spectrum and force sensing with with respect to both modes.

Thermal spectrum

The thermal spectrum of the two orthogonal modes is given by the sum their power spectral densities (1.90). Since only the fundamental modes are relevant for our experiments we will from now on only consider the first order modes $r_i(t)$ oscillating along the directions $\mathbf{r}_i$ and label their resonance frequencies and dissipation coefficients as ω_i and Γ_i $(i = 1, 2)$. Then we can write

$$S_r(\omega, r_1, r_2) = S_{r_1}(\omega)\hat{\mathbf{r}}_1 + S_{r_2}(\omega)\hat{\mathbf{r}}_2 \tag{1.95}$$

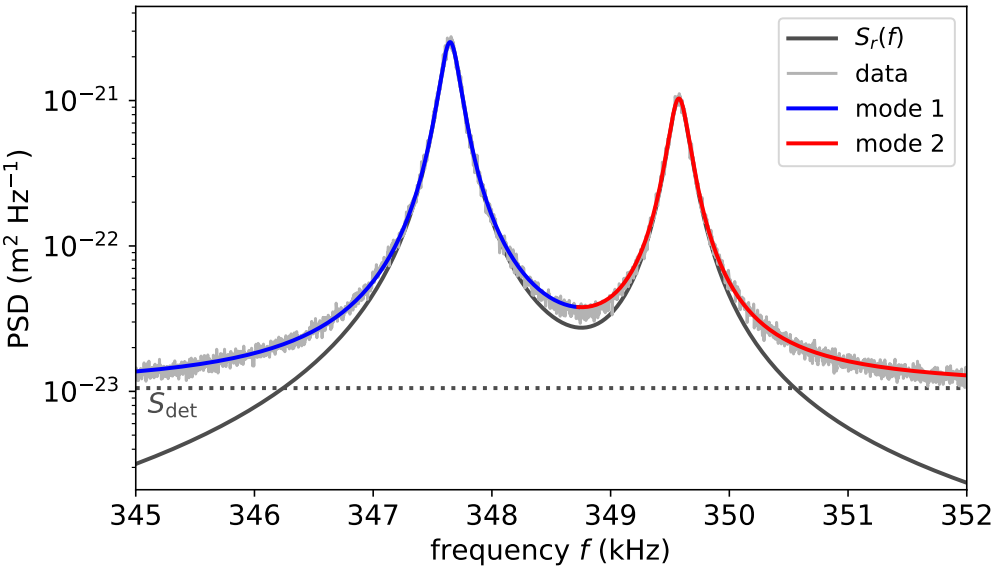

Figure 1.5. – **Thermal noise power spectral density**
Data of a Si NW at room temperature. Fitting with equation (1.96) plus an offset for the detector noise – consisting of electronic noise and the shot noise of the photoreceiver – yields resonance frequencies $f_1 = 347.65\,\mathrm{kHz}$, $f_2 = 349.58\,\mathrm{kHz}$, quality factors $Q_{1,2} \approx 2000$, an effective mass of $M = 8.7 \times 10^{-16}\,\mathrm{kg}$ and $S_{\mathrm{det}} = 1.05 \times 10^{-23}\,\mathrm{m^2\,Hz^{-1}}$. The mode angle α between the measurement vector and the lower frequency mode is $\alpha = 33°$. Indicated are the fitted contributions from both modes in red and blue. The fit according to equation (1.96) without S_{det} is highlighted in dark grey.

In our experiment we detect the NW motion optically with a fiber based interferometer. The quantities we measure is the projection of the NW motion onto the measurement vector (see Section 2.2.3) which is defined as the local optical gradient at the position of the NW pointing in the direction $\hat{\mathbf{e}}_\beta$. Since the NW modes are orthogonal we can write the projection as $\mathbf{r}(t) \cdot \hat{\mathbf{e}}_\beta = \cos(\alpha) r_1(t) \hat{\mathbf{r}}_1 + \sin(\alpha) r_2(t) \hat{\mathbf{r}}_2$. *Remark*: β is defined as the angle between the local optical gradient and the optical axis and α is the angle between the measurement vector and the lower frequency mode (see Figure 2.7 for details).

The power spectral density for the sum of both orthogonal first order modes is then given by

$$\begin{aligned} S_r(\omega) &= S_{r_1}(\omega)\cos^2\alpha + S_{r_2}(\omega)\sin^2\alpha \\ &= 4k_BT\left\{\frac{\Gamma_1\cos^2\alpha}{M^2[\omega_1^2-\omega^2]^2+\omega^2\Gamma_1^2} + \frac{\Gamma_2\sin^2\alpha}{M^2[\omega_2^2-\omega^2]^2+\omega^2\Gamma_2^2}\right\} \\ &= \frac{4k_BT}{M}\left\{\frac{\omega_1\cos^2\alpha}{Q_1[\omega_1^2-\omega^2]^2+\frac{\omega_1^2\omega^2}{Q_1^2}} + \frac{\omega_2\sin^2\alpha}{Q_2[\omega_2^2-\omega^2]^2+\frac{\omega_2^2\omega^2}{Q_2^2}}\right\} \end{aligned} \tag{1.96}$$

where we have used the definition of the mechanical dissipation. This formula is routinely applied to fit the measured spectra for the effective mass or temperature, resonance frequencies, quality factors and the mode angle as illustrated in Figure 1.5. It should be noted that this expression is valid only for a measurement at the tip of the NW ($x_0 = L$). For a different position $0 < x_0 < L$ an additional mode shape factor of $U_0^2(x_0)$ has to be taken into account.

The NW resonator is generally assumed to be in thermal equilibrium and its temperature matches the environment, either room temperature, liquid nitrogen or liquid helium temperature on large time scales. However this assumption is invalid if there are heating effects present due to the readout and/or driving laser for NWs with a high absorption coefficient. At room temperature these are negligible due to the small laser powers and we can estimate the effective mass properly at $x_0 = L$. Once M is fixed we can fit for the mode temperature at cryogenic temperatures, again at the tip of the NW or correcting for the mode shape. To illustrate further it follows from the equipartition theorem (1.84) and the Wiener-Khinchin theorem (1.83) that

$$T_{\mathrm{mode}} = \frac{M\omega_0^2}{k_B}\langle r^2(t)\rangle = \frac{M\omega_0^2}{k_B}\frac{1}{2\pi}\int_0^\infty S_r(\omega)\mathrm{d}\omega \tag{1.97}$$

where $S_r(\omega)$ is the measured power spectral density (1.96) at position x_0 and can be integrated around the resonance in order to retrieve T_{mode}.

Vectorial force sensing

Rossi and de Lepinay simultaneously developed a formalism describing the vectorial force sensing ability of a NW resonator [11, 46, 52]. Following the approach of Rossi we can write down a generalized equation of motion for both NW modes

$$M\ddot{\mathbf{r}}(t) + \begin{bmatrix}\Gamma_1 & 0\\ 0 & \Gamma_2\end{bmatrix}\dot{\mathbf{r}}(t) + \begin{bmatrix}k_1 & 0\\ 0 & k_2\end{bmatrix}\mathbf{r}(t) = \mathbf{F}(\mathbf{r},t) + \mathbf{F}_{\mathrm{th}}(\mathbf{r},t). \tag{1.98}$$

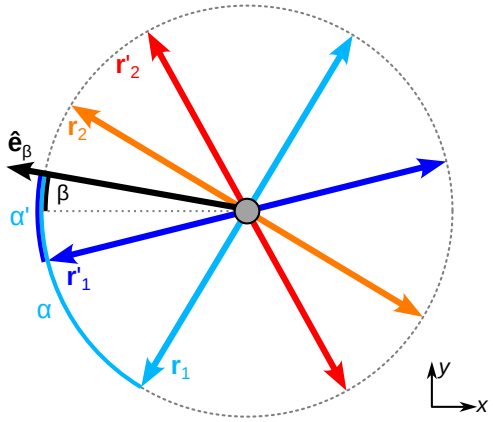

Figure 1.6. – **Eigenmode rotation**
Illustration of the eigenmode rotation when the NW is subject to force gradients. Light blue and orange are the free modes and blue and red the rotated eigenvectors. Black is the measurement vector onto which the motion of the modes is projected. *Remark*: The NW is aligned along the z-axis and oscillating in the xy-plane.

where Γ_i are the dissipation coefficients, k_i the spring constants, $\mathbf{r}(t) = [r_1(t)\ r_2(t)]^T$, $\mathbf{F}(\mathbf{r}, t) = [F_1(r_1, t)\ F_2(r_2, t)]^T$ and $\mathbf{F}_{\text{th}} = [F_{\text{th},1}\ F_{\text{th},2}]^T$. Expanding the external driving force for small oscillations around the origin at $\mathbf{r} = 0$ gives

$$F_i \approx F_i(0) + \sum_{i,j=1,2} r_j \left.\frac{\partial F_i}{\partial r_j}\right|_0 \tag{1.99}$$

Dropping the time dependence and using the shorthand $F_{ij} = \left.\frac{\partial F_i}{\partial r_j}\right|_0$ $i, j \in 1, 2$ yields

$$M\ddot{\mathbf{r}}(t) + \begin{bmatrix} \Gamma_1 & 0 \\ 0 & \Gamma_2 \end{bmatrix} \dot{\mathbf{r}}(t) + \begin{bmatrix} k_1 - F_{11} & -F_{12} \\ -F_{21} & k_2 - F_{22} \end{bmatrix} \mathbf{r}(r) = \mathbf{F}_0 + \mathbf{F}_{\text{th}}. \tag{1.100}$$

The first matrix containing the dissipation coefficients will be labeled $\mathbf{\Gamma}$ and the second containing the effective spring constants $\mathbf{K}$. For small force gradients the natural spring constants become modified by $-F_{ii}$, $i = 1, 2$ and shear forces $-F_{ij}$, $i \neq j$ couple the two modes. $\mathbf{K}$ can be diagonalized under the additional assumption that dissipations are small with respect to the unperturbed resonance frequencies $\frac{\Gamma_i}{2M} \ll \sqrt{\frac{k_i}{M}}$ in order to retrieve new hybridized eigenmodes with eigenvalues of

$$k'_{1,2} = \frac{1}{2}\left[k_1 + k_2 - F_{11} - F_{22} \pm \sqrt{(k_1 - k_2 - F_{11} + F_{22})^2 + F_{12}F_{21}}\right] \tag{1.101}$$

and new normalized eigenvectors expressed in the basis of the unperturbed ones

$$\hat{\mathbf{r}}_1' = \frac{1}{\sqrt{(k_2 - F_{22} - k_1')^2 + F_{12}^2}} \begin{bmatrix} k_2 - F_{22} - k_1' \\ F_{12} \end{bmatrix} \tag{1.102}$$

$$\hat{\mathbf{r}}_2' = \frac{1}{\sqrt{(k_1 - F_{22} - k_2')^2 + F_{21}^2}} \begin{bmatrix} F_{21} \\ k_1 - F_{11} - k_2' \end{bmatrix}. \tag{1.103}$$

This means that shear forces rotate the eigenvector basis of the two modes. By measuring the mode angle α we are able to observe the eigenvector rotation [11]. However due to our detection method (see Section 2.2.3) the sign of α for a single measurement is ambiguous and we have to acquire two consecutive spectra along different measurement vectors in order to clarify the rotation direction. For conservative forces ($\nabla \times \mathbf{F} = 0$) $F_{12} - F_{21} = 0$ and the new eigenvectors retain orthogonality $\hat{\mathbf{r}}_1' \cdot \hat{\mathbf{r}}_2' = 0$.

Now we consider the case of weak forces acting on the NW tip, that is the spring constants of the NW are bigger than the force gradients ($k_i \gg F_{ii}$). We can write for the new eigenvalues and eigenvectors in first order

$$k_1' \approx k_1 - F_{11}, \quad k_2' \approx k_2 - F_{22}, \tag{1.104}$$

$$\hat{\mathbf{r}}_1' = \frac{1}{\sqrt{(k_1 - k_2)^2 + F_{12}^2}} \begin{bmatrix} k_1 - k_2 \\ -F_{12} \end{bmatrix} \tag{1.105}$$

$$\hat{\mathbf{r}}_2' = \frac{1}{\sqrt{(k_1 - k_2)^2 + F_{21}^2}} \begin{bmatrix} F_{21} \\ k_1 - k_2 \end{bmatrix} \tag{1.106}$$

The resonance frequency of the perturbed modes is given by $f_i' = \frac{1}{2\pi}\sqrt{k_i'/M}$. Inserting the above assumption yields

$$f_i' \approx \frac{1}{2\pi}\sqrt{\frac{k_i - F_{ii}}{M}} = \frac{1}{2\pi}\sqrt{\frac{k_i}{M}\left[1 - \frac{F_{ii}}{k_i}\right]} \approx f_i - f_i\frac{F_{ii}}{2k_i} \tag{1.107}$$

Rearranging we can state the frequency shift equation which is at the heart of our measurements

$$\Delta f_i = f_i' - f_i = -\frac{f_i}{2k_i}\left.\frac{\partial F_i}{\partial r_i}\right|_0. \tag{1.108}$$

Scanning force microscopy with a NW resonator enables the simultaneous imaging of the two orthogonal in-plane force gradients by recording its frequency shifts, under the assumption that the acting force gradients are weak compared to the NWs spring constants and that the force field is conservative. If shear forces are present the eigenmode basis rotates by an angle $\delta\alpha$ leaving a mark in the oscillation amplitude signal[13], since the mode projections onto the measurement vector get shifted. Additionally we should note that the oscillation amplitude of the NW is usually kept small enough to locally probe the force gradients, which makes an integration of the force gradient over one oscillation cycle along the NW mode trajectory unnecessary, as required in AFM.

[13] A peak in one mode amplitude and a dip in the other.

1.3. Magnetic contrast formation

Since the advent of magnetic force microscopy (MFM) [3, 53] many different probe designs have been fabricated, in the beginning with the aim to just pick up magnetic signals from surfaces and later to improve spatial resolution and understand better the meaning of the measured quantities. Early designs were using electrochemically etched magnetic wires [3, 54–59] and relying on modifying cantilevers by depositing magnetic material somewhere close to the tip [60]. As a standard technique emerged the coating of Si AFM cantilever tips with magnetic thin films [61] which offers the advantage of a reliable and large scale fabrication process. More recent efforts focus on enhancing specific properties of the magnetic imaging probes. For example a double coating separated by a spacer layer can be used to realize a dipole tip model which possesses enhanced sensitivity to small spatial frequencies [62, 63]. Other approaches focus on thin and sharp magnetic tips at the apex of AFM cantilevers by electron beam induced deposition [64–68], coating of carbon nanotubes [69–71] iron filled carbon nanotubes [72–75] or attaching an iron NW to a cantilever [76]. An excellent overview of recent progress is given in [63] and [77].

The formation of the magnetic imaging contrast is very complex since the mutual interaction between tip and sample field can become quite convoluted. Generally one aims for a hard magnetic tip possessing a magnetization state that is unperturbed by the sample stray field [63]. In this regime we can assume that the tip magnetization is fixed throughout the whole measurement and a static tip model describes the interaction of the tip with the sample stray field. The sample magnetization on the other hand might be very well disturbed by the the tip stray field [78], also leading to interesting dissipation effects. Designing a suitable MFM probe requires balancing a lot of factors e.g. spatial resolution, magnetic sensitivity, invasiveness, expected sample stray field, external field range, temperature range, tip model and many more.

1.3.1. Stray field and magnetization reconstruction

Let us first consider the stray field of a sample with a given time-independent magnetization. The Maxwell's equations for magnetic fields in the static case with no free currents present are given in differential form by

$$\nabla \cdot \mathbf{B} = 0 \tag{1.109}$$

$$\nabla \times \mathbf{H} = 0 \tag{1.110}$$

where the magnetic field strength $\mathbf{H}$ and the magnetic flux density $\mathbf{B}$ are related by $\mathbf{B} = \mu_0(\mathbf{H} + \mathbf{M})$. The magnetization $\mathbf{M}$ is defined in the sample volume $V \subseteq \mathbb{R}^3$ and zero outside. It follows from (1.109) that [63, 79]

$$\nabla \cdot \mathbf{H} = -\nabla \cdot \mathbf{M}. \tag{1.111}$$

Since $\mathbf{H}$ is conservative (1.110) we can express it in terms of the magnetic scalar potential[14]

$$\mathbf{H} = -\nabla\phi_m \tag{1.112}$$

and it fulfills the Poisson equation

$$\nabla^2\phi_m(\mathbf{r}) = -\rho_m, \quad \mathbf{r} \in V \tag{1.113}$$

$$\nabla^2\phi_m(\mathbf{r}) = 0 \quad \text{otherwise.} \tag{1.114}$$

Additionally it needs to satisfy the boundary conditions that it is continuous across the surface. The magnetic volume and surface charges are defined as follows

$$\rho_m = -\nabla \cdot \mathbf{M} \tag{1.115}$$

$$\sigma_m = \hat{\mathbf{n}} \cdot \mathbf{M} \tag{1.116}$$

where $\hat{\mathbf{n}}$ is the unit vector normal to the boundary surface S of V. Then the scalar potential can be expressed as[15]

$$\phi_m(\mathbf{r}) = \frac{1}{4\pi}\left[\int_V \frac{\rho_m}{|\mathbf{r}-\mathbf{r}'|}\mathrm{d}^3r' + \int_S \frac{\sigma_m}{|\mathbf{r}-\mathbf{r}'|}\mathrm{d}^2r'\right] \tag{1.117}$$

and by applying equation (1.112) we receive an expression for the stray field

$$\mathbf{H}(\mathbf{r}) = \frac{1}{4\pi}\left\{-\int_V \frac{[\nabla'\cdot\mathbf{M}][\mathbf{r}-\mathbf{r}']}{|\mathbf{r}-\mathbf{r}'|^3}\mathrm{d}^3r' + \int_S \frac{[\hat{\mathbf{n}}\cdot\mathbf{M}][\mathbf{r}-\mathbf{r}']}{|\mathbf{r}-\mathbf{r}'|^3}\mathrm{d}^2r'\right\}. \tag{1.118}$$

It immediately follows that the stray field can be calculated from integrating over magnetic volume and surface charges across the volume of the sample. For a uniform magnetization ($\rho_m = 0$) and we only need to consider the second integral for the surface charge contributions.

In MFM we are usually interested in solving the inverse problem and obtaining the magnetization from the measured stray field or frequency shift. Unfortunately for a given stray field the magnetization is not unique, since many different volume densities and surfaces charges may lead to the same stray field, even for a uniform magnetization unless additional assumptions are made [63].

To treat the inverse problem it is useful to transform the equations to Fourier space. Since our images are taken in the xy-plane above the sample of interest we map $\mathbf{r} = [x, y, z] \to [k_x, k_y, z]$ where the sample is located at $z = 0$. The nabla operator takes the form $\nabla_k = [ik_x, ik_y, \frac{\partial}{\partial z}]$ and we can transform the free space equation (1.114) to [63]

$$\nabla_k^2\hat{\phi}_m(\mathbf{k}, z) = -[k_x^2 + k_y^2]\hat{\phi}_m(\mathbf{k}, z) + \frac{\partial^2\hat{\phi}_m(\mathbf{k}, z)}{\partial z^2} = 0 \tag{1.119}$$

$$\Leftrightarrow \quad \hat{\phi}_m(\mathbf{k}, z) = \frac{1}{k^2}\frac{\partial^2\hat{\phi}_m(\mathbf{k}, z)}{\partial z^2} \tag{1.120}$$

[14] $\nabla \times \nabla\phi(\mathbf{r}) = 0$ holds for any scalar $\phi(\mathbf{r})$.

[15] Using the identities $\nabla'\left[\frac{1}{|\mathbf{r}-\mathbf{r}'|}\right] = \frac{\mathbf{r}-\mathbf{r}'}{|\mathbf{r}-\mathbf{r}'|^3}$, $\delta^3(\mathbf{r}-\mathbf{r}') = -\frac{1}{4\pi}\nabla^2\frac{1}{|\mathbf{r}-\mathbf{r}'|}$ and the divergence theorem.

with the spatial wave vector $\mathbf{k} = (k_x, k_y)$ and $k = \sqrt{k_x^2 + k_y^2}$. The general solution can be spotted immediately to be

$$\hat{\phi}_m(\mathbf{k}, z) = \hat{\phi}_m(\mathbf{k}, 0)e^{-kz}. \tag{1.121}$$

Applying equation (1.112) gives the stray field in Fourier space as[16]

$$\mathbf{h}(\mathbf{k}, z) = -\nabla_k[\hat{\phi}_m(\mathbf{k}, 0)e^{-kz}] = \mathbf{h}(\mathbf{k}, 0)e^{-kz} \tag{1.122}$$

and reveals the fact that knowing the field for one distance z_0 allows for upward or downward continuation by multiplying with a factor $e^{-k\Delta z}$. The components of the stray field are then

$$\mathbf{h}(\mathbf{k}, z) = -\begin{bmatrix} ik_x \\ ik_y \\ \frac{\partial}{\partial z} \end{bmatrix} \hat{\phi}_m(\mathbf{k}, z) = \begin{bmatrix} -ik_x \\ -ik_y \\ k \end{bmatrix} \hat{\phi}_m(\mathbf{k}, z) \tag{1.123}$$

and the nabla operators z-component can be identified as $-k$. It follows that the stray field components are not independent but once for example the z-component is known the x- and y-component can be calculated as

$$h_z(\mathbf{k}, z) = k\hat{\phi}_m(\mathbf{k}, z) \tag{1.124}$$

$$h_{x,y}(\mathbf{k}, z) = -\frac{ik_{x,y}}{k} h_z(\mathbf{k}, z). \tag{1.125}$$

Another way to see this is by starting from Maxwell's equations (1.110) and (1.109) which give in Fourier space

$$ik_y h_z = -kh_y \tag{1.126}$$

$$ik_x h_z = -kh_x \tag{1.127}$$

$$ik_x h_y = ik_y h_x \tag{1.128}$$

$$\text{and} \quad kh_z = ik_x h_x + ik_y h_y. \tag{1.129}$$

The set of equations is over defined and knowing one component fixes the other two [80]. Note that singularities arise in the case where k_x, k_y or k are equal to zero. This case corresponds to a uniform DC offset of the stray field in real space. Since the equations above all contain first order derivatives this offset remains undefined. Lima [80] developed ways to treat the singularities, which is beyond the scope of this work.

The link between field and magnetization in Fourier space can be written in matrix form. By assuming that the magnetization is restricted to a 2D plane at $z = 0$, that is $\mathbf{M}(\mathbf{r}) = \mathbf{M}(x, y, 0)$, one can derive the following relation [81–84]

$$\mathbf{h}(\mathbf{k}, z) = -\frac{1}{2}e^{-kz} \begin{bmatrix} k_x^2/k & k_x k_y/k & ik_x \\ k_x k_y/k & k_y^2/k & ik_y \\ ik_x & ik_y & -k \end{bmatrix} \mathbf{m}(\mathbf{k}, 0) \tag{1.130}$$

[16] The Fourier transforms of $\mathbf{H}(\mathbf{r})$ and $\mathbf{M}(\mathbf{r})$ are denoted with small letters $\mathbf{h}(\mathbf{k})$ and $\mathbf{m}(\mathbf{k})$.

Since the matrix possesses rank 1 it is apparent that the system of equations is not linearly independent and allows for infinitely many solutions. However fixing the direction of $\mathbf{M}$ (e.g. out-of-plane) gives a set of equations that can be solved for the component(s) of the magnetization [7, 8, 84–86]. Of course it is also possible to guess a magnetization and calculate the stray field using the above equation until it agrees with the observational data.

1.3.2. Tip models and transfer function approach

Now that we have established a link between magnetization and stray field, we will take it one step further and explore how the stray field and the corresponding forces acting on the NW resonator are related. Aiming for quantitative MFM requires the precise knowledge of the tip magnetization or a suitable calibration procedure. Early models focused on cone-shaped or pyramidal tips [4–6, 87–89] as they were used on most MFM experiments. Hug and van Schendel later developed the powerful transfer function model [7, 8] applicable to the calibration of any magnetic tip.

Tip transfer function

Following Hug and van Schendel [7, 8] we can derive the force acting on a tip with magnetization $\mathbf{M}_{\text{tip}}$ as response to the sample stray field $\mathbf{H}$. The magnetostatic energy is given by [79, 90]

$$E_m(\mathbf{r}, z) = -\mu_0 \int \mathbf{M}_{\text{tip}}(\mathbf{r}', z') \cdot \mathbf{H}(\mathbf{r} + \mathbf{r}', z + z') \mathrm{d}\mathbf{r}' \mathrm{d}z' \tag{1.131}$$

where the coordinate systems are illustrated in Figure 1.7 and $\mathbf{H}(\mathbf{r}, z)$ is the sample stray field. The force acting on the tip is then given by the gradient of the magnetostatic energy

$$\begin{aligned} \mathbf{F}(\mathbf{r}, z) &= \mu_0 \int \nabla \left[\mathbf{M}_{\text{tip}}(\mathbf{r}', z') \cdot \mathbf{H}(\mathbf{r} + \mathbf{r}', z + z') \right] \mathrm{d}\mathbf{r}' \mathrm{d}z' \\ &= \mu_0 \int \left[\mathbf{M}_{\text{tip}}(\mathbf{r}', z') \cdot \nabla \right] \mathbf{H}(\mathbf{r} + \mathbf{r}', z + z') \mathrm{d}\mathbf{r}' \mathrm{d}z' \end{aligned} \tag{1.132}$$

where we exploited that $\mathbf{H}(\mathbf{r}, z)$ is conservative and a known vector calculus identity[17]. Applying the two dimensional Fourier transform as in the previous section with respect to the sample coordinate system yields

$$\hat{\mathbf{F}}(\mathbf{k}, z) = \mu_0 \int \left[\mathbf{M}_{\text{tip}}(\mathbf{r}', z') \cdot \nabla_k \right] \left[\int \mathbf{H}(\mathbf{r} + \mathbf{r}', z + z') e^{-i\mathbf{k}\mathbf{r}} \mathrm{d}\mathbf{r} \right] \mathrm{d}\mathbf{r}' \mathrm{d}z'. \tag{1.133}$$

In the next step we use the coordinate transformation $\tilde{\mathbf{r}} = \mathbf{r} + \mathbf{r}'$ and the upward propagation of the stray field from the previous section[18] to receive

$$\hat{\mathbf{F}}(\mathbf{k}, z) = \mu_0 \mathbf{h}(\mathbf{k}, z) \int \hat{\mathbf{M}}^*_{\text{tip}}(\mathbf{k}, z') e^{-kz'} \nabla_k \mathrm{d}z'$$

[17] $\nabla \left[\mathbf{A} \cdot \mathbf{B} \right] = \left[\mathbf{A} \cdot \nabla \right] \mathbf{B} + \left[\mathbf{B} \cdot \nabla \right] \mathbf{A} + \mathbf{A} \left[\nabla \times \mathbf{B} \right] + \mathbf{B} \left[\nabla \times \mathbf{A} \right]$

[18] $\mathbf{h}(\mathbf{k}, z + z') = \mathbf{h}(\mathbf{k}, z) e^{-kz'}$

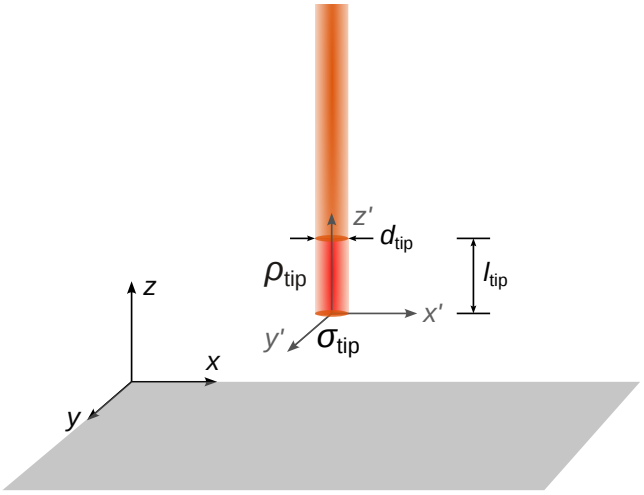

Figure 1.7. – **Magnetic NW tip**
Illustration of a cylindrical magnetic NW tip hovering above the sample plane. The orange part represents the non-magnetic part of the NW and the red part the tip possessing a magnetic volume charge ρ_{tip} and magnetic surface charges σ_{tip}. The tip dimensions are given by the diameter d_{tip} and the tip length l_{tip} and the primed coordinate system represents the tip reference system with its origin at the apex of the tip.

$$\begin{aligned} &= \mu_0 \mathbf{h}(\mathbf{k}, z) \int \rho^*_{\text{tip}}(\mathrm{k}, z) e^{-kz'} \mathrm{d}z' \\ &= \mu_0 \sigma^*_{\text{tip}}(\mathbf{k}) \mathbf{h}(\mathbf{k}, z) \end{aligned} \tag{1.134}$$

where we again used the form of ∇_k in fourier space[19] and defined the complex conjugates of the equivalent magnetic surface charge density and the magnetic volume charge density

$$\rho^*(\mathbf{k}, z') = \nabla^*_k \hat{\mathbf{M}}^*_{\text{tip}}(\mathbf{k}, z') \tag{1.135}$$

$$\sigma^*_{\text{tip}}(\mathbf{k}) = \int \rho^*_{\text{tip}}(\mathbf{k}, z') e^{-kz'} \mathrm{d}z'. \tag{1.136}$$

This result shows that in Fourier space the force acting on the magnetic NW tip becomes a simple multiplication of the equivalent magnetic surface charge density with the stray field.

It remains to determine the relation between the frequency shift of the NW modes, which is proportional to the force gradient along the mode direction as derived in equation (1.108), and the stray field. We can write for the force along the modes ($i = 1, 2$)

$$\begin{aligned} \hat{F}_i(\mathbf{k}, z) &= \hat{\mathbf{r}}_i \cdot \hat{\mathbf{F}}(\mathbf{k}, z) \\ &= \mu_0 \sigma^*_{\text{tip}}(\mathbf{k}) \; \hat{\mathbf{r}}_i \cdot \mathbf{h}(\mathbf{k}, z). \end{aligned} \tag{1.137}$$

[19] $\nabla_k = [ik_x, ik_y, -k]$

In the MFM literature one usually continues by expressing the field as derivative of its z-component (see previous section) and defining from that a lever canting function LCF($\mathbf{k}$)[20], which takes into account a tilt of the oscillation direction with respect to the z-axis. We however continue with the expression above. The derivative along the NW modes is given by

$$\begin{aligned}\frac{\partial \hat{F}_i}{\partial r_i} &= \hat{\mathbf{r}}_i \cdot \nabla_k \hat{F}_i(\mathbf{k}, z) \\ &= \mu_0 \sigma^*_{\text{tip}}(\mathbf{k})\ \hat{\mathbf{r}}_i \cdot \nabla_k [\hat{\mathbf{r}}_i \cdot \mathbf{h}(\mathbf{k}, z)].\end{aligned} \tag{1.138}$$

Now we will assume a specific form of $\hat{\mathbf{r}}_i$ namely that it represents the oscillation direction of the first mode given by $\hat{\mathbf{r}}_1 = [\cos\alpha, \sin\alpha, 0]$, where α is the mode angle[21]. Inserting yields

$$\begin{aligned}\frac{\partial \hat{F}_1}{\partial r_1} &= \mu_0 \sigma^*_{\text{tip}}(\mathbf{k}) \hat{\mathbf{r}}_1 \nabla_k \left[h_x(\mathbf{k}, z)\cos\alpha + h_y(\mathbf{k}, z)\sin\alpha\right] \\ &= \mu_0 \sigma^*_{\text{tip}}(\mathbf{k}) [ik_x \cos\alpha + ik_y \sin\alpha] \left[h_x(\mathbf{k}, z)\cos\alpha + h_y(\mathbf{k}, z)\sin\alpha\right] \\ &\overset{(1.128)}{=} \mu_0 \sigma^*_{\text{tip}}(\mathbf{k}) \frac{i}{k_x} h_x(\mathbf{k}, z) [k_x \cos\alpha + k_y \sin\alpha]^2 \\ &= \mu_0 \sigma^*_{\text{tip}}(\mathbf{k}) \text{NWTF}^2(\mathbf{k}, \alpha) \frac{i}{k_x} h_x(\mathbf{k}, z)\end{aligned} \tag{1.139}$$

where we defined the NW transfer function as

$$\text{NWTF}(\mathbf{k}, \alpha) = [k_x \cos\alpha + k_y \sin\alpha] \tag{1.140}$$

Note that it corresponds to the lever canting function LCF($\mathbf{k}$) for $\hat{\mathbf{n}}$ oriented in-plane and that an equivalent expression for the force gradient exists in terms of the y-component of the stray field[22]. Finally we can give the relation between the frequency shifts of both modes and the stray field in Fourier space

$$\Delta f_1(\mathbf{k}, z) = -\frac{f_1}{2k_1} \mu_0 \sigma^*_{\text{tip}}(\mathbf{k}) \text{NWTF}^2(\mathbf{k}, \alpha) \frac{i}{k_{x,y}} h_{x,y}(\mathbf{k}, z) \tag{1.141}$$

$$\Delta f_2(\mathbf{k}, z) = -\frac{f_2}{2k_2} \mu_0 \sigma^*_{\text{tip}}(\mathbf{k}) \text{NWTF}^2(\mathbf{k}, \alpha + \frac{\pi}{2}) \frac{i}{k_{x,y}} h_{x,y}(\mathbf{k}, z). \tag{1.142}$$

The frequency shift of the second mode is simply given by the orthogonality of the NW modes. Inverting the above equations one can calculate the stray field from frequency shift, provided $\sigma^*_{\text{tip}}(\mathbf{k})$ is known. In a second step a magnetization pattern can be obtained from the stray field as demonstrated in Section 1.3.1, under the assumption that the direction of the sample magnetization is fixed and constrained to a two-dimensional plane.

[20] $\mathbf{h}(\mathbf{k}, z) = -\frac{1}{k}\nabla h_z(\mathrm{k}, z)$, LCF($\mathbf{k}$) $= -\frac{1}{k}\hat{\mathbf{n}}\nabla_k$, where n̂ is normal to the cantilever surface.
[21] Additionally we assume that the measurement vector is along the optical axis ($\beta = 0°$).
[22] $\frac{\partial \hat{F}_1}{\partial r_1} = \mu_0 \sigma^*_{\text{tip}} \text{NWTF}^2(\mathbf{k}, \alpha) \frac{i}{k_y} h_y(\mathbf{k}, z)$

In this framework solely the equivalent magnetic surface charge $\sigma^*_{\text{tip}}(\mathbf{k})$ describes the magnetic part of the interaction with the stray field. Characterizing it is key to quantitative magnetic force microscopy imaging. There is three ways that have been followed to obtain the form of $\sigma^*_{\text{tip}}(\mathbf{k})$.

Instrument calibration The beauty of the transfer function approach of Hug and van Schendel [7, 8] is that $\sigma^*_{\text{tip}}(\mathbf{k})$ can be calibrated without any assumptions about the magnetic tip. They use magnetic thin films with a well known stray field pattern originating from purely out-of-plane magnetization. By measuring the frequency shift both sides of the transfer function equation are fully known and one can fit for $\sigma^*_{\text{tip}}(\mathbf{k})$. The resulting instrument calibration function, also containing the LCF, is completely defined and can later be used for a different measurement. It is of vital importance to use a calibration sample containing a wide range of spatial frequencies.

Micromagnetic simulations The second option is to numerically obtain an expression for $\sigma^*_{\text{tip}}(\mathbf{k})$ from micromagnetic simulations. This requires a precise knowledge of the magnetic volume and surface density in real space, which is a very difficult task in itself. The equivalent magnetic surface charge density would then be given by [7]

$$\sigma_{\text{tip}}(\mathbf{k}, z) = \int \rho_{\text{tip}}(\mathbf{r}', z') e^{-kz'} e^{-i\mathbf{kr}} \mathrm{d}\mathbf{r}' \mathrm{d}z' + \oint \sigma_{\text{tip}}(\mathbf{r}', z') e^{-kz'} e^{-i\mathbf{kr}'} \mathrm{d}\mathbf{r}' \quad (1.143)$$

The idea of this approach is to access the stray field from the measured frequency shift by modeling $\sigma^*_{\text{tip}}(\mathbf{k})$.

Geometric models The third option is a simple geometrical model for the tip magnetization and use equation (1.143) as well. In MFM this method has been applied [4, 6, 91], however it is generally overestimating the signal response and a comparison with the first method highlights that there is no agreement with the obtained calibration and the simple models (see Figure 9 in [8]). Nonetheless we will consider some point-pole models in the next section, since they are interesting to apply for NW resonators.

Point-pole model

The magnetization of the tip can be approximated by simple point-like magnetic monopoles and dipoles located at some distance Δz with respect to the tip apex [87, 92, 93]. An illustration is displayed in Figure 1.8 [7]. If the tip magnetization is confined to a very small volume of the apex it is usually best approximated by a point dipole. However if it consists of an elongated cylindrical volume and the shape anisotropy dominates, only one pole interacts with the sample stray field and a monopole is suitable to describe the magnetic interaction. The force from the point poles immersed the sample stray field acting at the tip is given by

$$\mathbf{F}(\mathbf{r}_t, z_t) = \mu_0 \left[q_{\text{tip}} \mathbf{H}(\mathbf{r}_t, z_t + \Delta z_{\text{mono}}) + \mathbf{m}_{\text{tip}} \nabla \cdot \mathbf{H}(\mathbf{r}_t, z_t + \Delta z_{\text{dip}}) \right] \quad (1.144)$$

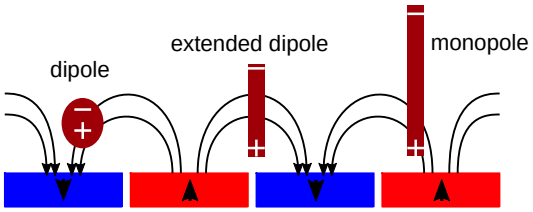

Figure 1.8. – **Magnetic tip models**
Illustration of point-pole MFM tip models. Adapted from [7].

where q_{tip} and $\mathbf{m}_{\text{tip}}$ are the magnetic monopole and dipole moment of the tip and the tip apex is located at $(\mathbf{r}_t, z_t)$. Fourier transforming yields directly the tip equivalent magnetic surface charge as [8]

$$\sigma_{\text{tip}}(\mathbf{k}) = q_{\text{tip}} + \mathbf{m}_{\text{tip}} \nabla_k^* \tag{1.145}$$

and we see that in a perfect monopole model the response is constant in Fourier space and in the perfect dipole case it is linear in k. A dipole tip thus offers an amplified response to higher spatial frequencies.

It is instructive to also derive $\sigma_{\text{tip}}(\mathbf{k})$ from a given magnetization in real space by solving equation (1.143) [7, 76]. Assuming a uniform magnetization pointing along the NW axis of a NW tip with diameter d_{tip} and and length l_{tip} (see Figure 1.7) we immediately have that $\rho_{\text{tip}}(\mathbf{k}, z) = 0$ and $\sigma_{\text{tip}}(\mathbf{r}, z) = M_s$ at the two ends with opposite surface normals with the saturation magnetization M_s of the tip material. Inserting gives

$$\begin{aligned}
\sigma_{\text{tip}}^{\text{mono}}(\mathbf{k}, z) &= M_s \left[1 - e^{-kl_{\text{tip}}}\right] \oint_A e^{-i\mathbf{k}\mathbf{r}'} \mathrm{d}\mathbf{r}' \\
&= M_s \left[1 - e^{-kl_{\text{tip}}}\right] \int_0^{\frac{d_{\text{tip}}}{2}} \int_0^{2\pi} r' e^{-ikr'\cos(\theta)} \mathrm{d}\theta \mathrm{d}r \\
&\overset{y=kr'}{=} M_s \left[1 - e^{-kl_{\text{tip}}}\right] \frac{2\pi}{k^2} \int_0^{\frac{kd_{\text{tip}}}{2}} y J_0(y) \mathrm{d}y \\
&= M_s \left[1 - e^{-kl_{\text{tip}}}\right] \frac{2\pi}{k^2} \left[y J_1(y)\right]_0^{\frac{kd_{\text{tip}}}{2}} \\
&= M_s \frac{\pi d_{\text{tip}}}{k} J_1\left(k\frac{d_{\text{tip}}}{2}\right) \left[1 - e^{-kl_{\text{tip}}}\right].
\end{aligned} \tag{1.146}$$

where we have used a few properties of the Bessel functions J_n of the first kind[23]. The last factor can be understood as the contributions from the two magnetic surface charges placed at either end of the cylindrical tip. The longer the tip the less impact the further end has on the transfer function and the model comes close to a perfect monopole. In

[23] $J_n(y) = \frac{1}{2\pi i^n} \int_0^{2\pi} e^{iy\cos\theta} e^{in\theta} \mathrm{d}\theta$, $J_n(y) = J_n(-y)$ for even n, and $\frac{\mathrm{d}}{\mathrm{d}y}\left[y^n J_n(y)\right] = y^n J_{n-1}(y)$

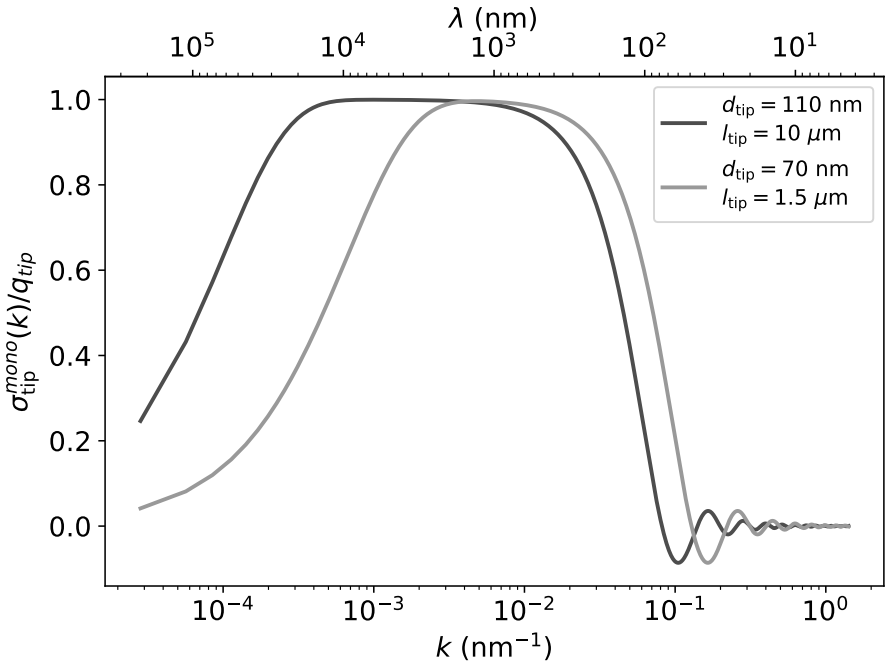

Figure 1.9. – **Monopole force transfer functions**
Plotted is the monopole force transfer function $\sigma_{\mathrm{tip}}^{\mathrm{mono}}(k)$ normalized to the monopole surface charge q_{tip} for two different cases. In dark gray for a NW that is fully magnetic over a length of $l_{\mathrm{tip}} = L = 10\,\mu\mathrm{m}$ and a diameter of $d_{\mathrm{tip}} = 110\,\mathrm{nm}$. In light grey we show $\sigma_{\mathrm{tip}}^{\mathrm{tip}}(k)$ for a tip diameter of $d_{\mathrm{tip}} = 70\,\mathrm{nm}$ and a length of $l_{\mathrm{tip}} = 1.5\,\mu\mathrm{m}$. The response to higher spatial frequencies mainly depends on the diameter of the NW and falls of sharply when the spatial features become smaller that d_{tip}. On the other end small spatial frequencies are better imaged with a long magnetic tip. Approximating $\sigma_{\mathrm{tip}}^{\mathrm{mono}}(k)$ with q_{tip} is only valid in the corridor of spatial frequencies where it approaches a value of one as pointed out by Freitag et al. [76].

the case of a very long ($l_{\text{tip}} \to \infty$) and thin ($k \ll d_{\text{tip}}$) magnetic tip, expanding the Bessel function for a small argument gives[24]

$$\sigma_{\text{tip}}^{\text{mono}}(\mathbf{k}) \approx M_s \frac{\pi d_{\text{tip}}^2}{4} = q_{\text{tip}}. \tag{1.147}$$

For the ideal monopole tip the tip equivalent magnetic surface charge is given by the saturation magnetization multiplied with the tip cross-section.

Figure 1.9 shows $\sigma_{\text{tip}}^{\text{mono}}(k)$ for two different dimensions of the magnetic tip. First for a fully magnetic NW so that the NW *is* the tip and second for a NW with a shorter and slightly thinner tip attached to its end. It is evident that the response to higher spatial frequencies is sharply limited by the tip diameter d_{tip}, whereas lower spatial frequencies are better captured with a longer tip. As Freitag et al. discussed, the point monopole approximation in equation (1.147) is only valid in the corridor of spatial frequencies where its value is close to one [76]. A true monopole response is achieved with an infinitely long and thin cylinder. However in most experimental situations only a certain range of spatial frequencies is relevant. On the low spatial frequency end the scanning window dimensions define a cutoff and on the high spatial frequency side scanning at a height z_0 already introduces a spatial low pass filter $e^{-k(z_t+\Delta z_{\text{mono}})}$ in the field transfer function.

Torque term A full description of the forces acting on a magnetic NW scanning probe tip requires to introduce an additional torque term in the case of low spring constants as shown by Rossi et al. [12]. If $\mathbf{m}_{\text{tip}}$ is the dipole moment of the tip the torque is given by $\boldsymbol{\tau} = \mathbf{m}_{\text{tip}} \times \mathbf{B}(\mathbf{r}_t, z_t + \Delta z_{\text{dip}})$. The full force acting on the NW tip is then given by expanding equation (1.144)

$$\begin{aligned}\mathbf{F}(\mathbf{r}_t, z_t) = \mu_0 \Big\{ & q_{\text{tip}} \mathbf{H}(\mathbf{r}_t, z_t + \Delta z_{\text{mono}}) + \mathbf{m}_{\text{tip}} \nabla \cdot \mathbf{H}(\mathbf{r}_t, z_t + \Delta z_{\text{dip}}) \\ & + \frac{1}{l_{\text{eff}}} \hat{\mathbf{n}} \times [\mathbf{m}_{\text{tip}} \times \mathbf{H}(\mathbf{r}_t, z_t + \Delta z_{\text{dip}})] \Big\}\end{aligned} \tag{1.148}$$

where $\hat{\mathbf{n}}$ is pointing along the NW-axis and l_{eff} is the effective length. For long cantilevers the torque term is suppressed by the prefactor $1/l_{\text{eff}}$ and becomes only relevant for short and soft NWs with a large dipole moment at the tip.

The force acting along the mode directions of the NW is then $F_i = \hat{\mathbf{r}}_i \cdot \mathbf{F}(\mathbf{r}_t, z_t)$. For a magnetic driving field at resonance the amplitude response of the NW resonator is directly proportional to the force

$$F_i = \frac{1}{\chi(\omega_i)} r_i = \frac{k_i}{Q_i} r_i. \tag{1.149}$$

where r_i is the oscillation amplitude. Measuring the displacement response to a known resonant stray field excitation allows to fit for the free parameters of equation (1.148),

[24] $J_1(y) = \frac{y}{2} - \frac{y^3}{16} + \dots$

namely q_{tip}, $\mathbf{m}_{\mathrm{tip}}$, Δz_{mono} and Δz_{dip}, calibrating the tip response e.g. with AC current carrying lines [12, 13].

This procedure has been used for MFM probes on cantilevers with DC current lines and rings of different sizes [72, 92–95]. For an extended tip volume the monopole values q_{tip} and Δz_{mono} depend on the scanning height and the separation between two lines, since the effective volume of the tip interacting with the stray field changes. In terms of the force transfer function $\sigma_{\mathrm{tip}}(\mathbf{k})$ they exhibit a clear non-constant dependence on spatial frequency and do not agree with a perfect monopole model. The response of iron filled CNTs as probes on the cantilever end however conforms to a monopole behavior, as the value of the fitted monopole charge does not depend on the separation between the current lines [72].

1.3.3. Sensitivity and spatial resolution

The sensitivity to magnetic field can be estimated by assuming a thermally limited measurement as discussed in Section 1.2.3. One has to differentiate between the exact tip models. While a monopole tip can transduce a resonant stray field excitation directly to *oscillation amplitude* as discussed in the previous section, a dipole tip oscillation amplitude responds to field gradient at resonance. For DC fields the *frequency shift* is proportional to field gradient in the monopole model and to the second field derivative in the dipole case. These relations are summarized in Table 1.1. The DC case is subject to the constraint of small oscillation amplitudes so that the field gradient is probed locally and the derivative can be linearized. For a dipole tip the direction of $\mathbf{m}_{\mathrm{tip}}$ with respect to the mode direction is crucial to whether the mode responds to the stray field [12].

Pushing the lateral spatial resolution to smaller scales has been an ongoing effort in MFM and resolutions down to 10 nm have been achieved [96]. The focus lies mainly on producing very sharp tips, that confine the magnetization to a small lateral volume and come close to the point-pole models, e.g. by engineering a vortex at the cantilever tip [97] or using extremely thin NWs attached to the lever [76]. The situation for NW MFM presents itself differently since the tip is oscillating in the xy-plane parallel to the surface and the displacement amplitude gives a lower boundary for the minimum spatial resolution. The second constrain is introduced by the scan height z_t above the sample surface and leads to spatial low pass filtering as discussed earlier. The third limitation is given by the type of tip model. A dipole-like tip responds better to higher spatial frequencies.

Hence designing the most suitable tip for a given sample requires balancing a lot of different and sometimes contradictory demands and is best discussed on a case by case basis. However the constrains of scan height including the effective offsets Δz_{mono} and Δz_{dip}, tip model and oscillation amplitude apply universally.

1.3.4. Separation of forces

For any scanning force probe the interpretation of the signal is difficult since contributions from many different sources need to be disentangled. The standard method for

Table 1.1. – **Sensitivity to magnetic field and field gradients**
Below are the field and field gradient sensitivities of point pole probes listed for the cases of DC and resonant excitation (AC) by the probed magnetic stray field. Note that the measured quantity in AC is the resonant oscillation amplitude, while in the DC case it is frequency shift.

	monopole	dipole
DC	$\left(\frac{\partial B}{\partial r_i}\right)_{\min} = \frac{1}{q_{\text{tip}} r_i}\sqrt{4k_B T \frac{M\omega_i}{Q_i}}$ [T/m$\sqrt{\text{Hz}}$]	$\left(\frac{\partial^2 B}{\partial r_i^2}\right)_{\min} = \frac{1}{\lvert\mathbf{m}_{\text{tip}}\rvert r_i}\sqrt{4k_B T \frac{M\omega_i}{Q_i}}$ [T/m$^2\sqrt{\text{Hz}}$]
AC	$B_{\min} = \frac{1}{q_{\text{tip}}}\sqrt{4k_B T \frac{M\omega_i}{Q_i}}$ [T/$\sqrt{\text{Hz}}$]	$\left(\frac{\partial B}{\partial r_i}\right)_{\min} = \frac{1}{\lvert\mathbf{m}_{\text{tip}}\rvert}\sqrt{4k_B T \frac{M\omega_i}{Q_i}}$ [T/m$\sqrt{\text{Hz}}$]

MFM is the lift mode, in which any line is scanned twice at different heights. The first pass very close to the surface images mostly the topography, while the second pass at a lift height of a few tens of nanometers captures mainly the magnetic field contrast, due to the different distance dependencies of the electrostatic and magnetic potentials [98]. Another way to distinguish between electrostatic and magnetic contrast is the combination of simultaneous magnetic and Kelvin probe force microscopy, which enables real time compensation of the electrostatic potential [99]. A third option works by applying exactly the coercive field of the tip, resulting in a demagnetized probe, and acquiring a topographic image [100].

In general if the magnetic properties of tip and sample are suitable any combination of inverting one and keeping the other constant, that is if there are differences in coercive field, can be used to separate the magnetic contrast. The most powerful method was already hinted at in Section 1.3.2 and consists of moving the magnetic contrast away from DC to a defined frequency as first performed by Schönenberger et al. [101]. In terms of NW-MFM this requires that the magnetic signal can be modulated up to the NWs resonance frequencies which usually are in the range of a few hundred kHz and makes it especially suitable to image current densities instead of static magnetization.

1.3.5. Dissipation

In scanning force measurements dissipation is usually understood as the additional external energy loss during one oscillation cycle by the energy transferred between tip and sample, compared to the free free energy loss of the resonator. The power dissipated during one period at resonance is given by

$$P_0 = \frac{\Delta W}{\Delta t} = \frac{\omega_0}{2\pi}\Delta W = \frac{\omega_0}{2\pi}\frac{2\pi W}{Q} = \frac{1}{2}\frac{M\omega_0^3}{Q}r^2 = \frac{1}{2}\Gamma\omega_0^2 r^2 \tag{1.150}$$

where we have used the definition of the quality factor (1.64). Maintaining a fixed oscillation amplitude thus requires to excite the resonator constantly with the power above. Let us now consider the equation of motion of a harmonic oscillator subject to a tip-sample interaction force F_{ts} while being driven by F_d

$$M\ddot{r}(t) + \Gamma_0\dot{r}(t) + k_0 r(t) = F_d(t) + F_{\mathrm{ts}}(t) \tag{1.151}$$

and $k_0 = M\omega_0^2$ is the spring constant. The tip sample force can be expanded around the equilibrium position as shown in Section 1.2.4. Additionally we will introduce a phenomenological dissipation term proportional to the velocity so that $F_{\mathrm{ts}} = \frac{\partial F_{\mathrm{ts}}}{\partial r}\big|_0 r - \Gamma_{\mathrm{ts}}\dot{r}$, using the same notation as above for the spatial. Inserting gives a modified equation of motion of the form

$$M\ddot{r}'(t) + [\Gamma_0 + \Gamma_{\mathrm{ts}}]\,\dot{r}'(t) + [k_0 - k_{\mathrm{ts}}]r'(t) = F_d'(t) \tag{1.152}$$

with a new dissipation $\Gamma' = \Gamma_0 + \Gamma_{\mathrm{ts}}$ and a new spring constant $k' = k_0 - k_{\mathrm{ts}} = k_0 + \frac{\partial F_{\mathrm{ts}}}{\partial r}\big|_0 = M\omega'^2$. Fourier transforming yields a modified mechanical susceptibility

$$\chi_{\mathrm{int}}(\omega) = \frac{\hat{r}'(\omega)}{\hat{F}'(\omega)} = \frac{1}{M[\omega'^2 - \omega^2] - i\Gamma'\omega}. \tag{1.153}$$

Now we consider the following experimental situation. The resonator is locked at resonance with a phase-locked loop (PLL). In the non-interacting case ($F_{\mathrm{ts}} = 0$) the dissipated power is given by equation (1.150) and $\omega_d = \omega_0$ for a driving force $F_d(t) = F_0 \cos \omega_d t$. Approaching closer to the surface eventually leads to tip sample interactions ($F_{\mathrm{ts}} \neq 0$) and the PLL drives the system at $\omega_d = \omega'$ with the driving force $F'(t) = F_0' \cos \omega_d t$. Note that ω' and Γ' are depending on the tip sample distance z_t. The power dissipated close to the surface during one period can be written analog to the free situation as

$$P' = \frac{1}{2}\Gamma' \omega'^2 r'^2 \tag{1.154}$$

where r' is the oscillation amplitude close to surface. This allows us to write the power dissipated by the tip sample interaction as the difference

$$P_{\mathrm{tip}} = P' - P_0 = \frac{1}{2}\left[\Gamma' \omega'^2 r'^2 - \Gamma_0 \omega_0^2 r^2\right] \tag{1.155}$$

At this point many useful forms can be derived, depending on the exact experimental situation. Let us first investigate the case of constant driving amplitude ($F_0 = F_0'$). From the susceptibility at resonance in the free and interacting case we find that

$$\Gamma' \omega' r' = \Gamma_0 \omega_0 r \tag{1.156}$$

Inserting and rearranging gives

$$P_{\mathrm{tip}} = \frac{1}{2}\Gamma_0 \omega_0^2 r^2 \left[\frac{\omega' r'}{\omega_0 r} - 1\right] \simeq P_0 \left[\frac{r'}{r} - 1\right] \tag{1.157}$$

where in the last step we approximated that $\omega'/\omega_0 \simeq 1$ in most cases. In general it holds that $0 \leq r' \leq r$ i.e. the oscillation amplitude in the interacting case is smaller than the free amplitude r. If $r' \simeq r$ the above equations gives $P_{\mathrm{tip}} \approx 0$, as one would expect for an oscillation amplitude that is almost undisturbed. For a large damping $r' \ll r$ we see that P_{tip} approaches P_0. In conclusion measuring the oscillation amplitude for fixed driving force provides access to the dissipated power.

In AFM and MFM measurements there is usually a second feedback loop employed, keeping the oscillation amplitude constant ($r' = r$) when approaching the surface. This has several advantages when scanning close and oscillating normal to the surface where the dissipation can be very large compared to the free case, requiring a large dynamic range. From the resonant conditions in both cases we get

$$\Gamma' \omega' F_0 = \Gamma \omega_0 F_0'. \tag{1.158}$$

and a similar relation can be found for the dissipated powers in terms of the driving forces

$$\begin{aligned} P_{\mathrm{tip}} &= \frac{1}{2}\Gamma_0 \omega_0^2 r^2 \left[\frac{\omega' F_0'}{\omega_0 F_0} - 1\right] \simeq P_0 \left[\frac{F_0'}{F_0} - 1\right] \\ &= P_0 \left[\frac{F_0' - F_0}{F_0}\right] = P_0 \left[\frac{A_0' - A_0}{A_0}\right] \end{aligned} \tag{1.159}$$

where in the last step we expressed the driving force in terms of driving amplitude directly proportional to the force and received the relation used mostly in AFM. Monitoring the excitation amplitude A_0' throughout the measurement reflects the dissipated power, if the oscillation amplitude r is locked. A third method of determining the dissipation experimentally is a measurement of the quality factor either by obtaining a thermal noise PSD or with ringdown techniques. They are relatively time consuming as compared to the dynamic readout but nonetheless useful for validating the dynamic data.

More difficult is finding an interpretation for the origin of the magnetic dissipation measurement. Often times one classifies the nature of the dissipation channel into two categories, hysteretic or velocity dependent [63]. Hysteretic behavior is present if the sample magnetization switches state during one oscillation cycle of the tip. Experimental clues are sharp peaks in the dissipation data at the location where the hysteretic switching takes place. Additionally there should also be a a dependence on scanning height since the magnitude of the tip field gets stronger for a closer scan, leading to more hysteretic events. Taking two consecutive scans each at different scan heights are a good method to identify hysteretic behavior. The second type is velocity dependent dissipation and was modeled above with a phenomenological tip-sample dissipation Γ_{ts}. Liu and Grütter for example could relate the magnetic dissipation to domain wall width oscillations of a NiFe thin film and a CoPtCr recording medium by introducing a frictional term in the equation of motion with the dissipation proportional to the square of the magnetostriction coefficients of the two materials [102, 103].

An additional challenge is the acquisition of clean dissipation contrast data itself. If the system transfer function is not characterized properly apparent dissipation effects can obscure the signal as shown by Labuda et al. [104, 105] and discussed in Section 2.3. Another type of seemingly true dissipation can originate from driving the resonator in the anharmonic regime where velocity- and position dependent terms can mix. A special case of of apparent dissipation in NW-MFM is the eigenmode rotation in the presence of shear forces described in Section 1.2.4, which can produce a signature of dissipation, when only considering one mode. It can be lifted by inspecting the data of both modes for a simultaneous dip and peak, that are simply a consequence of the changed projection onto the measurement vector.

The sensitivity of the amplitude measurement can be derived from the force response at resonance (1.149). Plugging in the minimum detectable force (1.94) on the right and side and solving for Γ gives

$$\Gamma_{\mathrm{min}} = \frac{1}{\omega_0 r} F_{\mathrm{min}} = \frac{1}{\omega_0 r} \sqrt{4 k_B T \frac{M \omega_0}{Q}} = \frac{1}{r} \sqrt{4 k_B T \frac{M}{\omega_0 Q}} \tag{1.160}$$

in units of $\mathrm{kg/s}\sqrt{\mathrm{Hz}}$. The most sensitive dissipation sensors have low mass, a high quality factor and a high resonance frequency.

2. Nanowire Force Microscope

In this chapter we will give an overview of the low temperature microscope used for nanowire force microscopy.

At first the operating principle and instrumentation will be described. Afterwards we discuss in detail the optical interferometer and motion detection capabilities of the microscope. In the last two parts we focus on different methods of actuation for a NW resonator and how the general measurement scheme employed for mapping in plane field gradients in a pendulum geometry is implemented.

2.1. Cryostat and instrumentation

The work horse of our nanowire force microscope is a vacuum and liquid nitrogen-shielded liquid helium bath cryostat fabricated by Precision Cryogenic System Inc. It is equipped with a superconducting magnet coil, which allows for the application of magnetic fields of up to 8 T in either direction along the vertical axis of the cryostat, using a Cryomagnetics 4G superconducting magnet power supply. The multi-walled cryostats interior can be pumped to a high vacuum of about 1×10^{-4} mbar and its outer chamber is filled with liquid nitrogen (LN_2), acting as a heat shield, while the inner chamber contains liquid helium (LHe) bath. A helium recovery line is connected to the inner chamber and fed back to the in-house helium liquifier. At a maximum filling the cryostat can be operated for 10 to 11 d, before it requires a new filling. The whole dewar rests on a tripodal, pressurized air-damped passive vibration isolation system. A full cooldown cycle takes roughly two days, including pumping to a small enough pressure and cooling down the entire probe to LHe temperature.

The actual scanning probe microscope is suspended with a four point copper beryllium spring system from a custom build insert manufactured mostly out of stainless steel. Connections at the top allow for attaching a turbo pump[1], 14 twisted pair lines, four radio frequency transmission lines and a few optical fibers (see Section 2.2). Additionally an ion pump[2] is part of the vacuum system and can hold the pressure in the case of room temperature operation, since the vibrations from the turbo pump would disturb the measurements. The bottom part of the insert consists of a copper disc to which a steel can with an indium seal can be affixed. This allows for operating pressures in the range of 2×10^{-7} to 8×10^{-7} mbar at room temperature. Cryogenic cooling lowers the pressure further during low temperature operation. The material choice of copper provides a direct interface to the LHe bath with an excellent thermal conductivity and is a crucial

[1] Agilent TPS compact turbo pumping station
[2] Agilent MiniVac

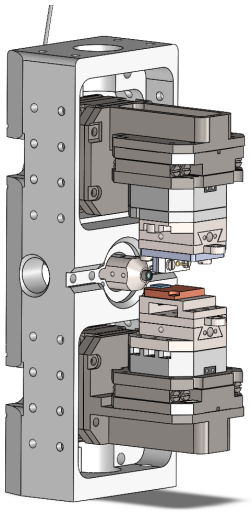

(a) Microscope

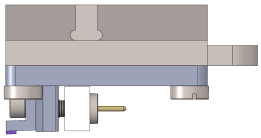

(b) Top stack holder

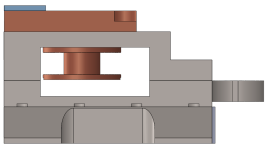

(c) Bottom stack holder

Figure 2.1. – **Nanowire scanning probe microscope**
(a) Rendering of the inner titanium frame of the NW scannning probe microscope. The top assembly is used to position a NW resonator with respect to the focal spot of the readout laser and the bottom stack to subsequently approach the sample of interest. (b) Detailed view of the NW holder. A chip with NWs facing upside down is glued at the lowermost part so that the NWs point downwards. A dither piezo used for actuation is pressed by a stamp towards the holder, which simultaneously serves as electrical contact. (c) Close-up of the sample stage. The sample of interest is glued edge-on on top of a copper plate. In the newer version, that is on display here, a heater coil is in direct contact with the sample plate and allows for precise control of the sample temperature.

part of the heat management. An extension of the copper disk acts as the anchoring point for the aforementioned spring system offering further passive vibration isolation, and four copper braids are ensuring a good thermal connection with the hanging part of the microscope.

Central to this section is a titanium frame on which the scanning units of the microscope are mounted. The positioning unit on the top half serves the purpose of placing a NW resonator into the focal spot of a custom build confocal fiber objective, described in detail later (Section 2.2.1). The unit consists of a stack of positioners and scanners, with steppers[3] for coarse navigation in all three directions and a 3D scanner[4] for fine positioning, providing a scan range of $30\,\mu m \times 30\,\mu m \times 15\,\mu m$ at 4 K. The same holds true for the bottom positioning unit with the exception that the scan control is handled by a 2D scanning unit[5], offering a scan rage of $10\,\mu m \times 10\,\mu m$ at LHe temperature, and that the fine approach of the sample of interest towards the NW resonator is controlled by applying an offset voltage to the bottom z-stepper providing a range of roughly 2 µm. Top and bottom piezo stack are each connected to a digital piezo control[6] unit with different modules[7] for every piezo, and the scanner voltages being supplied by a 16-bit analog output card with a BNC output panel[8]. The coordinate system used here is defined as follows: The z-axis is aligned vertically with the cryostat, the x-axis is parallel to the optical axis of the fiber objective and the y-axis perpendicular to it. Deviations in angle between the movement of the scanners and the coordinate system defined above are assumed to be below 1°.

The full microscope, without the surrounding copper parts, and close ups of the NW and sample holder are displayed in Figure 2.1. A picture of the entire assembly can be found in the Appendix Figure A.1. The NW chip is mounted on top of a L-shaped sample holder which in turn is fixed to the top stack holder as shown in Figure 2.1b. This leaves the NWs facing upside down and being the lowest extension point of the entire top assembly. At the back of the NW holder a small dither piezo disk is pressed into a suitable notch. The stamp providing the pressure simultaneously serves as electrical contact to the disk. In a more recent version of the microscope the dither piezo actuation unit was removed completely in order to excite the NWs mechanical motion optically (Section 2.3.1). On the bottom half of the microscope the sample of interest is glued close to the edge of a copper plate. Once mounted to the titanium holder piece it constitutes the highest point of the bottom assembly.

In a usual measurement run one of the NW sensors is first brought into the focal spot of the readout laser. Subsequently the sample of interest is carefully moved closer towards the NW resonator. This illustrates a major challenge for NW force microscopy measurement in the pendulum geometry. The sample of interest needs to be located at the very edge of the sample chip in order to still provide optical access to the NW

[3] Attocube ANPx300
[4] Attocube ANSxyz100lr
[5] Attocube ANSxy100
[6] Attocube ANC300
[7] Steppers ANM150, scanners ANM 200, stepper/scanner ANM300
[8] National Instruments PXI-6733 and BNC-2110

resonators from the side while scanning, even when the two chips are in close proximity. In practice this constrains the accessible area to a stripe on the sample chip reaching from the front edge to about 30 to 40 µm inwards. The precise value depends mainly on the length of the NW sensor, the position of the focal spot along the NW axis and the properties of the readout laser beam. Scanning too far inside of the sample chip gradually leads to a loss of interference contrast and a modulation of the incident power on the NW, which both affect the measurement in various undesirable ways. For example in some NW probes the elastic modulus depends decidedly on temperature thus leading to an additional power dependent frequency shift as incident light of varying intensity will be absorbed during a measurement.

2.1.1. Temperature control

Thermal management is an integral part of cryostat operation. In order to exert precise control over the sample temperature, sources and sinks of heat must be understood and balanced in a way that leads to a desired outcome in terms of operating ranges and the achievable rate of cooling or heating.

In our cryostat we ideally aim for the top stack, containing the NW sample, to be at the lowest possible temperature to boost sensitivity, while at the same time being able to exercise good control over the temperature of the sample of interest. Without the presence of exchange gas our microscope was limited to a fixed sample temperature of roughly 11 K. Two measures were taken to provide a broader operating temperature range on both ends of the scale. Firstly, with the addition of a heater stage (Figure 2.1c), consisting of a copper bobbin with approximately 2 m of twisted Constantan wire coiled up in a way so that opposing segments cancel their Biot-Savart fields and fixated with Stycast, we are able to access temperatures of 50 K by passing an open loop DC current through the coil. For a precise temperature readout a calibrated temperature sensor[9] is mounted with vacuum grease[10] inside a bore at the center of bobbin and its four way resistance is converted to temperature. The copper plate containing the sample of interest is in direct contact with the top part of the bobbin aided by another small application of vacuum grease. In this fashion we can assume that the measured temperature is indeed very close to the actual sample temperature, especially with diffusive heat transport being eliminated by the high vacuum in the sample chamber. Secondly, with the goal to decrease the minimum operating temperature, a soft copper braid is routinely placed on the back edge of the copper sample plate and anchored at the lower copper base plate of the microscope. It is fixed tightly with the same titanium screw that was previously used.

These two additions allow for a minimum sample temperature[11] of about 4.7 K, close to the LHe bath temperature, and a maximum (confirmed) value of 50 K. Higher values might be possible by increasing the heating current further. In terms of heating and

[9] Lakeshore Cernox® (CX-SD packaging)

[10] Apiezon N

[11] To clarify the NW temperature will still equilibrate at roughly 11 K since no additional copper braid is added to the top stack.

cooling rates the temperature settles within a few minutes to a new value, with a slight asymmetry between heating and cooling. The latter is taking effect on a faster time scale than the former. Regarding the NW's temperature on the top stack, we place a very thin and soft copper wire from the frame at the top, to electrically ground the holder and hopefully cool the sample holder closer to base temperature. However the deciding factor influencing the NW temperature would in any case be the power absorbed from the readout laser combined with the optical driving laser (see Section 2.3.1).

Apart from the low cryogenic operating temperatures described above it is possible to operate the microscope at 77 K by filling the LHe chamber with LN_2 and obviously also at room temperature. In these two cases however we are lacking the ability of applying magnetic fields as the superconducting magnet coil requires LHe temperatures.

2.2. Optical interferometer and motion detection

Detecting the mechanical motion of a resonator employed in force measurements is at the heart of any atomic or magnetic force microscopy instrument. There exist a host of different detection techniques for the motion of a standard cantilever [90] ranging from electron tunneling current, capacitive, piezoresistive [106], and piezoelectric [107–109] to optical techniques of beam deflection [1, 110] and interferometry [58, 111, 112]. In most standard instrumentation the optical techniques prevail due to their ease of application. Smaller resonators approaching the nanoscale however require more advanced methods. Doubly clamped beam resonators have been measured, apart from optical techniques, by capacitive coupling to microwave resonators [113], an AC current passing through the device [114, 115] and more exotically even by coupling them to a SQUID [116] or using a cantilever scanning probe to image the vibration modes of a carbon nanotube [117]. Another class of force sensors, which received a lot of attention recently, are ultra thin SiN membranes, engineered to exhibit record high quality factors by exploiting soft clamping and dissipation dilution [118]. It is very challenging however to build a robust scanning probe platform out of these type of membranes [119]. Doubly clamped or membrane resonators do not provide the geometric flexibility that singly clamped levers can offer with simply scanning the sample of interest below the free end.

The vibrational modes of nanoscale resonators with a free, vibrating end have also been measured by a variety of techniques, for example inside a scanning electron microscope [51, 120, 121], with a microwave cavity [122], optically from the side in transmission [48, 123], reflection [11–13, 46, 47, 124, 125], inside an optical cavity [35, 126] and from the top [127, 128]. Piezoelectric or resistive techniques are not applicable at this scale due to the small piezoelectric response.

In our system we chose a fully fiber coupled interferometer with a confocal objective and detection from the side, due to its mechanical robustness, space requirements and ease at operation at cryogenic temperatures [129, 130]. A schematic sketch of the basic components along the optical path is shown in Figure 2.2. A laser diode head[12] provides the laser beam used for the interferometric motion detection at a center wavelength of

[12]Toptica DFB pro, maximum power 36 mW

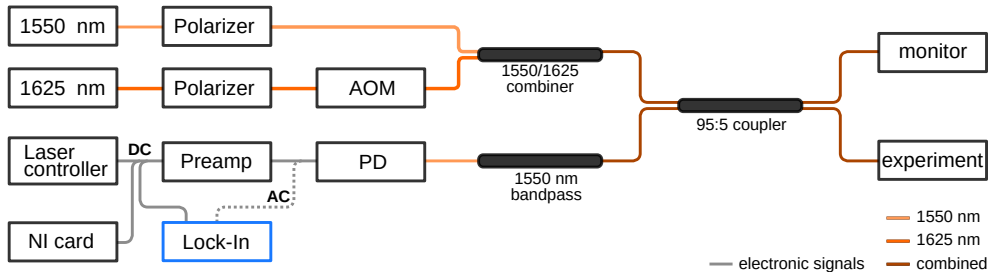

Figure 2.2. – **Optical signal path**
Sketch of the all fiber-coupled optical signal path displaying the most important elements. The interferometer is instituted by the 95:5 fiber optic coupler. At the signal arm (bottom left) the interference signal is converted a voltage and its DC and AC part are analyzed further or used for feedback and measurement control. PD: Photodiode, AOM: Acousto-optic modulator.

1550 nm. Its temperature and current set points are controlled and maintained via a digital laser controller[13]. The wavelength can be tuned by changing the diode temperature over a window of roughly 4 nm around the center wavelength[14] while the current dependence of the wavelength is negligible[15].

Following the output of the diode the light is attenuated by one or several fixed fiber optic attenuators[16] in series depending on the power desired at the NW resonator. Subsequently it passes a 3-paddle polarization controller[17] before entering a wavelength division multiplexer[18]. Its function is to combine the light used for the interferometer at 1550 nm wavelength with a second laser beam at a wavelength of 1625 nm required for optically driving the NWs motion (see Section 2.3.1 for details). The interferometer itself consists of a single mode fused fiber coupler[19] with a coupling ratio of 95:5. The smaller fraction of the incident light is guided into the cryostat and focused onto the NW resonator, while the bigger part can be used to monitor the laser power. At the experiment arm, the reflected and collected light follows the same path in the opposite direction passing the fiber optic coupler a second time, where the major amount of light is directed towards the signal arm of the interferometer. Here the 1625 nm light is filtered out by a 1550 nm bandpass filter[20] with a pass band width of 4 nm, a stop bandwidth of 10 nm and an isolation at 1625 nm bigger than 35 dB. The remaining

[13] Toptica DLC pro
[14] Temperature coefficient: $0.099\,\mathrm{nm\,K^{-1}}$
[15] Current coefficient: $0.007\,\mathrm{nm\,mA^{-1}}$
[16] e.g. FA15T-APC for 15 dB attenuation
[17] Thorlabs FPC560
[18] Thorlabs WD1525A
[19] CSRayzer SMC-1550-2x2-5/95-3.0x45-SMF28e-S-1-S
[20] GEHT International BPF-1550-4-10-22-LL-1

light is converted to a voltage signal by a photoreceiver[21] offering a low noise gain from 1×10^2 to $1\times10^7\,\mathrm{V\,A^{-1}}$ and a response of roughly $1\,\mathrm{A\,W^{-1}}$. At a gain of $1\times10^6\,\mathrm{V\,A^{-1}}$ its bandwidth is 1.8 MHz, comfortably exceeding most of the NWs resonance frequencies. Additionally it provides a low pass cutoff filter either working with the gain dependent full bandwidth, 10 MHz or 1 MHz. If not stated otherwise, the latter setting is used.

All fibers in use are single mode fibers and all connector interfaces are of the AF/APC type, in order to avoid spurious reflections along the optical path. As compared to a previous iteration of the interferometer, we moved away from polarization maintaining fibers. Empirically standard single mode fibers turn out to be more robust against small temperature and pressure changes, which can drastically affect the polarization state of the light guided through the fiber in the polarization maintaining case. This is especially relevant since the amount of light scattered back by the NW resonator highly depends on the polarization of the incident light. Ideally the incoming polarization state is aligned with the NW-axis [34]. This can now be achieved simply by varying the polarization of the 1550 nm laser at the input arm of the interferometer, maximizing the reflected signal. The polarization will inevitably vary while traveling through the single mode fiber, but it is nonetheless a fixed, deterministic function of the input state, once the temperature inside the cryostat has settled [130]. Also in addition to the NIR fiber coupler there exists a second one covering the visible part of the spectrum, centered around a wavelength of 635 nm and with a coupling ratio of 50:50.

Moving on, the AC and DC part of the signal are led to a host of instruments for monitoring and measurement control. The DC part is further amplified by a low noise preamplifier[22], usually with a gain of 10 and the low pass filter set to 100 Hz, and passed to the laser controller, an auxiliary input of a lock-in amplifier[23] and a data acquisition card[24]. The AC part is directly connected the lock-in amplifier for analyzing the dynamical part of the optical signal.

2.2.1. Confocal objective

The confocal objective inside the cryostat consists of a titanium body, a glass ferrule and two lenses for collimation[25] and focusing[26]. During fabrication first step the collimating lens is fixed in place with glue[27]. Then the loose and stripped end of the fiber[28] at the experiment arm of the coupler is fed through a glass ferrule and cleaved afterwards. While monitoring the the collimation of the beam we fix the fiber and the ferrule to titanium part. Finally the focusing lens is put into place and the objective can be mounted inside the cryostat.

[21] Femto OE-300-IN-01-FC
[22] Stanford Research Systems SR560
[23] Zurich Instruments UHFLI
[24] National Instruments PXIe-6361 and BNC2090A
[25] Thorlabs 354430-C, NA = 0.16, f = 5.00 mm, CA = 1.60 mm
[26] Thorlabs 354140-C, NA = 0.58, f = 1.45 mm, CA = 1.60 mm
[27] TorrSeal
[28] Corning SMF28e, NA = 0.14, MFD = 10.4(5) µm, effective group index of refraction 1.4679

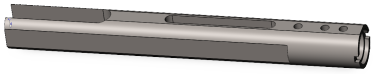

(a) Titanium body of the confocal microscope

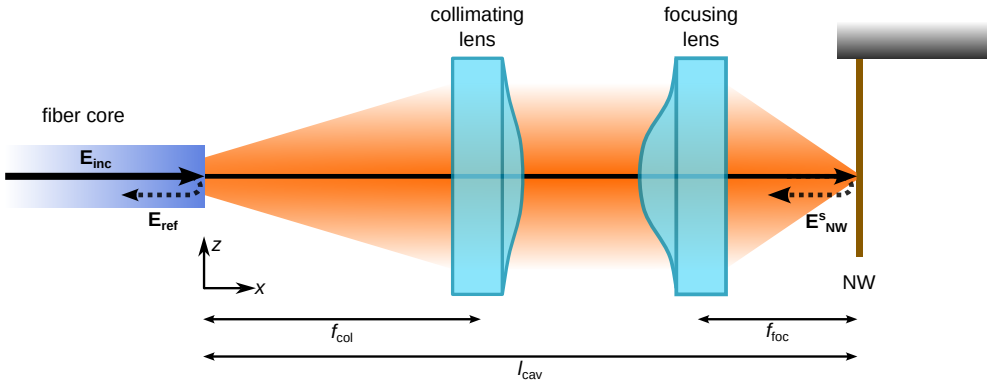

(b) Cleaved fiber end and lenses

Figure 2.3. – **Confocal objective**
(a) Titanium body which guides the loose fiber at the experiment arm with the help of a glass ferrule, centering it with respect to its long axis. A collimating and a focusing lens are glued on the right hand side. (b) Illustration of the optical elements at the cleaved end of the fiber.

The effective numerical aperture (NA) of the objective is a measure of its lateral spatial resolution and is roughly 0.44. This is due to the NA mismatch between the fiber and the collimating lens, causing the beam diameter to fall slightly short of the clear aperture (CA) of the lenses. The choice of lenses is a compromise between a sufficiently small focal spot and a reasonable working distance to allow for a big enough margin to navigate with the positioners without causing accidental damage to the focusing lens or the sample. The mode field diameter (MFD) of the fiber core serves as a pinhole and defines the minimum focal spot achievable with this configuration, resulting in a value of 1.53 µm. As a consequence the NW motion is integrated across a narrow section of its length. Since most of the NW probes employed have a length of roughly 10 µm or above it is possible to image the mode shape by moving along the NW axis.

2.2.2. Interference signal

Figure 2.3b depicts a sketch of the optical elements at the experiment arm of the fiber coupler. The incoming beam denoted $\mathbf{E}_{\mathrm{inc}}$ gets reflected at the fiber end. The transmitted part travels through the confocal objective and illuminates the NW, while the reflected part $\mathbf{E}_{\mathrm{ref}}$ constitutes the reference arm of the interferometer. We can link the two components by $\mathbf{E}_{\mathrm{ref}} = \sqrt{R_{\mathrm{core}}}\mathbf{E}_{\mathrm{inc}}$, where R_{core} is the Fresnel reflectivity for normal incidence of the fiber core boundary with vacuum. Numerically this gives a value of $R_{\mathrm{core}} \approx 3.6\,\%$. In practice we have found a good agreement with a value of 3.2 % for the objective currently mounted inside the microscope. Losses are easily explained by an imperfect interface.

The reference part interferes with the light reflected from the NW. Passing through the confocal objective in the backwards direction the scattered light couples into the fiber with another loss ($\sqrt{1-R_{\mathrm{core}}}$) due to Fresnel reflection. Relating it to the incoming part we can write $\mathbf{E}_{\mathrm{NW}} = \sqrt{1-R_{\mathrm{core}}}\ \mathbf{E}^{\mathrm{s}}_{\mathrm{NW}} = [1-R_{\mathrm{core}}]\sqrt{R_{\mathrm{NW}}}\ \mathbf{E}_{\mathrm{inc}}$, where R_{NW} expresses the effective reflectivity of the NW. Since the reflectivity of the NW is in general rather poor one can consider the experiment arm as a very low finesse Fabry-Pérot cavity.

NW scattering The scattering problem of light interacting with a NW resonator can be treated in the framework of Mie theory. An extensive study of the problem of light scattering on a cylinder of infinite length is given by Bohren and Huffman in section 8.4 of their excellent book *Absorption and scattering of light by small particles* [131]. A short overview is given in the Appendix Section B. The incoming and scattered fields can be related by an amplitude scattering matrix by expanding them in vector cylindrical harmonics and imposing the boundary conditions at the interface between vacuum and cylinder. From this the scattering cross section can be calculated. It depends on the wavelength λ of the incoming light, the radius R of the cylinder and its refractive index. In general the scattering cross section exhibits a very rich behavior especially when the cylinder radius approaches the dimension of the wavelength or the refractive index depends strongly on wavelength. In our experiments R is usually smaller than $\lambda = 1550\,\mathrm{nm}$ by at least one order of magnitude. By fulfilling this condition it emerges that

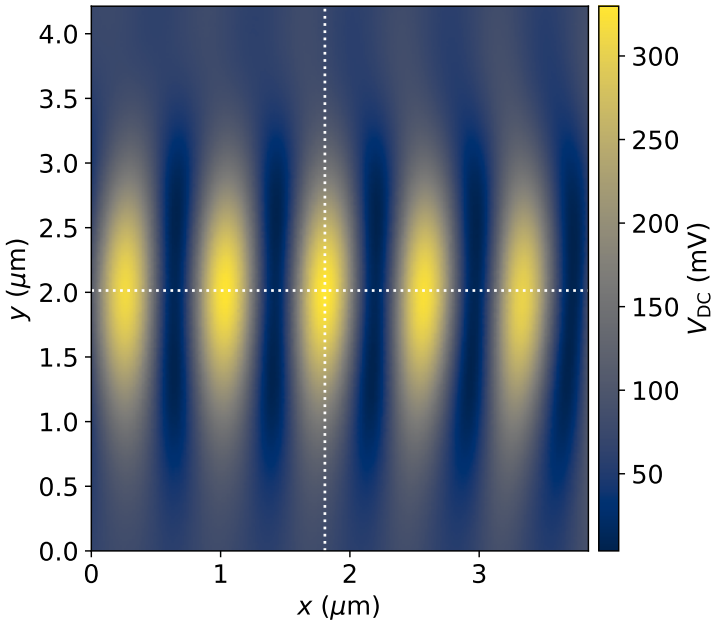

Figure 2.4. – 2D cavity scan
Scan of a NW resonator inside the low finesse Fabry-Pérot cavity constituted by the NW and the fiber end. The plotted signal is the DC output of the photoreceiver. Along the x-axis, which coincides with the optical axis, interference fringes with a periodicity of $\lambda/2$ emerge as the cavity length is changed by moving the NW. In the y-direction one can observe the waist profile of the gaussian beam at the focal spot. Taking the indicated line cuts one can fit the on-axis cavity response and the beam waist parameter w_0.

backscattering is greatly enhanced if the polarization direction of the incoming light is aligned with the NW axis [34] as mentioned before.

The incoming light interacting with the NW can be described as a Gaussian beam in paraxial approximation with the beam waist parameter w_0 fully determining the amplitude profile along the optical axis. For a beam polarized in z-direction and propagating along the x-axis it is given by [132]

$$E(x,z) = \sqrt{1-R_{\text{core}}}E_{\text{inc}}\hat{\mathbf{z}}\frac{w_0}{w(x)}e^{-\frac{z^2}{w^2(x)}}e^{i\phi(x,z)} \tag{2.1}$$

where

$$w(x) = w_0\sqrt{1+x^2/x_{\text{R}}^2} \tag{2.2}$$

$$\phi(x,z) = kx - \eta(x) + kz^2/[2R(x)] \tag{2.3}$$

is the beam radius with the relation $x_{\text{R}} = kw_0^2/2$ defining the Rayleigh range and $k = 2\pi/\lambda$. The additional phase terms in $\phi(x,z)$ are the wavefront radius $R(x)$ and the phase correction $\eta(x)$

$$R(x) = x[1+x_{\text{R}}^2/x^2] \tag{2.4}$$

$$\eta(x) = \arctan(x/x_{\text{R}}). \tag{2.5}$$

The Gaussian characteristics of the focused laser beam can be probed by scanning the NW inside the focal spot and recording the DC response of the cavity as show in Figure 2.4. Since the condition for the NW radius $R \ll w_0$ is usually fulfilled the interaction of the NW with the Gaussian beam can be approximated by plane waves and the NW acts as a local probe of the amplitude. From the response in y-direction we can extract the beam waist w_0 by applying a Gaussian fit function (see Figure 2.5b). Noting that for our confocal setup detects the transverse coherent spread function $\text{CSF}_{\text{total}} = \text{CSF}_{\text{illum}}\text{CSF}_{\text{det}}$ [21], where we measure the total part $\text{CSF}_{\text{total}}$. However to determine the waist of the illuminating beams only $\text{CSF}_{\text{illum}}$ is of importance. Since the illuminating and detectec coherent spread functions coincide in our case (moving though the same objective with the fiber end acting as a pinhole) we have $\text{CSF}_{\text{illum}} = \sqrt{\text{CSF}_{\text{total}}}$ and in order to get the correct beam waist we have to consider the square root of the intensity profile shown in Figure 2.5b. This results in values for the illuminating beam of FWHM = 2.194(8) µm and $w_0 = 1.863(7)$ µm.

Interference contrast The interference contrast can be derived from the two fields at the fiber end. We will only consider first order terms because of the poor reflectivities involved. Since for normal incidence on the NW the two degrees of polarization do not mix in the scattering process we can assume that $\mathbf{E}_{\text{ref}}$ and $\mathbf{E}_{\text{NW}}$ are aligned. The general form if the interference consists of the sum of the intensities of both fields and the interference term [133]

$$P_{\text{signal}} = |\mathbf{E}_{\text{ref}}|^2 + |\mathbf{E}_{\text{NW}}|^2 + 2\Re(\mathbf{E}_{\text{ref}} \cdot \mathbf{E}_{\text{NW}}). \tag{2.6}$$

Plugging in the expressions from above in terms of the incident light and dropping vector notation yields

$$P_{\text{signal}} = E_{\text{inc}}^2 \left\{ R_{\text{core}} + [1 - R_{\text{core}}]^2 R_{\text{NW}} + 2[1 - R_{\text{core}}] \sqrt{R_{\text{NW}} R_{\text{core}}}\ \Re(e^{i\delta}) \right\} \tag{2.7}$$

where $\delta = 2\pi/\lambda\ 2l_{\text{cav}}$ is the phase difference acquired between the two fields given by twice the cavity length l_{cav} times the wave vector. By noting $R_{\text{core}}, R_{\text{NW}} \ll 1$ we can omit the terms $\propto (1 - R_{\text{core}})$ and obtain

$$P_{\text{signal}} \approx E_{\text{inc}}^2 \left[R_{\text{core}} + R_{\text{NW}} + 2\sqrt{R_{\text{NW}} R_{\text{core}}} \cos\left(\frac{2\pi}{\lambda} 2l_{\text{cav}} \right) \right]. \tag{2.8}$$

Following [21] equation (2.8) can be reformulated by defining the powers $P_{\text{avg}} = (R_{\text{core}} + R_{\text{NW}}) E_{\text{inc}}^2$ and $P_{\text{amp}} = 2\sqrt{R_{\text{core}} R_{\text{NW}}} E_{\text{inc}}^2$, which describe a slowly varying envelope and a fringe term oscillating with the x-position of the NW along the optical axis, respectively. Inserting yields

$$P_{\text{signal}} \approx P_{\text{avg}} \left[1 + \nu \cos\left(\frac{2\pi}{\lambda} 2x \right) \right] \tag{2.9}$$

where we have defined the visibility of the interferometer as follows

$$\nu = \frac{P_{\text{amp}}}{P_{\text{avg}}} = \frac{2\sqrt{R_{\text{core}} R_{\text{NW}}}}{R_{\text{core}} + R_{\text{NW}}}. \tag{2.10}$$

From this we can easily see that the visibility approaches the maximum possible value of $\nu = 1$ if the reflectivities are equal ($R_{\text{core}} = R_{\text{NW}}$). In practice we observe a very good match obtaining fringe visibilities of up to 0.96 routinely with Si NW resonators [16], since the cleaved fiber naturally fulfills the above condition. No further processing is needed to enhance the fiber end reflectivity.

2.2.3. Calibration of nanowire displacement motion

The voltage measured at the photoreceiver is directly proportional to the incident optical power. Rewriting equation (2.9) gives the measured signal

$$V_{\text{signal}}(x) = V_{\text{avg}}(x) \left[1 + \nu \cos\left(\frac{2\pi}{\lambda} 2x \right) \right] \tag{2.11}$$

and we can extend the definition of the visibility in terms of the fringe minimum and maximum as follows

$$\nu = \frac{P_{\text{amp}}}{P_{\text{avg}}} = \frac{2\sqrt{R_{\text{core}} R_{\text{NW}}}}{R_{\text{core}} + R_{\text{NW}}} = \frac{\frac{1}{2}[V_{\text{max}} - V_{\text{min}}]}{\frac{1}{2}[V_{\text{max}} + V_{\text{min}}]}. \tag{2.12}$$

Figure 2.5a depicts the fringe pattern emerging by moving the NW along the optical axis. The fit to equation (2.11) agrees reasonably well by introducing the Lorentzian behavior of $V_{\text{avg}}(x) = V_0/[1 + x^2/x_0^2]$. The Rayleigh range x_0 is found to be $x_0 = 5.10(21)\,\mu\text{m}$,

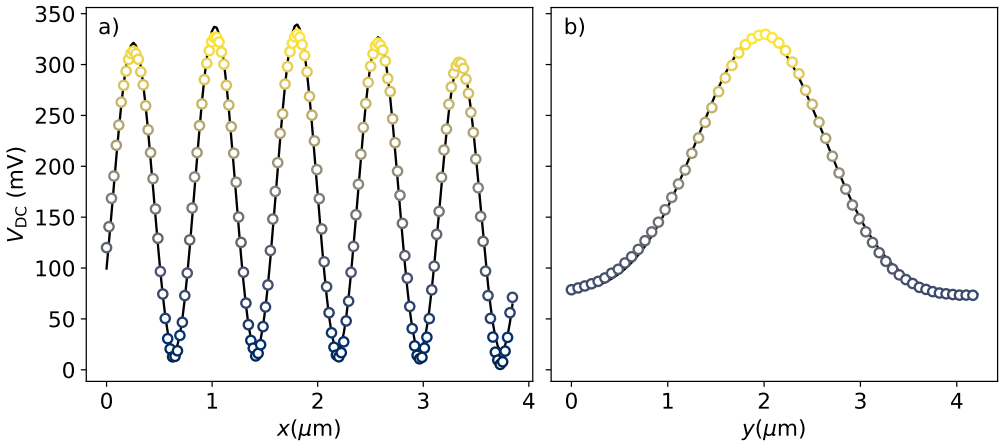

Figure 2.5. – **Cavity line cuts**
Line cuts along the x- and y-direction of the 2D cavity scan shown in Figure 2.4. (a) The cavity response along the optical axis can be fitted (solid black line) using equation (2.11) introducing a Lorentzian profile for the amplitude $V_{\mathrm{avg}}(x) = V_0/(1 + x^2/x_{\mathrm{R}}^2)$. The resulting fit values are $V_0 = 166.0(10)\,\mathrm{mV}$ and $x_{\mathrm{R}} = 5.10(21)\,\mu\mathrm{m}$, while the wavelength $\lambda = 1550\,\mathrm{nm}$ and $\nu = 0.968$ were fixed to their known and calculated (from V_{min} and V_{max}) values, respectively. (b) Fitting the data in with a Gaussian profile (black, solid line) results in a full width at half maximum of $\mathrm{FWHM}^{\mathrm{det}} = 1.551(6)\,\mu\mathrm{m}$. The beam waist is defined as the width at which the intensity drops to $1/e^2$ and is related to the FWHM by $w_0^{\mathrm{det}} = \mathrm{FWHM}^{\mathrm{det}}/\sqrt{2\ln 2} = 1.318(5)\,\mu\mathrm{m}$.

which disagrees with the value calculated from the beam waist $\pi w_0^2/\lambda = 7.04(5)\,\mu\text{m}$ found from the line cut in y-direction (see Figure 2.5b). The most likely explanation is that the cavity scan does not extend over a wide enough range along x to fully capture the Lorentzian form of the focal spot.

The dynamic motion of the NW resonator is imprinted to the signal by a very faint modulation of the cavity length at the NWs resonance frequencies. We can write $x = x_0 + \delta x(t)$, where x_0 is the working point of the interferometer and $\delta x(t)$ describes the small dynamic changes that we are interested in. The sensitivity of the transduction from $\delta x(t)$ to a voltage signal $\delta V_{\text{signal}}(t)$ is highest at the inflection points of equation (2.11) imposing the condition $\frac{2\pi}{\lambda} 2x = [n + \frac{1}{2}]\pi$ with $n \in \mathbb{Z}$. This leads to periodic inflection points at $x_0 = \frac{\lambda}{8} + \frac{\lambda}{4} n$. In order to work with the highest sensitivity we usually choose a point very close to the focal spot with either positive or negative slope. Since in general $\delta x(t) \ll \frac{\lambda}{4}$ holds and under the additional assumption that the NW resonator is not deflected statically by a strong force, the signal can be linearized around the inflection points yielding together with equation (2.12)

$$\left.\frac{dV_{\text{signal}}}{dx}\right|_{x=x_0} = \pm\frac{4\pi}{\lambda}\nu V_{\text{avg}} = \pm\frac{2\pi}{\lambda}[V_{\max} - V_{\min}] \tag{2.13}$$

with the sign depending on the slope. The above quantity defines the conversion factor between displacement and the measured voltage and is usually of the order of roughly $10\,\mu\text{V}\,\text{nm}^{-1}$. Its uncertainty is given by the precise knowledge of the wavelength and the error in the voltage measurement. The interferometer sensitivity can be boosted by increasing the incident laser power up to a limit where bolometric heating influences the properties of the NW or radiation back-action effects set in [124]. We routinely monitor for back-action effects by comparing the thermal noise limited PSDs on either side of the fringe. Incident powers used are usually in the range of 0.5 to $10\,\mu\text{W}$ in order to keep the interferometer in the linear range.

A second way of tuning the interferometer to the working point makes use of the dependence of the laser wavelength on the diode temperature. By positioning the NW inside the focal spot and sweeping the temperature of the laser diode across a range of several °C we obtain a fringe pattern as shown in Figure 2.6. Identifying a suitable inflection point with either positive or negative slope we obtain setpoints for the laser diode temperature $T_{\text{LD}}^{\text{set}}$ and the DC voltage $V_{\text{DC}}^{\text{set}}$ and can calculate the displacement to voltage conversion factor given in equation (2.13) by inserting $V_{\min}$ and $V_{\max}$. During experiments it is crucial that these setpoints are met throughout the whole measurement run. This can be achieved by locking onto the fringe setpoint $V_{\text{DC}}^{\text{set}}$ with the digital laser controller giving feedback on the diode temperature or the diode current. With the former long term drifts are eliminated and the latter can cancel fluctuations up to a bandwidth of about 1 kHz. In practice we observe that at LHe temperature the cavity is stable enough to work without any feedback and the laser diode temperature is simply stabilized at $T_{\text{LD}}^{\text{set}}$.

Another quantity that can be extracted from the fringe pattern in Figure 2.6 is the free spectral range (FSR) of the cavity corresponding to the period of the oscillation.

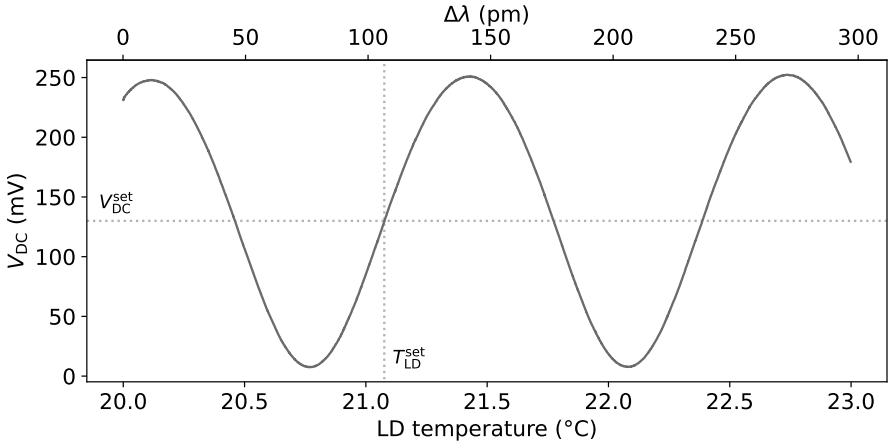

Figure 2.6. – **Fringe signal vs. laser diode temperature**
Interference fringes obtained if the laser wavelength is tuned by varying the laser diode temperature. The setpoints for optimal operation are marked by dashed lines. One fringe period corresponds to the free spectral range (FSR) of the cavity.

A quick fit reveals FSR = 129.63(3) pm and allows us to calculate the cavity length by $l_{\mathrm{cav}} = \lambda^2/[2n_{\mathrm{vac}}\mathrm{FSR}] \approx 9.27\,\mathrm{mm}$. There are some implications regarding the coherence length of the laser which is given by $L_{\mathrm{coh}} = c_l/[\pi\Delta\nu_{\mathrm{las}}]$, where c_l is the speed of light and $\Delta\nu_{\mathrm{las}}$ the linewidth of the laser[29]. Using the largest linewidth specified for our laser head we retrieve $L_{\mathrm{coh}} \approx 23.9\,\mathrm{m}$ which is orders of magnitude bigger than the cavity length and can lead to unwanted signals from other cavities present in the optical path. In order to minimize these effects we modulate current at the laser diode directly with a small amplitude modulation at a frequency $\geq 10\,\mathrm{MHz}$ effectively decreasing the coherence length. Additionally all fiber connectors used are of the FC/APC type to minimize spurious reflections as already mentioned previously.

The displacement to voltage conversion factor was derived in equation (2.13) for the special case where the NW is centered with respect to the optical axis. We can extend the definition of the optical gradient to the xy-plane by [21]

$$\|\nabla V_{\mathrm{DC}}(x_0, y_0)\|\hat{\mathbf{e}}_\beta, \quad \hat{\mathbf{e}}_\beta = \frac{\nabla V_{\mathrm{DC}}(x_0, y_0)}{\|\nabla V_{\mathrm{DC}}(x_0, y_0)\|} \tag{2.14}$$

with the working points (x_0, y_0) and the direction of the local optical gradient $\hat{\mathbf{e}}_\beta$. This quantity describes the absolute value of the displacement to voltage conversion and its direction in the xy-plane. Moving the NW to different working points we can measure its 2D-motion projected onto different directions β. Noting again that the NW motion is very small compared to $\lambda/4$ we can locally probe the optical gradient by offsetting the NW by small amounts $x_0 \pm \delta x_0$, $y_0 \pm \delta y_0$ and fitting the resulting values of V_{DC} to a second order polynomial in x and y. This can than be used to determine the

[29] DFB pro $\Delta\nu_{\mathrm{las}} = 1$ to 4 MHz

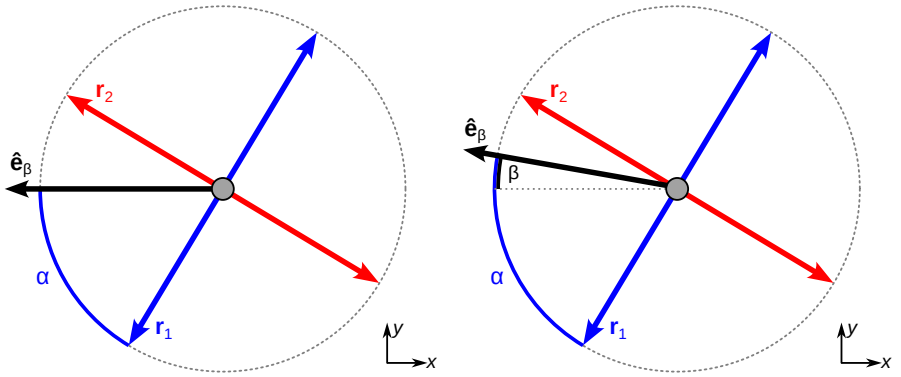

Figure 2.7. – **Measurement vector**
Illustration of the measurement vector for two cases. On the left hand side the NW is positioned centered with respect to the focal spot and on the right hand side it is offset to one side. α is the mode angle with respect to the measurement vector and β the angle between the optical axis and the measurement vector. The blue arrows indicate the motion direction of the lower NW mode in frequency and the red arrows the upper frequency mode.

local magnitude of the optical gradient and its direction with respect to the optical axis during measurements without having to obtain a full range cavity scan. However, this method is limited by drifts of the piezo positioners and the necessity to know their precise displacement calibration. For most measurements we work on the optical axis ($\partial V_{\mathrm{DC}}/\partial y = 0$) at the point of highest sensitivity and rely on a simple temperature scan shown in Figure 2.6 to extract the magnitude of the optical gradient, assuming that $\hat{\mathrm{e}}_\beta$ is aligned with the optical axis (x-axis).

In Figure 2.7 the direction of the measurement vector is illustrated for two different cases: Aligned along the optical axis and tilted away by 10°. It is important to distinguish the angle α from the measurement angle β here. We denote with α the angle of the lower frequency mode direction with respect to the measurement vector. If the NW is positioned centered within the focal spot $\beta = 0°$ and α is the angle between the optical axis (x-axis) and the lower frequency mode. In general however the measurement angle can deviate from 0° and the angle of the lower frequency mode with the x-axis is given by $\alpha' = \alpha - \beta$, which is important for identifying the mode directions with respect to the sample. Additionally we should emphasize that α is ambiguous with regard of its sign. Since we only measure along a single measurement vector, two possible solutions exist for the projection of the in-plane NW motion onto $\hat{\mathrm{e}}_\beta$. This ambiguity can be lifted by measuring subsequently at a different measurement vector and requires to move the NW to a different spot, which can be very inconvenient during scans, since it necessitates moving NW and sample in sync. Detection schemes in transmission using a split photodiode allow for simultaneous measurements along two orthogonal measurement vectors [46, 48] by using sum and difference signal. In any case the mode

direction with respect to the sample usually emerges from the fact that each mode is the most sensitive to force gradients along its oscillation direction, highlighting the orientations directly in the recorded image.

2.3. Actuation

Driving the NW at its resonance frequency for the dynamical readout can be achieved in a number of ways and requires either accoustic actuators or relies on field gradients. Historically AFM probes are driven piezoelectrically by placing a dither piezo in the vicinity of the cantilever. Other methods include accoustic [134] (in liquid), optical [126] or capacitive techniques [13]. In the following section we will explore three methods used in our setup by estimating their transfer functions under the assumption of linear time-invariant systems. In the frequency domain the linear response function of a damped harmonic oscillator (see Section 1.2.1) is given by

$$\chi_{\mathrm{ho}}(\omega) = \frac{\hat{r}(\omega)}{\hat{F}(\omega)} = \frac{1}{M[\omega_0^2 - \omega^2] + i\Gamma\omega}. \tag{2.15}$$

In a real experiment we have to consider the transfer function of the full system. The driving signals amplitude and phase are modified additionally on the path from signal generation at the lock-in amplifier to the NW, depending on the driving method. On the detection side, which is the same for all three actuation techniques, there is in general an additional phase offset present and the amplitude gain function is characterized by equation (2.13). We can write

$$H_{\mathrm{total}}(\omega) = H_{\mathrm{det}}(\omega)\chi_{\mathrm{ho}}(\omega)H_{\mathrm{drive}}(\omega) \tag{2.16}$$

where each of the transfer functions can be expressed in the form $|H(\omega)|e^{i \arg H(\omega)}$. In the frequency domain gains are multiplicative and phases add up. In practice it is very challenging to characterize all the gain functions properly. Here we will assume that $H_{\mathrm{det}}(\omega)$ has a flat frequency spectrum. Its fixed amplitude and phase offset can be absorbed into $H_{\mathrm{drive}}(\omega)$, leaving us with

$$H_{\mathrm{total}}(\omega) = \chi_{\mathrm{ho}}(\omega)H_{\mathrm{drive}}(\omega). \tag{2.17}$$

Inferring the harmonic oscillator susceptibility from the mechanical properties as fitted from a thermal noise PSD measurement of the NW, we can estimate $H_{\mathrm{drive}}(\omega)$ by

$$H_{\mathrm{drive}}(\omega) = \frac{H_{\mathrm{total}}(\omega)}{\chi_{\mathrm{ho}}(\omega)}. \tag{2.18}$$

The accessible frequency range is limited to a region around the NW resonances, where the contribution of $\chi_{\mathrm{ho}}(\omega)$ is not below the noise level of the electronics. Additionally the relative amplitude can only be fixed to an arbitrary value.

Figure 2.8 shows the transfer functions for three different actuation methods for comparison. In order to estimate the transfer functions in each case the frequency was

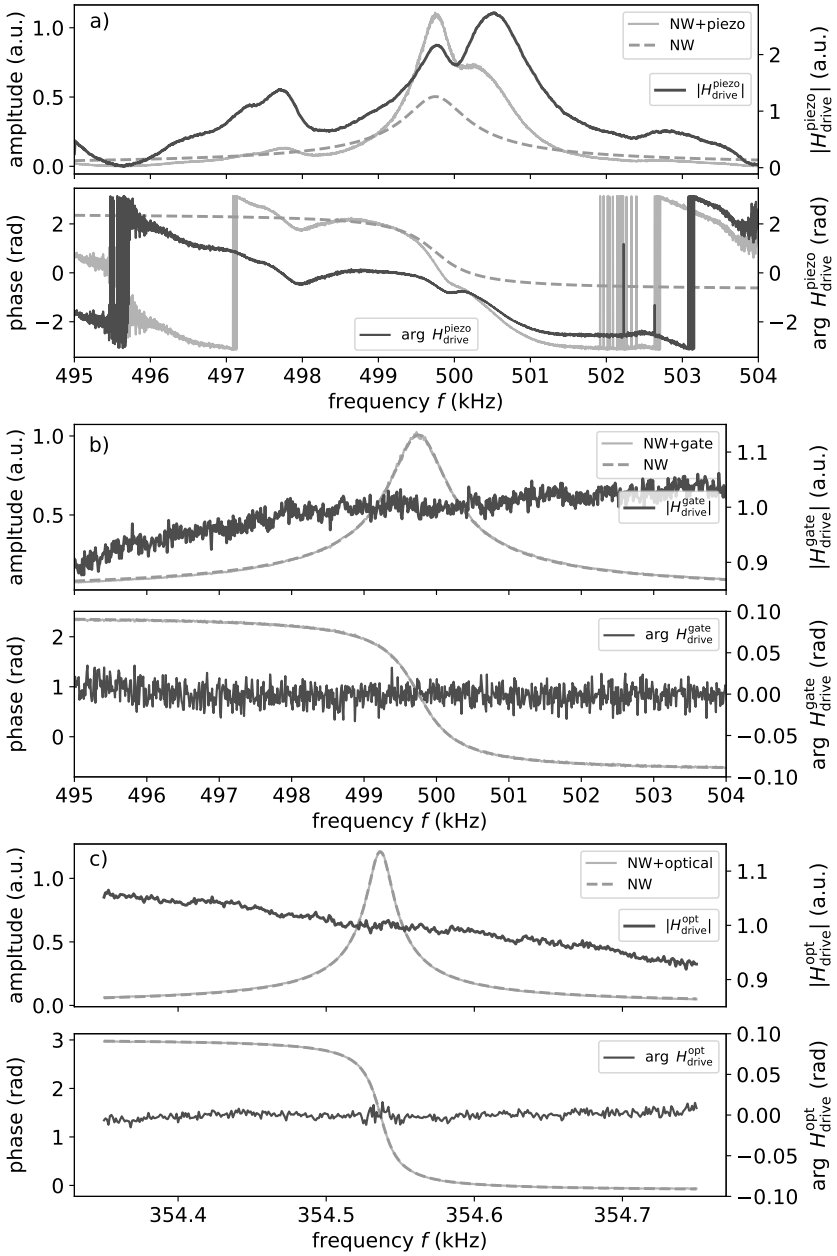

Figure 2.8. – **Actuation methods**
(a) Amplitude and phase acquired with frequency sweeps for three different methods of actuation: (a) piezoelectric, (b) capacitive and (c) optical (using a different NW with a higher quality factor than in (a) and (b)). The gray lines represent the data, dashed gray the inferred mechanical susceptibility of the NW and the dark gray the estimated respective transfer functions. Capacitive and optical drive offer an almost flat frequency response in phase and amplitude as compared to the piezoelectric drive.

swept across one of the NW resonances, recording amplitude and phase of the response. Figure 2.8a displays the result in case of piezo-driven actuation. The amplitude and phase response are rugged around the NW resonance and show large variations within its linewidth. This response can lead to artifacts in frequency shift and amplitude signals during imaging and is attributed to spurious resonances of the entire mechanical assembly, including the dither piezo and its coupling to the environment itself. Usually these type of spurious behavior is becoming more pronounced at cryogenic temperatures. It is known in AFM literature [104, 105] and Labuda et al. derived a complete framework to calibrate a given AFM system. It requires the use of a "clean" drive - in AFM usually an AC variation on the tip-sample bias - and can empirically correct for the apparent dissipation effect. In our experiments frequency shifts are on the order of a few to many linewidths of the NW resonators, due to their small spring constants. Calibrating the full spectral range needed for imaging would require to tune the NW resonance at will, without affecting its free properties. Having no control of the tip-sample bias we are not able to achieve this prerequisite. Additionally, even within the small range of shifts accessible by tuning a gate voltage on a sample it turns out that the spurious resonances seem to be non-linear in nature and couple differently to the NW resonances, depending on their center position or even drifting over time due to small fluctuations of the experimental conditions.

NWs with a low quality factor are especially prone to these type of effects, since their broad linewidths allow for multiple spurious resonances to convolute with the NWs susceptibility and produce the spectrum shown in Figure 2.8a. For stiffer NWs with larger quality factors one might assume a locally flat transfer function. However as soon as tip-sample forces become large and the NW resonance shifts by multiple linewidths this assumption breaks down. Of major concern is also the non-monotonic phase response. When setting up a phase-locked loop (PLL) on a fixed phase, multiple points exist in the spectrum where the phase set point is met. The result are instabilities obscuring acquired images, which are almost impossible to correct for. Finally the dynamic range of the amplitude controller needs to cover a few orders of magnitude, e.g. when the NW resonance is on top of a point with high damping in the transfer function.

The second option of using an oscillating gate voltage to drive the NWs motion exhibits an almost flat transfer function $H^{\text{gate}}_{\text{drive}}(\omega)$ in amplitude and phase as can be seen in Figure 2.8b. Both parts seem to deviate on the lower end of frequencies which can be attributed to the presence of the second resonance, since the mode splitting is small. In general the transfer function fulfills the requirement of a flat phase across multiple linewidths of the NW resonance and is suitable for establishing a PLL. However there are a few disadvantages of employing a capacitive drive for imaging. First, they require the patterning of a finger gate in close proximity to the sample of interest. Depending on the exact sample geometry and fabrication process this poses a significant challenge, especially with the constraint in mind the sample to be placed close at the chip edge. Second, the local AC field driving the NW is spatially not homogeneous. It can change vastly within the scan range of a single image. With the NW tip being in an undefined but usually stable charge state, it acts as a local probe of the AC field at its resonance. Mapping the amplitude generally results an a spatial gradient towards the gate source.

Closer to the sample this variations become smaller in spatial wavelength. Utilizing a suitable amplitude controller with a wide enough dynamic range can compensate for the inhomogeneities. The phase is similarly changing and has shows strong dependence on position. If the gradient of the driving field switches sign with respect to the oscillation direction of the NW the phase set point of the PLL flips by π and it becomes impossible to track the resonance frequency across such a phase flip, also derailing the amplitude controller. Consecutive images with phase set points separated by π can be added up to a composite image. However there will always be missing information at the boundary points. In summary the capacitive driving method can be locally very powerful, if the gate electrode is designed in a way to produce a very homogeneous field within the vicinity of the sample of interest. Practically this is hard to achieve and local deviations will always be present.

2.3.1. Optical drive

The third method of actuation is optical excitation via the intensity modulation of a second laser beam with a wavelength of 1625 nm, spectrally separated from the readout laser. One consequence is a slight focal shift with respect to the working point x_0, leading to a wider beam diameter of the excitation laser at the position of the NW. The transfer function also exhibits very flat amplitude and phase contributions as can be seen in Figure 2.8c. In comparison to the capacitive actuation method the optical drive works universally and has no spatial dependence, except when scanning too far inwards from the chip edge, cutting off the driving and readout lasers intensity.

Photothermal actuation has widely been used in AFM [135–139] especially in the liquid phase. Two driving forces of different origin are considered: photohermal and/or radiation pressure mediated. Vassalli et al. separate them by their different contributions for coated and uncoated cantilevers with respect to the position of the exciting laser along the cantilever [140]. The photothermal driving force shows a maximum at the 2nd derivative of the mode shape, close to the base point, whereas the radiation pressure force follows the mode shape of the first order flexural mode. Photothermal excitation dominates for coated cantilevers while equal contributions arise in for uncoated ones. Gil-Santos et al. [124] examine the effects of bolometric heating and radiation pressure based effects and show that they can exhibit a rich behavior depending on the NW diameter. If certain Mie scattering conditions are met, absorption is high leading to a frequency offset due to the temperature dependence of the Young's modulus. Similarly the resonance frequency can be shifted by the presence of a radiation pressure gradient, which is also enhanced when a Mie resonance condition is fulfilled. However their experimental design has the NW horizontally suspended above the substrate and excitation and detection from the top lead to cavity effects due to the high reflectivity of the substrate. Additionally the incident power used in their work (100 µW, $\lambda = 635$ nm) is one order of magnitude higher than in our experiments and Mie resonances are more pronounced at smaller wavelength.

In our optical drive we observe that both NW modes are driven equally if the same AOM modulation amplitudes (see below) are applied. This means there is no direc-

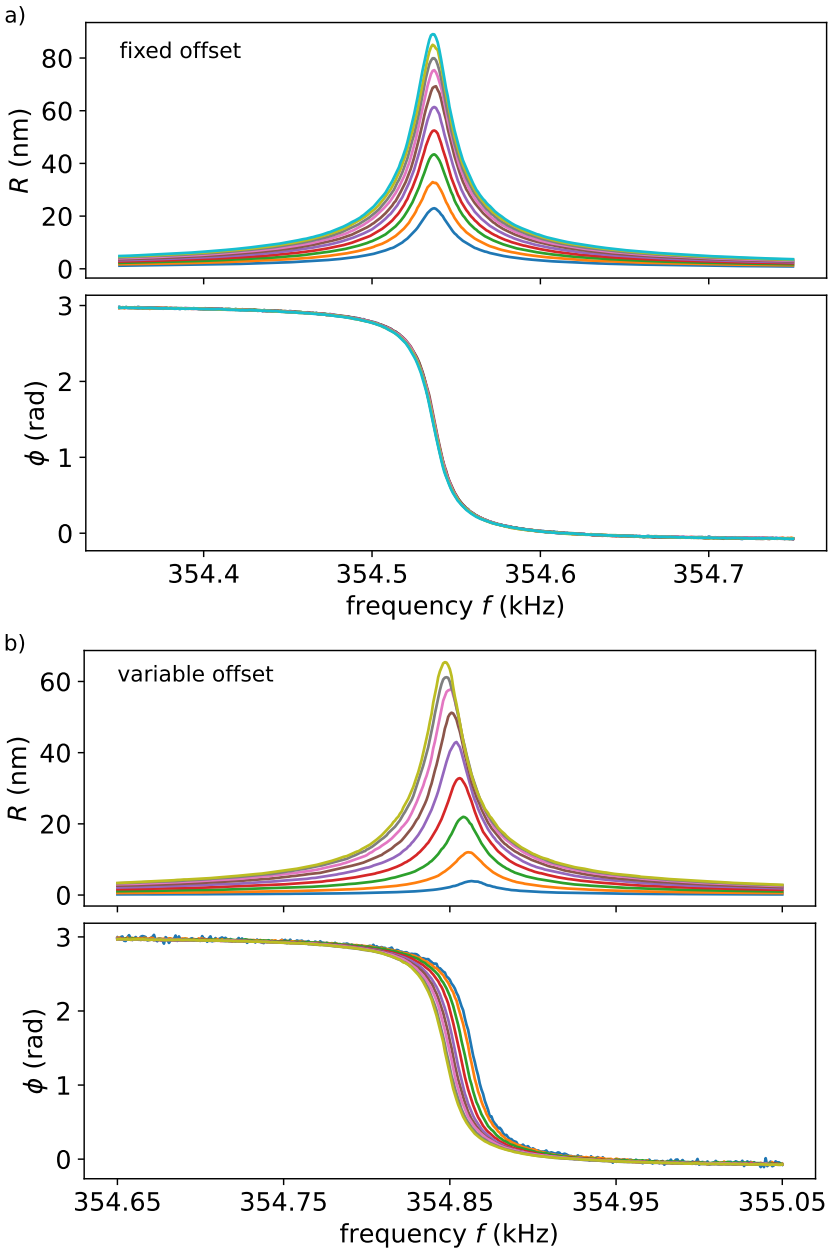

Figure 2.9. – **Optical drive: Sweeps**
Sweeps of a Si NW resonance with different AOM modulation amplitudes. (a) The driving amplitude is varied around a fixed offset of 400 mV with modulation amplitudes ranging from 76 to 400 mV. (b) The offset is variable and equals the modulation amplitude ranging from 100 to 500 mV. In case of fixed offset the average incident power on the NW stays the same, while with a variable offset it increases with the modulation amplitude leading to a heating effect mediated through the temperature dependence of the Young's modulus.

tionality with respect to optical gradients. From the data in Figure 2.9b it is evident that we bolometrically heat the NW with the driving laser and can conclude that the main driving mechanism in our setup is photothermal. This is further reinforced by the observation that mode hopping of the driving laser affects both modes simultaneously showing a jump in frequency shift.

The optical drive is implemented using an AOM[30] with the corresponding driver unit[31] and a high stability laser diode[32] emitting at 1625 nm with a built in optical isolator. In front of the AOM a second 3-paddle polarizer[33] is installed in order to adjust the polarization of the driving laser to be aligned with the NW-axis. A few characteristics of the AOM are shown in the Appendix Figures A.2 (output power vs. modulation depth) and A.3 (output power vs. operating frequency). The performance of the optical drive was assessed by sweeping across one resonance of a Si NW at 4 K. We differentiate between two modes of operation. The AOM modulation signal is given in its general form by

$$A_i(t) = A_0^{\mathrm{AOM}} + A_i^{\mathrm{AOM}} \sin(2\pi f_i t + \phi_{0,i}^{\mathrm{AOM}}) \tag{2.19}$$

ranging from 0 to 1 V. $A_{0,i}^{\mathrm{AOM}}$ is the modulation offset, A_i^{AOM} the modulation amplitude and the index i indicates the NW mode. In the first operation mode the modulation offset is kept at a fixed value of $A_0^{\mathrm{AOM}} = 400\,\mathrm{mV}$ and A_i^{AOM} is varied. This leads to an illumination of the NW with constant power and the intensity is modulated around this offset. Figure 2.9a shows the corresponding resonance curves for different modulation amplitudes and the resonance properties of the NW are summarized in Figure 2.10a. Up to a modulation amplitude of 250 mV the resonance frequency f_0 does not show any significant change. Above however it decreases slightly pointing to the onset of non-linear behavior. The oscillation amplitude R_0 increases directly proportional to the output power of the AOM. At first the increase is linear and at modulation amplitudes higher than 200 mV it becomes sublinear with the reason being the characteristic input/output curve of the AOM device (see Figure A.2).

The second mode of of operation varies the modulation offset in a way that $A_0^{\mathrm{AOM}} = A_i^{\mathrm{AOM}}$ leading to a modulation of the incident light from zero intensity up to a maximum power and not around a constant offset. Figure 2.9b shows the corresponding frequency sweeps and Figure 2.10b the resonance properties of the NW. Here a clear dependence of f_0 on the modulation amplitude is visible. The decrease is easily explained by heating due to the higher incident power as the Young's modulus changes with the NW temperature. The oscillation amplitude R_0 follows the same pattern as in the first mode of operation, directly linked to the input/output characteristics of the AOM.

For our measurements we chose operating the AOM with a fixed offset. This has the effect of constantly illuminating the NW with more power, leading to a slight downshift of f_0, but has the advantage of a constant f_0 if locking the oscillation amplitude becomes necessary. In any case we usually work with oscillation amplitudes smaller than 20 nm,

[30] EQ Photonics SFO6123-T-M110-0.2C2J-3-F2S
[31] AODR 1110AFP-AD-3.0
[32] AeroDIODE 1625LD-1-0-0 Model 1 (10 mW) DFB
[33] Thorlabs FPC560

well below the point where the anharmonic effects set in (Figure 2.10a). Typical optical powers of the driving laser incident on the NW are between 5 to 30 µW.

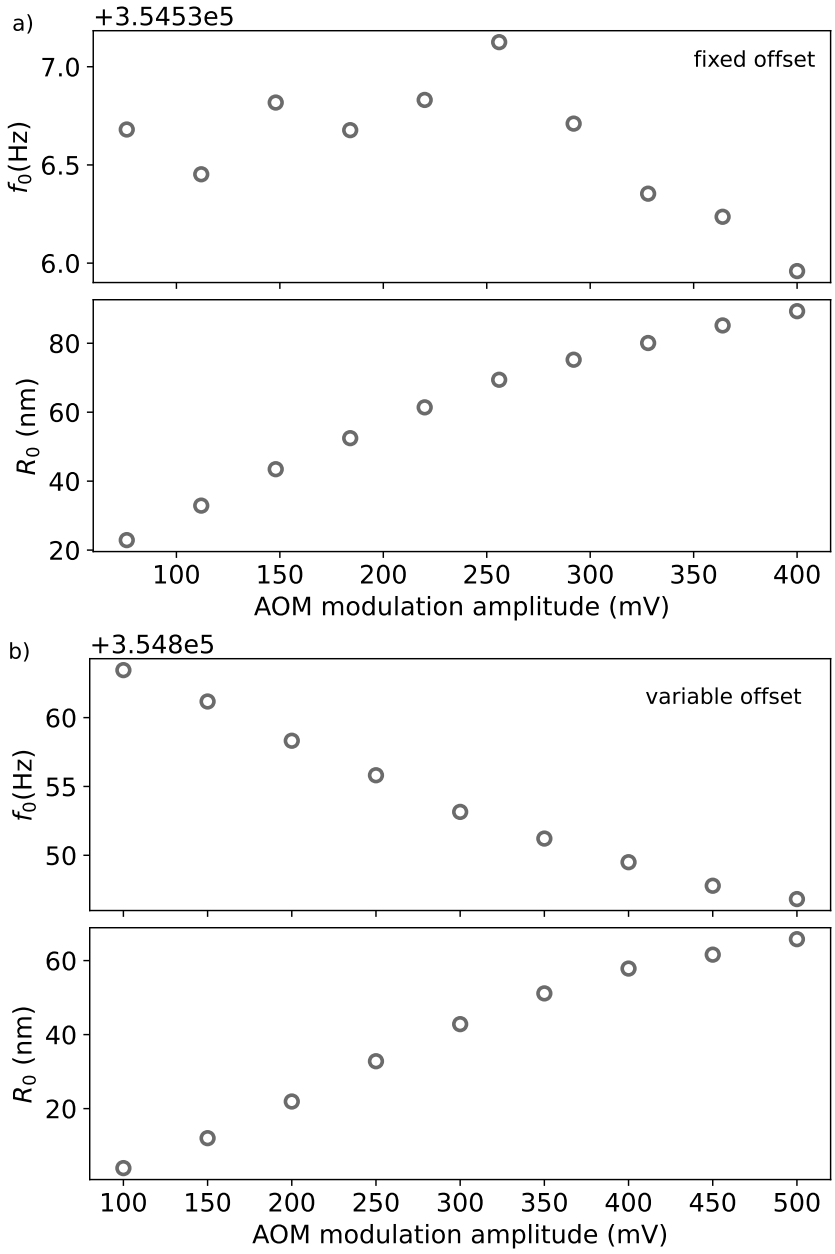

Figure 2.10. – **Optical drive: NW resonance**
Frequency shift and oscillation amplitude at resonance for different AOM modulation amplitudes. The properties are derived from fitting the data in Figure 2.9 to a harmonic oscillator lines shape. (a) In case of the fixed offset at 400 mV the resonance frequency is very stable up to an AOM modulation amplitude of 250 mV after which it decreases slightly. This might be attributed to the onset of non-linearity. (b) The resonance frequency curve in the case of an offset equal to the modulation amplitude confirms the heating effect by the temperature dependence of the Young's modulus. In both cases the oscillation amplitude R_0 increases directly proportional to the output power of the AOM (see Figure A.2).

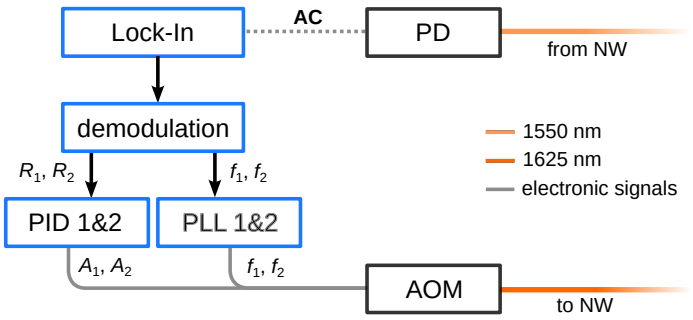

Figure 2.11. – Signal acquisition and phase and amplitude locking
Schematic sketch of the signal acquisition during imaging. Frequencies and amplitudes of both NW modes are locked using PLL/PID feedback loops on the AOM driver.

2.4. Image acquisition

After approaching with the sample of interest towards the NW probe we set up the image acquisition in the following way: A block diagram showing the relevant elements is displayed in Figure 2.11. During the approach the laser is positioned roughly in the middle of the nanowire, balancing a higher signal amplitude (due to the mode shape of the NW mode which is bigger towards the tip) against cutting off the laser intensity with the chip edge of the bottom sample. Frequency sweeps reveal the NW resonances and the corresponding phase and amplitude set points. The two resonance frequencies f_1 and f_2 are locked with PLLs. The PLL bandwidth is usually chosen to be around the linewidth of the NW resonance or a bit broader for narrow resonances in order to enable reasonable scanning speeds. For most measurements it will be around 25 to 50 Hz.

The amplitude is adjusted by changing the AOM modulation amplitudes so that both modes are driven equally. Here the mode shape and the projection of the modes onto the measurement vector have to be taken into account properly. The resulting driving signal contains both frequencies and amplitudes is fed to the AOM driver and imprinted onto the driving laser. Usually we work with fixed open loop driving amplitudes, since the PIDs for amplitude locking require very small bandwidths, leading to time consuming scans. Typical scanning speeds are around $0.25\,\mu\mathrm{m\,s^{-1}}$, depending on the desired spatial resolution.

The scanning height is adjusted by a procedure we call “soft touchpoint calibration”. As we approach the bottom sample carefully towards the NW tip we monitor frequencies and oscillation amplitude. At very close distances strong forces lead to massive frequency shifts and damping of the oscillation amplitudes. By simultaneously monitoring the thermal noise spectrum we stop the slow approach when the resonances are almost damped to the noise level. The extension of the bottom z-scanner at this point is marked as z_{touch}. Retracting from this point we use the piezo voltage to distance calibration given by the manufacturer to determine the scanning height. This procedure

introduces an estimated error of about ±10 nm since it highly depends on the local nature of the surface on which we execute the touch point and is subject to the tolerance of the manufacturers specifications. As compared to standard AFM/MFM operating modes we work with a fixed scanning height and do not employ active distance control. Typical scanning heights range from 50 to 250 nm, mainly because the minimum spatial resolution is defined by the tip diameter and a larger tip-sample distance allows for better a disentanglement of topographic and magnetic signals.

Once all of the above is set up we employ a LabView VI to handle the scan control. The selected scanning window can be either rastererd line-by-line or point-by-point. Respecting the PLL/PID time constants the scan speed is adjusted to allow for a clean image capture without artifacts. During the scan frequency shifts and oscillation amplitudes and/or their PLL/PID error signals are recorded from the lock-in amplifier and saved to disk.

3. Probes for Nanowire Magnetic Force Microscopy

In this chapter we will discuss two types of NW-MFM probes recently employed in our setup. The first are fully magnetic NWs grown by Co focused electron beam induced deposition (FEBID) and the second are extremely high quality Si NWs functionalized with a Co FEBID tip.

3.1. Cobalt FEBID nanowires

This section is entirely based on the published article *Nanowire magnetic force sensors fabricated by focused-electron-beam-induced deposition* [13]. The free standing Co FEBID NWs were fabricated by J. M. de Teresa[1] and the permalloy disks by the Berezovsky group[2].

3.1.1. Motivation

In the early 1800s, images of the stray magnetic fields around permanent magnets and current-carrying wires made with tiny iron filings played a crucial role in the development of the theory of electromagnetism. Today, magnetic imaging techniques such as Lorentz microscopy, electron holography, and a number of scanning probe microscopies continue to provide invaluable insights. Images of magnetic skyrmion configurations [141] or of edge and surface currents in topological insulators [142] have provided crucial direct evidence for these phenomena. The ability to map magnetic field sensitively and on the nanometer-scale – unlike global magnetization or transport measurements – overcomes ensemble or spatial inhomogeneity in systems ranging from arrays of nanometer-scale magnets, to superconducting thin films, to strongly correlated states in van der Waals heterostructures. Local imaging of nanometer-scale magnetization [143], local Meissner currents [144], or current in edge-states [145] is the key to unraveling the microscopic mechanisms behind a wealth of new and poorly understood condensed matter phenomena.

The techniques combining the highest magnetic field sensitivity with the highest spatial resolution include scanning Hall-bar microscopy, scanning nitrogen-vacancy (NV) center magnetometry, and scanning superconducting quantum interference device (SQUID) microscopy. Each has demonstrated a spatial resolution better than 100 nm and a magnetic field sensitivity ranging from $500\,\mu\mathrm{T}/\sqrt{\mathrm{Hz}}$ for Hall-bar microscopy [146], to

[1] INMA and Universidad de Zaragoza, Zaragoza, Spain
[2] Case Western Reserve University, Cleveland, Ohio, USA

$60\,\mathrm{nT}/\sqrt{\mathrm{Hz}}$ for NV magnetometry [147], and $5\,\mathrm{nT}/\sqrt{\mathrm{Hz}}$ for scanning SQUID microscopy [14]. Recently, a form of magnetic force microscopy (MFM) based on a transducer made from a magnet-tipped nanowire (NW) demonstrated a high sensitivity to magnetic field gradients of $11\,\mathrm{mT}/(\mathrm{m}\sqrt{\mathrm{Hz}})$ with a similar spatial resolution [12]. The high force sensitivity of NW cantilevers coupled together with a small magnetic tip size could allow such sensors to work both close to a sample, maximizing spatial resolution, and in a regime of weak interaction, remaining noninvasive.

Here, we demonstrate the use of individual magnetic NWs, patterned by focused electron beam induced deposition (FEBID), as MFM transducers for mapping magnetic fields with high sensitivity and resolution. The monopole-like magnetic charge distribution of their tips makes these transducers directly sensitive to magnetic fields rather than to field gradient, as in the initial demonstration of NW MFM [12]. Furthermore, the FEBID fabrication process allows for a large degree of flexibility in terms of the geometry, composition, and location of the NW transducers. In particular, the possibility of long, thin, and sharp NWs is promising for further increasing field sensitivity and spatial resolution of the technique [52].

3.1.2. FEBID as fabrication technique for free-standing NWs

FEBID is an additive-lithography technique where precursor gas molecules are adsorbed onto a surface and dissociated by a focused electron beam, forming a local deposit [148–152]. It can be used to pattern exceptionally small features, down to a few nanometers. This high resolution patterning is complemented by the capability to produce three-dimensional structures, as well as to pattern on unconventional non-planar surfaces, such as high-aspect-ratio tips. FEBID and its sister technique, focused ion beam induced deposition (FIBID), have been used to produce deposits of various materials with metallic [153], magnetic [154, 155], superconducting [156], or photonic [157] functionalities. They have been used in industry and research for mask repair [158], circuit editing, lamella fabrication [159], tip functionalization [160], and for the fabrication of nano-sensors [161]. They have also been employed in the production of free-standing NWs from both superconducting [162] and – as in this work – magnetic materials [155, 163].

We grow free-standing NWs by FEBID using $Co_2(CO)_8$ as a gas precursor at specific positions along the cleaved edge of a Au-coated GaAs chip. Their lengths range from 9.1 µm to 11.0 µm and their base diameters from 105 nm to 120 nm as inferred from scanning electron microscopy (SEM) images. In general, NWs with diameters ranging from 35 nm to 1 um can be grown using our FEBID technique. The NWs studied here consist of nanocrystalline Co, with a composition reaching up to 80% [163], and residues of C and O. Their proximity to the edge of the chip allows optical access from the side for the detection of their flexural motion. A SEM image of a Co NW standing at the chip edge is shown in Figure 3.1a. Surface roughness and geometric irregularities are part of the FEBID fabrication process and are present across the 11 NWs studied in this work.

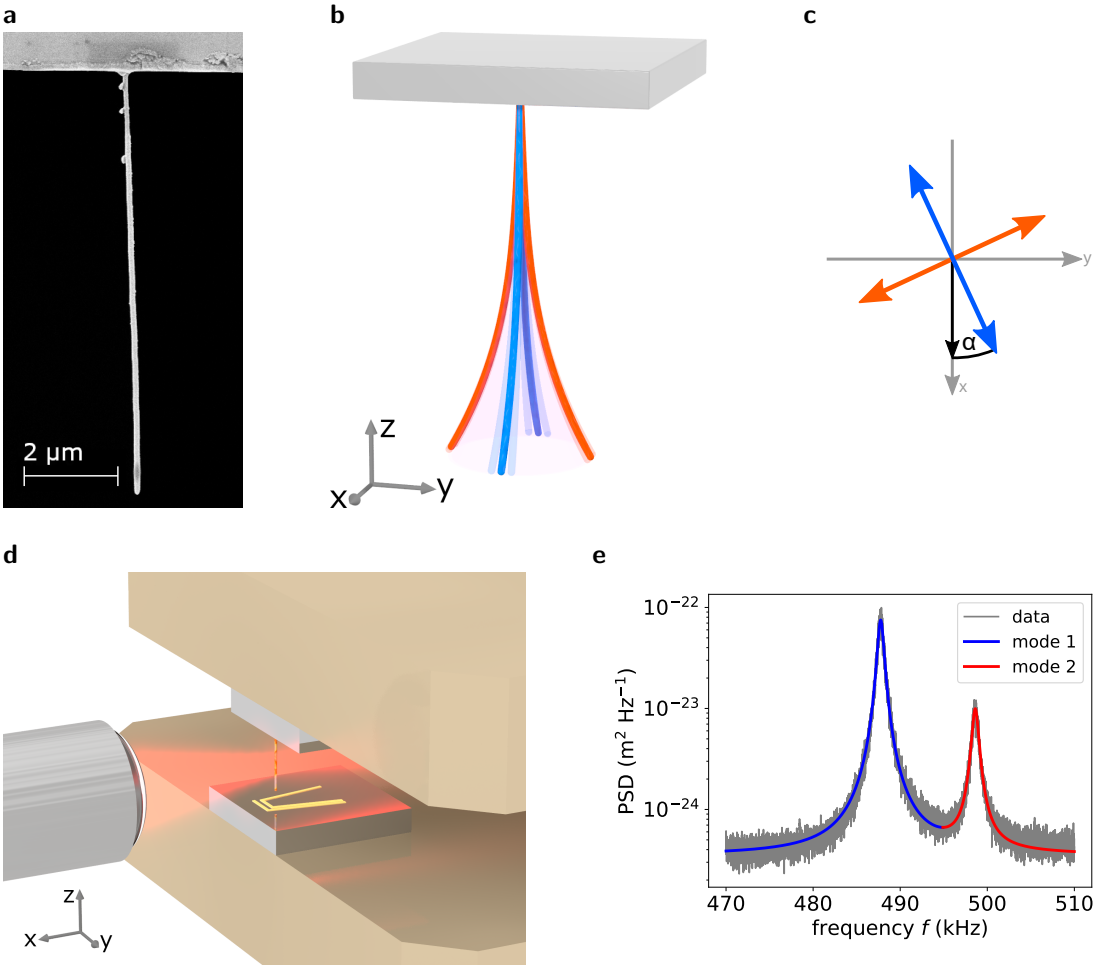

Figure 3.1. – **Co FEBID nanowires**
a) SEM micrograph of a Co FEBID NW at the chip edge. **b**) Illustration of the NW's flexural modes. The displacement amplitudes are exaggerated for better visibility. **c**) Projection of flexural modes onto the xy-plane. α is the angle between the lower frequency mode direction (blue) and the measurement vector (black). **d**) Illustration of the optical readout of the NW motion. **e**) Thermally excited response of the upper and lower mode at room temperature (gray). We fit the thermal noise displacement PSD with equation (1.90). The two modes are highlighted by the blue and red regions of the fit.

3.1.3. Mechanical and magnetic properties

Mechanical properties

Measurements of the NWs' thermo-mechanical noise PSD are performed with the bath held at room temperature (293 K), liquid nitrogen temperature (77 K), and liquid helium temperature (4.2 K). Heating caused by absorption of the incident laser light (typically 25 µW) can increase the NW's temperature well above the bath temperature. As a result, care must be taken interpreting PSDs, as discussed in Section 3.1.6. Using the fits to the measured PSDs based on the fluctuation-dissipation theorem, we determine the mechanical properties of the fundamental flexural modes: their resonance frequencies $f_i = \omega_i/2\pi$, quality factors Q_i ($i = 1, 2$), and effective motional mass m_{eff} (see Section 2.2) [12]. At 293 K, the resonance frequencies of the NWs are between 390 kHz and 560 kHz with a mode splitting from 10 kHz to 42 kHz. We measure quality factors around 600 and motional masses in the 100s of fg range. These parameters correspond to flexural modes with effective spring constants k_i of a few mN/m. At a bath temperature $T_{\text{bath}} = 4.2$ K, the quality factors improve by roughly a factor of 3 to around 1000 to 2000 and the resonance frequencies shift upwards by roughly 30 kHz. From these parameters, shown in Table 3.1 for two different NWs, we deduce the spring constants, mechanical dissipation, and thermally limited force sensitivities. Notably, at $T_{\text{NW}} = 4.2$ K, a typical NW has flexural modes with thermally-limited force sensitivities around $10\,\text{aN}/\sqrt{\text{Hz}}$. In practice the force sensitivity is limited to about $25\,\text{aN}/\sqrt{\text{Hz}}$, since even at very low laser power (1 µW on NW 4, signal-to-noise ratio of first mode SNR ≈ 8) bolometric heating is present and leads to a NW temperature $T_{\text{NW}} \approx 20$ K (see Section 3.1.6).

Magnetic properties

We probe the magnetic properties of each NW by measuring its mechanical response to a uniform magnetic field B up to 8 T applied along its long axis. In particular, we measure the shift in the resonance frequency of each flexural mode, $\Delta f_i = f_i - f_{0_i}$, as a function of B, where f_{0_i} is the resonance frequency at $B = 0$. Figure 3.2 shows a typical measurement of the hysteretic response of $\Delta f_1(B)$ and $\Delta f_2(B)$ carried out on NW 4 with $T_{\text{bath}} = 4.2$ K. As in measurements of the other NWs, the data show a smooth V-shaped response for most of the field range, except for discontinuous inversions of the slope ("jumps") in reverse fields of around ±40 mT. These sharp features, which arise from the switching of the NW magnetization, and the steady stiffening of the mechanical response as $|B|$ increases are characteristic of a strong magnet with a square magnetization hysteresis, whose easy axis is nearly parallel to the applied field [164], as opposed to a weak magnet with comparatively small switching field and saturation magnetization. Therefore, the data point to NWs with negligible magnetocrystalline anisotropy and an easy axis coincident with their long axis, as set by the magnetic shape anisotropy resulting from their extreme aspect ratio.

In order to extract specific magnetic properties from our measurements, we compare them to micromagnetic simulations, which model both the NW's magnetic state and the way in which its interaction with B affects the mechanical rigidity of the flexural

Table 3.1. – Mechanical properties of Co FEBID NWs
Mechanical properties of representative NWs with the thermal bath held at room temperature ($T_{\mathrm{bath}} = 293\,\mathrm{K}$) and liquid helium temperature ($T_{\mathrm{bath}} = 4.2\,\mathrm{K}$) measured at high and low laser powers. Resonance frequencies, Q-factors, effective mass, and measurement angle (not shown here) are extracted by fitting the thermal noise PSD (see Section 1.2.4). For a correct interpretation, bolometric heating due to the readout laser must be taken into account. Considering this effect, we also specify a NW temperature T_{NW} (see Section 3.1.6). The data of the last two lines in a liquid helium environment correspond to NW temperatures of 99 K (20 µW) and 22 K (1.2 µW) respectively.

T_{bath}	NW	f_1 (kHz)	f_2 (kHz)	Δf_{m} (kHz)	Q_1	Q_2	M (10^{-15} kg)
293	1	390.726	426.018	35.292	528.0(1.4)	–	0.69(4)
	4	514.459	556.750	42.291	551.1(1.5)	527(66)	0.260(15)
4.2	4	550.803	593.745	42.942	1045(1.0)	1156(40)	0.260(15)
	4	555.860	599.044(49)	43.18	2356(39)	–	0.260(15)

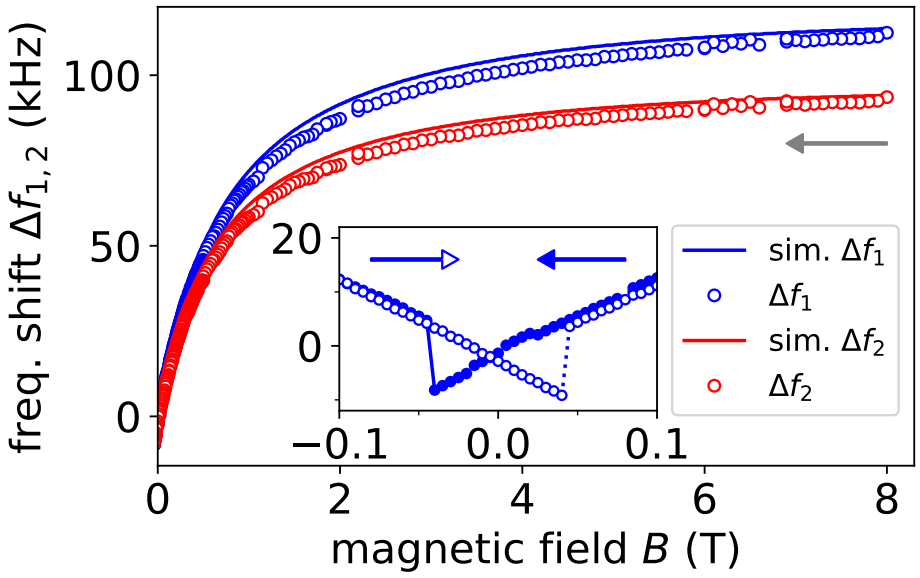

Figure 3.2. – **Magnetometry of Co FEBID NWs**
Resonance frequency shift of the two first order flexural modes of NW 4, measured while sweeping an axially aligned external magnetic field from 8 T to 0 T (gray arrow). Points represent measured data, while solid lines correspond to simulations using *Mumax3* (see Section 3.1.3), yielding a saturation magnetization of $M_{\mathrm{sat}} = 1.1(1) \times 10^6\,\mathrm{A\,m^{-1}}$ which equates to $\mu_0 M_{\mathrm{sat}} = 1.43(12)\,\mathrm{T}$. The inset shows a close-up plot of mode 1's frequency shift in the switching region around zero field for down- and up-sweep of the field (blue arrows). The jumps are highlighted by solid and dashed blue lines.

modes. We use *Mumax3* [165, 166], which employs the Landau-Lifshitz-Gilbert micromagnetic formalism with finite-difference discretization, together with geometrical and material parameters to model each NW. For a given value of B in a hysteresis loop, the numerical simulation yields the equilibrium magnetization configuration and the total magnetic energy E_m corresponding to that configuration. Just as in dynamic cantilever magnetometry (DCM) [164, 167], the frequency shift of each flexural mode is proportional to the curvature of the system's magnetic energy E_m with respect to rotations θ_i corresponding to each mode's oscillation:

$$\Delta f_i = \frac{f_{0_i}}{2k_i l_e^2} \left[\frac{\partial^2 E_m}{\partial \theta_i^2}\bigg|_{\theta_i=0} \right], \tag{3.1}$$

where l_e is an effective length, which takes into account the shape of the flexural mode [168]. Therefore, by numerically calculating the second derivatives of E_m with respect to θ_i at each B, we simulate $\Delta f_i(B)$. Note that, unlike in standard DCM, where the magnetic sample is attached to the end of the cantilever, each NW is magnetic along its full length. Because of the mode shape, each longitudinal segment of the NW rotates by a different angle during a flexural oscillation, experiencing a different tilt of the external magnetic field. We account for this effect by applying a spatially dependent external field in the simulation, rather than altering the geometry, which is impractical. For positive (negative) deflections in experiment, the tilt direction of the field in the simulations increases (decreases) with the z position along the NW. The magnitude of the tilt angle follows the Euler-Bernoulli equation, reflecting the mode shape. We choose a maximum oscillation amplitude (at the tip) large enough to account for the finite precision of the simulation. The torque signal can then be calculated using a finite difference approximation for the second derivative in equation (3.1) and the simulated magnetic energy of the system for small positive, negative, and no deflection (see Section 3.1.3) [167].

The excellent agreement between the measured and simulated $\Delta f_i(B)$ in Figure 3.2 is typical for all measured NWs. For each NW, the mechanical parameters used in the simulation are extracted from measurements of the thermal motion at $B = 0$, while geometrical parameters are estimated from SEM images. We adjust the value of the saturation magnetization M_{sat} in order to bring the curves into agreement, giving us a sensitive measurement of this material property. M_{sat} is found to be $1.1(1) \times 10^6\,\mathrm{A\,m^{-1}}$, where the uncertainty is dominated by the estimation of the NW geometry from SEM. While the saturation magnetization of bulk Co is $1.4 \times 10^6\,\mathrm{A\,m^{-1}}$, the expected metallic composition of as-grown Co NWs grown by FEBID varies between 70 and 95%. This reduced Co content makes our measured value consistent with expectations as does a comparison with electron holography measurements in similar NWs, yielding $M_{\mathrm{sat}} \simeq 1.2 \times 10^6\,\mathrm{A\,m^{-1}}$ [163]. In addition, the simulations show that the magnetization of the NWs is axially aligned in remanence for up to about 40 mT of reverse field. These results are consistent with nanoSQUID measurements of similar Co NWs carried out at 15 K by Martínez-Pérez et al [169]. This axially aligned remanent magnetization can be represented by a magnetic charge distribution in the form of an elongated dipole,

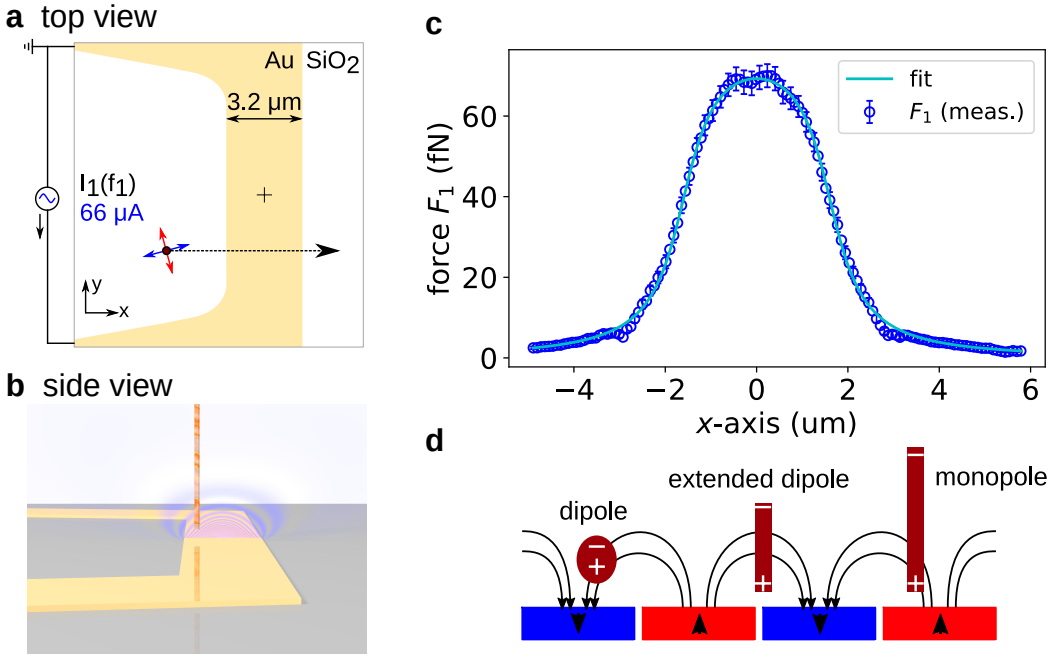

Figure 3.3. – **Tip calibration of Co FEBID NWs**
a) Sketch of the Au wire dimensions, NW mode directions, scanning direction and applied drive tone. **b**) Illustration of the scanning probe measurement. **c**) Measured response of the first mode of NW 4 as a function of position along the line scan indicated by the arrow shown in **a**) to a resonant drive field for a tip-sample distance of $d_z = 200\,\mathrm{nm}$. The best fit according to equation (3.2) is represented by the solid cyan line and yields a value of $q_{\mathrm{tip}} = 9.7(4) \times 10^{-9}\,\mathrm{A\,m}$. **d**) Illustration of three tip models for magnetic tips. The FEBID NWs correspond to the monopole tip model. Figure adapted from [7].

leaving a monopole-like distribution localized at the free end of the NW to interact with an underlying sample, as shown in Figure 3.3d and demonstrated in Section 1.3.2.

Micromagnetic Simulations

The principles of simulating the torque magnetometry signal with micromagnetic solvers are described in Refs. [12, 164, 170]. In these works, it is only the tip of the mechanical resonator which is magnetic, therefore the system can be modelled as a magnetic object oscillating in a homogeneous external magnetic field. The mode shape of the mechanical resonator enters into the calculation only in the form of the effective length, simplifying the mechanics to that of a harmonic oscillator. For the Co NWs, which are both the mechanical resonator and the magnetic object, the mode shape has to be taken into account.

The final geometry used in the simulation of Figure 3.2 is a 9.1 µm long, elliptic cylinder, whose diameters are modulated along the z direction, as determined from the SEM images. The average diameters along the two mode directions are $d_1 = 135\,\text{nm}$ and $d_2 = 125\,\text{nm}$. Space is discretized to 5 nm. Material parameter values are the saturation magnetization $M_{sat} = 1.1(1) \times 10^6\,\text{A}\,\text{m}^{-1}$ and the exchange stiffness $A_{ex} = 38\,\text{pJ}\,\text{m}^{-1}$. The latter has been chosen to match the switching field of the NW, and is significantly larger than other values reported for Co [171–174]. This discrepancy arises because the switching field also depends sensitively on geometrical and material imperfections, which we do not attempt to model. Nevertheless, control simulations confirm that the overall magnetization reversal process and the remanent states are unaffected by such differences in A_{ex}.

In an effort to determine the effect of nanocrystallinity in the NW, we have run simulations with NW divided into grains of around 10 nm size, giving each grain a uniaxial anisotropy with $K_1 = 530\,\text{kJ}\,\text{m}^{-3}$ and a random orientation of the anisotropy axis. We find that this refinement does not significantly change the simulation results with respect to standard simulations assuming homogeneous material without crystalline anisotropy.

3.1.4. Calibration with a known magnetic field profile

In order to determine the behavior of the FEBID NWs as scanning probes, we approach and scan a nearly planar sample with respect to NW 4 at $T_{\text{bath}} = 4.2\,\text{K}$. The sample consists of a 6 µm-long, 3.2 µm-wide, and 240 nm-thick Au wire patterned between two contact pads on a Si substrate (Figure 3.3a and b). By passing a current through the wire, we produce a well-known magnetic field profile $\mathbf{B}_{\text{AC}}(x, y, z)$ given by the Biot-Savart relation, with which we drive NW oscillations and calibrate its response, as done in standard MFM [8, 92, 93]. By applying an excitation current containing two sine waves, each at the frequency of one of the NW modes f_1 and f_2, we drive the NW as we scan it across the Au wire at a fixed tip-sample spacing. Both the resonance frequencies f_i and oscillation amplitudes r_i are tracked using two phase-locked loops. The corresponding values of the force driving each mode on resonance are calculated using $F_i = r_i k_i / Q_i$ (see Appendix C). Figure 3.3c shows the response of mode 1 to a drive current amplitude of 47 µA as we scan the NW, which in the absence of a static external field ($B = 0$) is in a remanent magnetization configuration, above the Au wire at a fixed distance of $d_z = 200\,\text{nm}$. Since the first mode is nearly aligned with the x-direction ($\alpha \approx 7.3\,^\circ$) and thus along the direction of $\mathbf{B}_{\text{AC}}$, the orthogonal second mode has almost no response to the driving tone at f_2 and is not shown.

From our torque magnetometry measurements, we know that the magnetic NWs have an axially aligned remanent magnetization. Because the decay length of the magnetic field from our sample is much shorter than the NW length, the sample fields only interact with the monopole-like magnetic charge distribution at the free end of the NW [7]. This charge distribution then determines the NW's response to magnetic field profiles produced by a sample. For a monopole-like NW tip, we can relate the driving magnetic

field and the force it produces on the NW by (see equation (1.148))

$$F_i = q_{\text{tip}} \mathbf{B}_{\text{AC}} \cdot \hat{\mathbf{r}}_i, \tag{3.2}$$

where q_{tip} is an effective magnetic monopole moment describing the tip magnetization and $\hat{r}_i$ is the unit vector in the direction of displacement of mode i. In this point-probe approximation, we consider the interaction of dipole and higher multipoles of the magnetic charge with the driving field to be negligible. As shown by the agreement between the field calculated from the Biot-Savart law and the measured response of NW 4 in Figure 3.3c, this approximation is valid for our NWs. Control experiments, using the applied magnetic field to initialize the NW magnetization along the opposite direction also show that spurious electrostatic driving of the NW modes is negligible.

In order to extract a value for the monopole q_{tip}, the response of the NW to the driving tone is converted to a force using $F_i = r_i k_i / Q_i$ ($i = 1, 2$ representing the two modes, see equation (1.149)). The interferometric calibration factor between units of signal amplitude in volts and displacement in meters and the measurement position along the wire axis have to be taken into account. We then use equation (C.3) and the monopole model to fit the measured force response of NW 4 by assuming $\mathbf{B}_{\text{AC}}(x, y, z) = [B_x(x, z), 0, B_z(x, z)]$ giving the fit function for the first mode

$$F_1 = q_{\text{tip}} B_x(x, z) \cos \alpha' \tag{3.3}$$

where α' is the angle between x-axis and the NWs first mode direction. It differs from α by the angle between the measurement direction and the optical axis, which is usually within the range of $2\,^\circ$ when centered on the wire. The optical axis is assumed to be aligned with the x-axis. The free parameters of the fit are the value of the monopole q_{tip} and its effective distance $z = z_{\text{mono}}$. A typical fit is shown in Figure 3.3c of the main text for a distance between the tip and Au wire of $d_z = 200\,\text{nm}$ and a driving current of $47\,\mu\text{A}$. The field profile fitting to the response curve locates the effective monopole not at the tip of the NW but higher along its axis at $z_{\text{mono}} = 472(5)\,\text{nm}$.

This behavior is illustrated in more detail in Figure 3.4. The value of the monople is scattered, for different tip-sample distances, in a region around $9.7(4) \times 10^{-9}\,\text{A m}$. This spread can be related, on the one hand, to imperfections of the Au-wire structure resulting in a different field profile and, on the other hand, to the approximate nature of the monopole model used for fitting the data. The tip of the NW, which interacts with the Biot-Savart field of the Au wire, is an extended object. Depending on the tip-sample distance d_z, its effective volume of interaction changes, leading to different values for q_{tip} and z_{mono}. In addition, a small tilt of the NW from the xy-plane can also add error, since it introduces sensitivity to the z-component of $\mathbf{B}_{\text{AC}}(x, y, z)$. It should also be noted that, while the zero-point of the tip-sample distance is precisely determined by a soft touch of the NW tip onto the Au wire, the open-loop piezo translation stage regulating the tip-sample distance in z-direction is subject to piezoelectric creep. We do not consider the nonlinearity that creep introduces to the positioning of the NW. Furthermore, the nature of the open loop scanners also introduces a systematic error of about 5 % in the conversion of the x- and y-coordinates from voltage to µm, depending on the calibration method used.

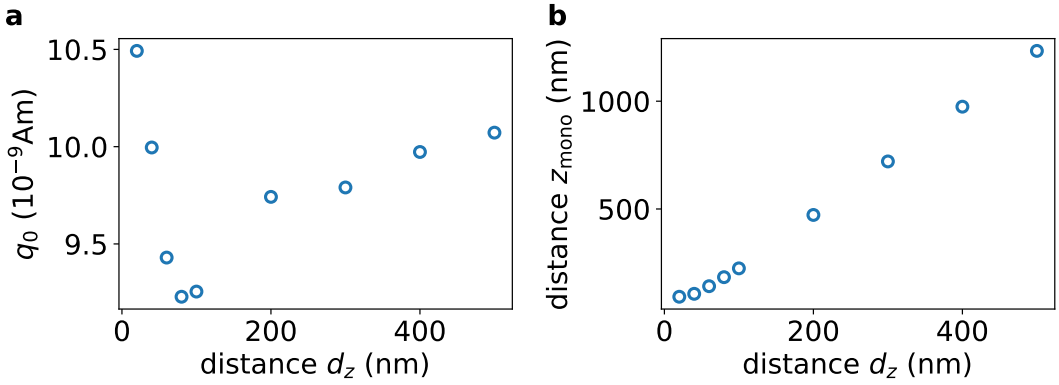

Figure 3.4. – **Point-monopole values**
a) Value of the monopole q_{tip} and **b**) monopole distance z_{mono} plotted against the tip-sample distance d. The monopole distance increases with the tip-sample distance. The fitted value of the monopole is scattered around a value of $9.7(4) \times 10^{-9}\,\text{A m}$ and seems to change substantially below a tip-sample distance closer than the NWs diameter.

Combining measurements at different d_z and different driving currents, we find that NW 4 has an effective magnetic charge of $q_{\text{tip}} = 9.7(4) \times 10^{-9}\,\text{A m}$. Given our thermally limited force sensitivity of $25\,\text{aN}/\sqrt{\text{Hz}}$ at $T_{\text{bath}} = 4.2\,\text{K}$, this value of q_{tip} gives our sensors a sensitivity to magnetic field of around $3\,\text{nT}/\sqrt{\text{Hz}}$. This sensitivity is similar to those of some of the most sensitive scanning probes available, including scanning NV magnetometers and scanning SQUIDs.

The value extracted for q_{tip} is consistent with M_{sat} found in section 3.1.3 and the geometry of the NW. Assuming a perfect cylinder with magnetization M_{sat}, the expected magnetic charge is $q_{\text{tip}}^{\text{cyl}} = M_{\text{sat}}\pi(d/2)^2$, where d is the cylinder's diameter. Given the that the diameters of the NWs range from 105 nm to 120 nm we find $q_{\text{tip}}^{\text{cyl}} = 9.5 \times 10^{-9}\,\text{A m}$ to $12.4 \times 10^{-9}\,\text{A m}$.

Furthermore, the magnetic charge model allows us to estimate the stray field and field gradients produced by the NW tip, so that we can assess its potential for perturbing the magnetic state of the sample below. At a distance of $d_z = 50\,\text{nm}$ from the NW tip, the stray magnetic field and magnetic field gradients are $B_{\text{tip}} = \mu_0 q_{\text{tip}}/(4\pi z_{\text{mono}}^2) \approx 60\,\text{mT}$ and $dB_{\text{tip}}/dz \approx 1\,\text{MT m}^{-1}$. The stray field is of similar size to that produced by a conventional MFM tip [175]. For future NW devices to be less invasive, i.e. having less magnetic charge at their tips, sharper tips than those produced here, which are more than 100 nm in diameter, will be required [176]. The large magnetic field gradients, however, combined with the NWs' excellent force sensitivity may make the NWs well-suited as transducers in sensitive magnetic resonance force microscopy [177].

3.1.5. Magnetic field imaging of permalloy disks

In Figure 3.5, we demonstrate the ability to image sub-micrometer features using a FEBID NW as MFM sensor on a permalloy disk ($Ni_{0.81}Fe_{0.19}$) at $T_{\mathrm{bath}} = 4.2\,\mathrm{K}$. Three disks, 1 µm in diameter and 40 nm-thick, are patterned on top of the Au wire, of which one is imaged. During the scan, the first flexural mode of the NW is electrically driven on resonance using an AC voltage applied between the Au wire and a third lead (Figure 3.5a). Frequency shift and dissipation are recorded using a phase-locked loop. Figures 3.5c and d show a $1.5 \times 1.5\ \mu\mathrm{m}^2$ image of frequency shift $\Delta f_1(x, y)$, as the disk is scanned below NW 4 for $d_z = 100\,\mathrm{nm}$ at $B = 0$ and for $d_z = 150\,\mathrm{nm}$ at $B = 100\,\mathrm{mT}$, respectively. At $B = 0$ (Figure 3.5c), the magnetization of the disk is arranged in a remanent vortex configuration [178], as verified by a micromagnetic simulation carried out with *Mumax3*. Figure 3.5e shows the magnetic image contrast expected from the simulation using the monopole model (3.2), in which the frequency shift of the NW mode is proportional to the stray field derivative along the mode direction. While the contrast measured at the edges of the disk is due to topographic features, the contrast in the center is consistent with what is expected from the stray field of a vortex core. The image taken at $B = 100\,\mathrm{mT}$, Figure 3.5d, shows an almost homogeneous magnetic imaging contrast across the disk. The corresponding simulation in Figure 3.5f agrees well with the measurement and reveals that while the vortex core is still present in the center of the disk, its stray field is overshadowed by the field originating from the outer parts of the disk, where the magnetization tilts out of plane (see figure 3.5g and h). The region of high frequency shift in the bottom right quadrant of Figure 3.5d is explained in the simulation by assuming a small tilt ($\approx 1\,^\circ$) of the disk plane with respect to the external field, resulting in the vortex core being slightly offset from the center of the disk. Although a detailed interpretation of the NW MFM images and a quantitative comparison of the measured and calculated frequency shifts is beyond the scope of this work, they showcase the high sensitivity and potential spatial resolution of the FEBID NWs transducers.

3.1.6. Bolometric heating

In order to investigate any bolometric heating of the nanowires (NWs) due to the readout laser, the thermal noise power spectral density (PSD) is measured at the tip of NW 4 for laser powers from 0.5 to 25 µW in room temperature ($T_{\mathrm{bath}} = 293\,\mathrm{K}$), liquid nitrogen ($T_{\mathrm{bath}} = 77\,\mathrm{K}$), and liquid helium environments ($T_{\mathrm{bath}} = 4.2\,\mathrm{K}$). In addition, the influence of the laser beam's position along the NW's long axis is examined for a fixed laser power of 20 µW. All laser powers provided in this section correspond to the total power at the output arm of the interferometer at the bottom of the probe, not the fraction of the power incident on the NW.

Generally, for high laser powers, a negative resonance frequency shift and a high thermal noise amplitude are observed, corresponding either to an increase in NW temperature or to a decrease in effective mass of the resonator. Since the latter can be excluded, we fix the effective mass to $2.6(2) \times 10^{-16}\,\mathrm{kg}$, as extracted from the highest

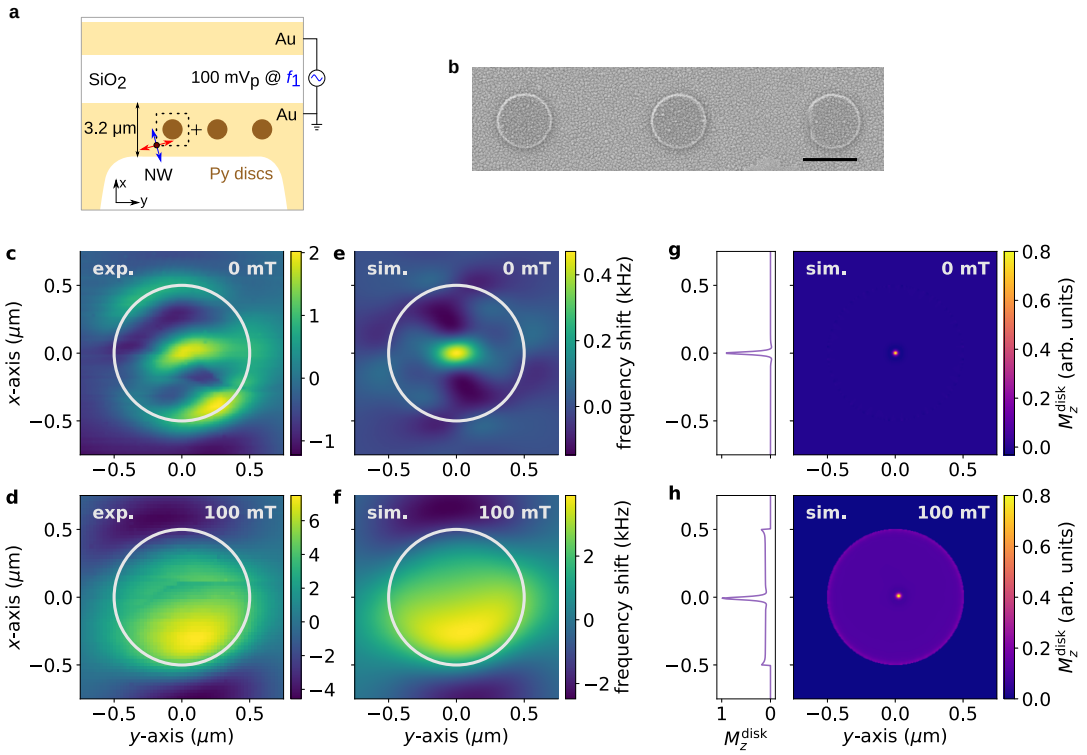

Figure 3.5. – **Imaging of permalloy disks with Co FEBID NWs**
a) Sketch of the Au wire sample with three 1 µm wide permalloy disks patterned on top. The NW is driven resonantly by applying a gate voltage of 100 mV_p amplitude at f_1. **b**) SEM image of the permalloy disks. The scale-bar is 1 µm. **c**), **d**) NW-MFM images using NW 4 with an external magnetic field applied perpendicular to the disk plane of $B = 0$ and $B = 100$ mT, respectively. **e**), **f**) corresponding simulations of the expected contrast obtained by applying the monopole model (3.2) to the disk's stray field calculated by *Mumax3*. The disk circumference is highlighted by a white circle. **g**) and **h**) Out of plane magnetization M_z^{disk} of the permalloy disk simulated with *Mumax* for external magnetic fields of zero and 100 mT, and corresponding line cuts through the vortex core on the left hand side. The slight offset of the vortex core at non-zero external field is due a small tilt of the disk with respect to the B-field direction, which was taken into account for the simulation.

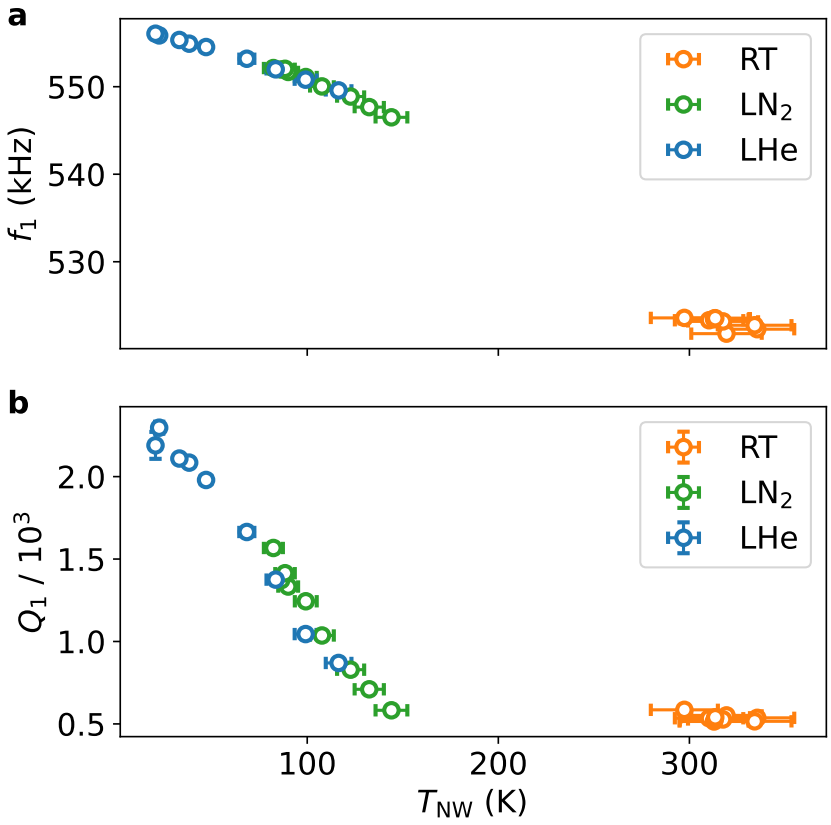

Figure 3.6. – **Temperature dependence of mechanical properties**
a The resonance frequency of NW 4 plotted against the NW temperature for the full data set at all three different bath temperatures. The overlap of the points, especially at $T_{bath} = 77\,K$ and $4.2\,K$, points to a bolometric heating effect. **b** Quality factor Q against the NW temperature. These measurments are carried out with the laser aligned to the tip of the NW, corresponding to the cross (X) in Figure D.1 a.

observed values at small incident laser powers with $T_{\mathrm{bath}} = 293\,\mathrm{K}$. The remaining data is then fitted to equation (1.90) with the NW temperature $T = T_{\mathrm{NW}}$ as a free parameter.

The changes observed in the mechanical properties of the NW as a function of laser power and focal position are a consequence of the temperature dependence of the NW's Young's modulus [124]. A change of the Young's modulus is reflected in a change of a resonators resonance frequency, specifically in a negative frequency shift for higher NW temperatures.

Laser power dependence Appendix Figure D.1 a, c, e show images of NW 4 in reflection with the positions marked, at which the thermal noise PSD is measured as a function of laser power while the bath is held at $T_{\mathrm{bath}} = 4.2,\ 77$ and $293\,\mathrm{K}$. Figure D.1 b, d, f show line cuts of the reflection images along the NW's long axis with the gray area highlighting the spatial extent of the NW. The NW's length is used to calibrate the conversion between piezo scanner voltage and its displacement in µm.

Resonance frequencies, quality factors, and NW temperatures of the first mode are extracted from the thermal noise PSD as a function of laser power at the positions marked with crosses in Figure D.1. On overview across all parameters for the different environment temperatures is plotted in Figure D.2. As we can see for all three bath temperatures, the resonance frequency shows a linear decrease with increasing laser power which is consistent with the temperature dependence of the Young's modulus. As the NW becomes warmer it softens. The quality factor exhibits a similar drop as a function of power for both $T_{\mathrm{bath}} = 4.2\,\mathrm{K}$ and $T_{\mathrm{bath}} = 77\,\mathrm{K}$, whereas at $T_{\mathrm{bath}} = 293\,\mathrm{K}$ it appears constant within the error. The NW temperature increases with laser power at $T_{\mathrm{bath}} = 4.2\,\mathrm{K}$ and $T_{\mathrm{bath}} = 77\,\mathrm{K}$, while at $T_{\mathrm{bath}} = 293\,\mathrm{K}$, it appears roughly constant.

All of the above observations are summarized in Figure 3.6 where we have used the fitted NW temperature T_{NW} as x-coordinate. The readout laser acts as local heat source and seems to fully thermalize the NW to a new temperature. This is supported by the overall temperature behavior and especially the overlap between the data at LN_2 and LHe bath temperatures. Similar curves have been measured in literature for GaN NWs [122]. In the case of silicon cantilevers the frequency dependence is of the same type, whereas the quality factor exhibits a richer behavior related to the temperature dependence of the thermal expansion coefficient during the transition from room temperature to cryogenic temperatures [179].

We can analyze further by fitting the Young's modulus to the semi-empirical Wachtman formula [180] used in references [122, 179]. The Young's modulus for a cylindrical object is related to the spring constant by

$$M_{\mathrm{tot}}\omega_1^2 = \frac{1}{2}\pi(1.8751)^4\frac{ER^4}{L^3} \tag{3.4}$$

where we have used the Euler-Bernoulli natural resonance frequency equation (1.28) for the first order mode and the second moment of inertia for a constant cylindrical

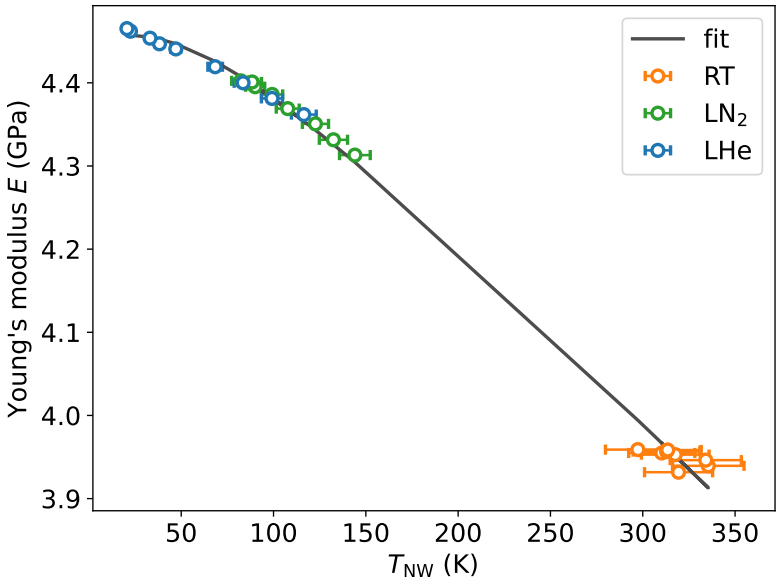

Figure 3.7. – **Young's modulus**
Fit of the temperature dependent Young's modulus to equation (3.5). The found parameters are the zero-temperature Young's modulus $E_0 = 4.46\,\mathrm{GPa}$, the temperature coefficient $B = 2.23\,\mathrm{MPa\,K^{-1}}$ and the Debye temperature $\Theta_D = 214\,\mathrm{K}$.

cross-section[3]. The semi-empirical Wachtman equation is given by [122, 180]

$$E(T) = E_0 - BTe^{-\frac{\Theta_D}{2T}} \tag{3.5}$$

where Θ_D is the Debye temperature. The frequency data is converted to the Young's modulus via equation (3.4) and fitted to equation (3.5) as presented in Figure 3.7. The fit parameters found are $E_0 = 4.46\,\mathrm{GPa}$, $B = 2.23\,\mathrm{MPa\,K^{-1}}$ and $\Theta_D = 214\,\mathrm{K}$. As a caveat the fit uncertainties are large since even small errors in the estimation of the geometry can introduce huge errors in the Young's modulus since the NW length and radius enter with powers of three and four respectively. Compared to the Debye temperature of Cobalt of 460 K [181] we fit a much lower value. The Young's modulus for FEBID structures varies a lot across literature and depends on the specific details of the growth conditions [182]. Generally it is in the range of a few tens of GPa. Our fitted value is much lower than the one found for Co NWs by Zhang et al [183] of around 75 GPa. However they used electrochemical vapor deposition, possibly producing much higher quality samples, also with diameters around 300 nm. Thus our fitted value is probably accurate within the geometrical uncertainties of the Young's modulus discussed above.

Focal spot position dependence For a second set of measurements, the focal spot is moved along the z-axis (long axis) of the NW. Thermal noise PSDs are measured at the

[3] $I = \frac{1}{2}\pi R^4$

points shown in Figure D.1. Figure 3.8 shows the resonance frequency and the NW temperature along the NW, extracted from thermal noise PSDs, while taking into account the mode shape $U(z)$. As the focal spot is moved onto the NW tip and begins to overlap with the NW, the resonance frequency shifts downwards and the NW temperature rises, since maximal power impinges on the NW. At the other end of the NW, close to its base, the laser light is cut off by scattering at the chip edge. Consequently the resonance frequency shifts up by a small amount and the NW temperature is lowered. Since the signal in this region is very faint due to the mode's small displacement at the base and back-scattering from the chip edge, some measurement points for the NW temperature are omitted.

In the middle region of the NW, where the laser focal spot fully overlaps with the NW, we measure a roughly constant NW temperature profile. This behavior is an indication that radiative losses – and not losses from the thermal contact to the substrate – are the dominant channel through which the NW reaches thermal equilibrium. This observation indicates that the NW is well-isolated thermally from the substrate and therefore, through the use of exchange gas to create thermal contact to a sample, could be used as a sensitive thermal scanning probe [184].

3.1.7. Conclusion

In the past, FEBID-grown NWs have been patterned directly on tips of atomic force microscopy (AFM) cantilevers in an effort to improve spatial resolution [65, 68, 176]. Our results make clear that such nanocrystalline metallic NWs can have surprisingly high mechanical quality, making FEBID a promising and versatile method for producing nanometer-scale force transducers. In principle, a FEBID NW patterned on the tip of a standard AFM or MFM cantilever could be used to add sensitive 2D lateral force and dissipation detection capabilities. Such a system would be capable of vectorial force sensing in 3D, i.e. mapping both the size and the direction in 3D of tip-sample forces.

In addition to demonstrating the high-force sensitivity of FEBID-grown NWs, we also show their excellent magnetic properties. The Co NWs measured here maintain a saturation magnetization, which is 80% of the value of pure Co. They also have an axially aligned remanent magnetization with a switching field around 40 mT. These magnetic properties, combined with the aforementioned mechanical properties, make these NWs among the most sensitive sensors of local magnetic field. The ability to fine tune the NW geometry, especially making them thinner and sharper, may allow for even better field sensitivities and spatial resolutions in the future. NW MFM with such transducers may prove ideal for investigating subtle magnetization textures and current distributions on the nanometer-scale, which – so far – have been inaccessible by other methods.

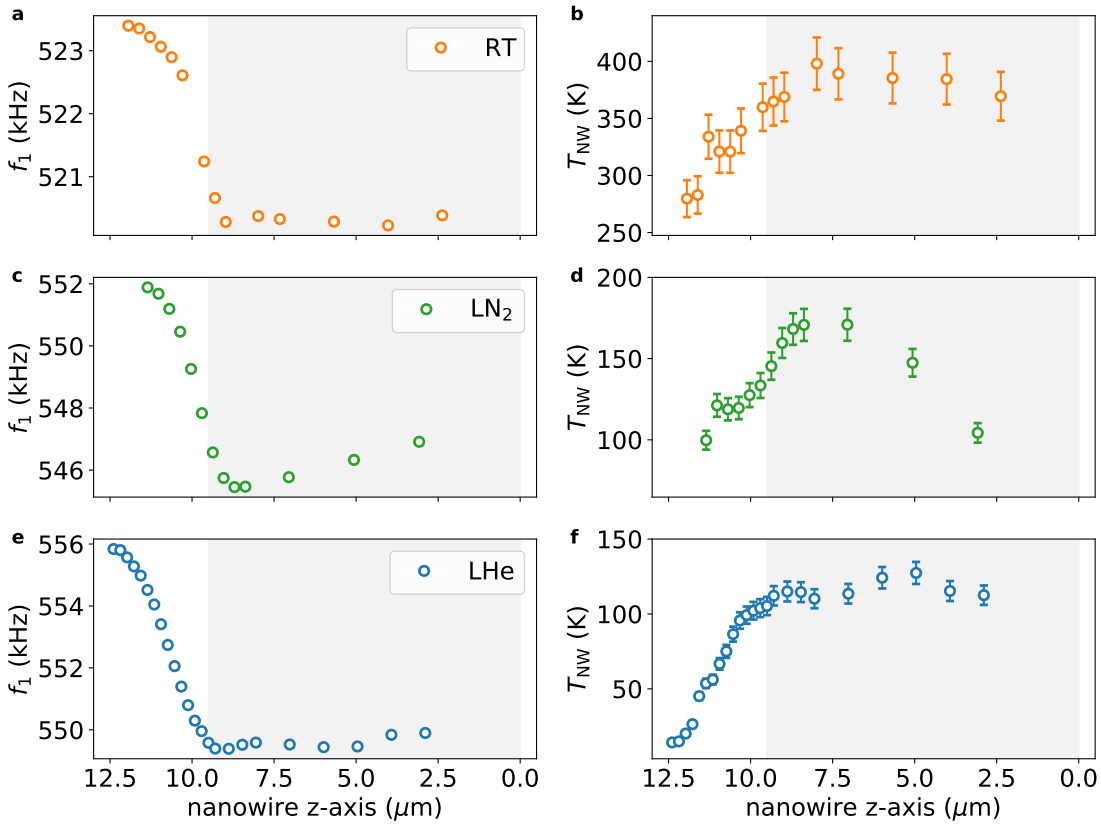

Figure 3.8. – **Mechanical properties along the NW axis**
a–**f** Resonance frequency and NW temperature at different points along the long axis of NW 4. The gray boxes mark the spatial extent of the NW. Moving the NW into the laser results in a lowering of the resonance frequency since the amount of incident power increases on the wire, thus heating it up. Once the NW is fully immersed in the laser beam, the NW temperature is roughly constant. The drop for the data at $T_{\mathrm{bath}} = 77\,\mathrm{K}$ in **d** can be explained by a small piezo drift perpendicular to the wire axis. Close to the base point the NW temperature decreases again due to a portion of the laser light being scattered at the chip edge. *Note*: The abscissa is inverted and its origin corresponds to the base point of the NW.

3.2. Silicon nanowires with cobalt FEBID tips

In this section we will present a new type of NW probe for magnetic imaging which was perceived to combine the high mechanical properties of Si NWs with a Co FEBID tip for magnetic contrast formation, avoiding challenges such as bolometric heating or spurious resonances due to a large linewidth (see Sections 3.1.6 and 2.3). The goal is to ideally retain a magnetic monopole-like tip. The Si NWs were fabricated by the Budakian group[4] and exhibit an extremely good force sensitivity at 4.2 K with the best values of around $500\,\mathrm{zN}/\sqrt{\mathrm{Hz}}$ [16]. Here we will focus on a single fabricated probe that was used later on to image an $EuGe_2$ bilayer[5].

3.2.1. Mechanical properties

Figure 3.9 shows scanning electron micrographs of the fabricated Si NW (3.9a) and a close-up of the Co FEBID tip deposit (3.9b). The dimensions of the Si NW are $L_{\mathrm{Si}} = 21.05(25)\,\mu\mathrm{m}$ without the tip deposit and $d_{\mathrm{Si}} = 172(5)\,\mathrm{nm}$ as inferred from SEM images (see Appendix Figures E.1 and E.3). The tip deposit, using a beam current of 100 pA at an acceleration voltage of 5 kV for a duration of 30 s, starts growing from the side of the droplet at the end of the Si NW and then aligns itself vertically following the direction of the highly focused electron beam. Its diameter expands from roughly 80 nm at the base to around 150 nm at the biggest point, forming an elongated drop-like shaped object. It can only be speculated why the deposition process resulted in this geometry, since we were aiming for a cylindrical tip coaxial to the long axis of the Si NW. Probable reasons are misalignment of the electron beam, charging issues, secondary deposition or pressure gradients of the precursor gas. We can estimate the mass of the resonator from the volume density of Si as follows[6] $M_{\mathrm{tot}} = \rho_{\mathrm{Si}} V = \rho_{\mathrm{Si}} \pi L_{\mathrm{Si}} d_{\mathrm{Si}}^2/4 \approx 1.14 \times 10^{-15}\,\mathrm{kg}$ ignoring the contribution from the tip deposit.

The mechanical properties can be obtained from fitting the thermal noise PSD to equation (1.2.4) as in the previous section. The resulting fit values from two representative spectra taken close to the tip of the NW at room- and LHe temperature are displayed in Table 3.2. The effective mass is fixed to the lowest observed value at room temperature at $M = 0.32 \times 10^{-15}\,\mathrm{kg}$. This agrees reasonably well with the value calculated from the mass density above $M = M_{\mathrm{tot}}/4 \approx 0.285 \times 10^{-15}\,\mathrm{kg}$. Deviations to a higher value can be explained by the additional motional mass of the tip deposit and the extended spot size of the readout laser still covering a part with a mode shape $U_1(z) < 1$.

The quality factor increases during the cooldown by a factor of almost 10 to roughly 20 000. We observe however a substantial loss in quality factor compared to the native Si NWs without tip deposit, that can reach quality factors in excess of 10 000 at room temperature and close to 60 000 at LHe temperature [16]. The difference is attributed to the FEBID deposition process which might cover the sidewalls of the NW by secondary electron scattering and causing friction losses. We observe this effect for all NWs with

[4] University of Waterloo, Waterloo, Ontario, Canada
[5] Publication in preparation
[6] $\rho_{\mathrm{Si}} = 2329\,\mathrm{kg\,m^{-3}}$

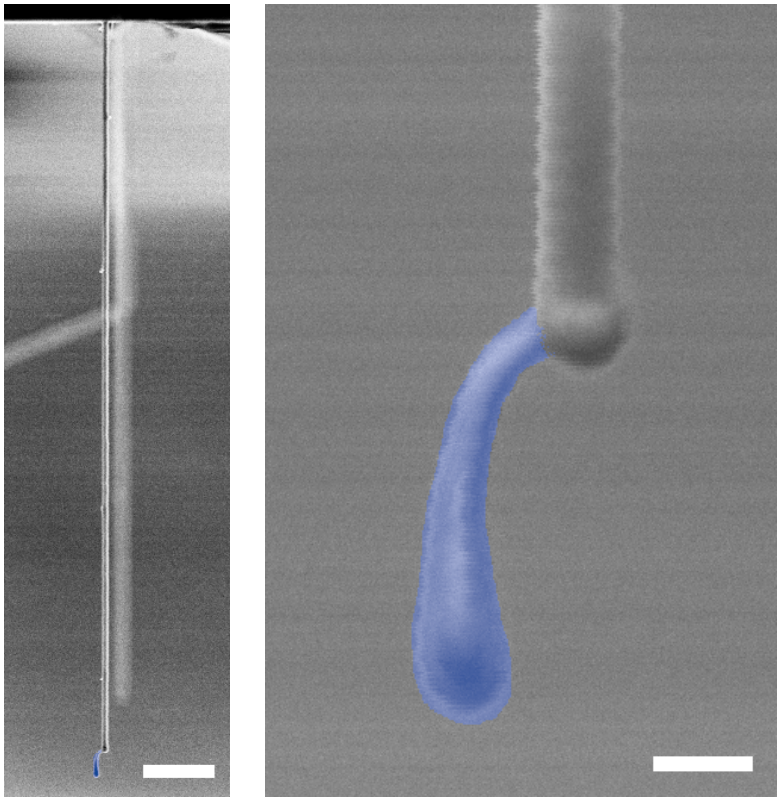

a. Full NW **b.** Co tip

Figure 3.9. – **SEM of a Si NW with Co FEBID tip**
Scanning electron micrograph of a Si NW with Co FEBID tip. (a) shows the full NW along its length. The scale bar indicates 2 µm. (b) is a close-up of the NW tip. The Co FEBID deposit is highlighted in false color (blue) and the scale bar corresponds to 200 nm.

Table 3.2. – Mechanical properties of the Si NW with Co FEBID tip
Presented are the resonance frequencies f_1 and f_2 of the two modes and their splitting Δf_m as well as their quality factors Q_1 and Q_2. T_bath is the bath temperature and M the effective mass.

T_bath	f_1 (kHz)	f_2 (kHz)	Δf_m (kHz)	Q_1	Q_2	M (10^{-15} kg)
295	347.648	349.577	1.929	1962(4)	2036(13)	0.32
4.2	353.460	355.364	1.904	18045(19)	16998(450)	0.32

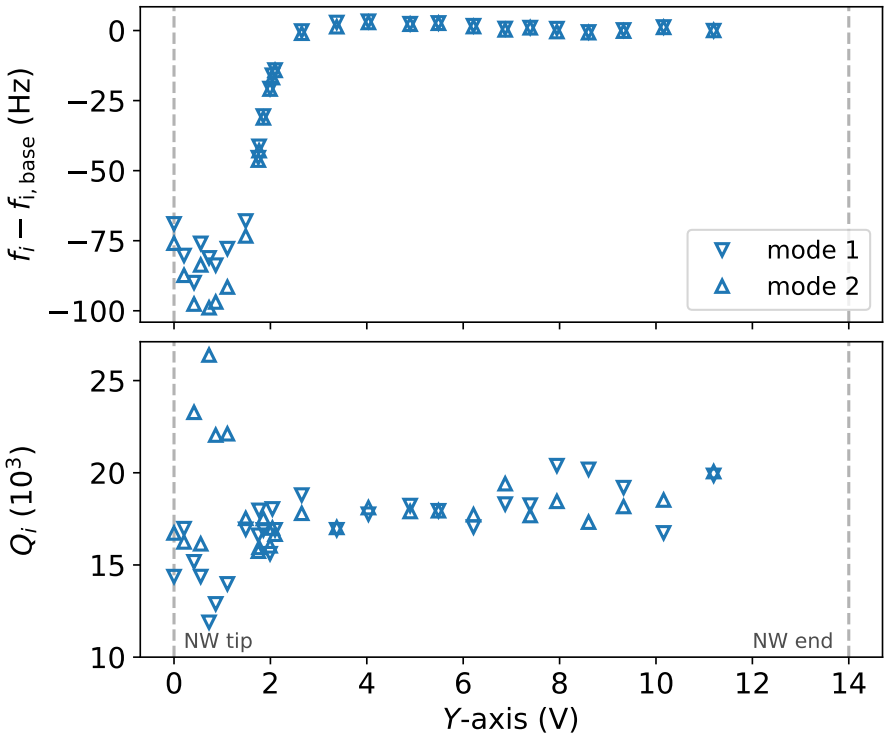

Figure 3.10. – **Si NW along axis at LHe temperature**
Moving the focal spot of the readout laser along the NW axis results in a frequency shift of close to −100 Hz when approaching the tip. This is consistent with bolometric heating of the Co FEBID tip as reported in Section 3.1.6. *Remark*: Bottom z-scanner voltages above 10 V are fictional and just a consequence of stepping during the acquisition of the points and stitching the data.

a Co FEBID tip. Evidence of side wall deposition is shown in the Appendix Figure E.4 for a *different* NW from the same batch of fabrication. The resonance frequencies shift about 2 kHz upwards from room temperature to LHe temperature which is consistent with the temperature dependent change of the Young's modulus.

Heating effects

In the same manner as for the full Co FEBID NWs discussed in Section 3.1 we will also investigate if and how the NW is influenced by the readout and driving lasers. At room temperature we do not observe any significant change in resonance frequency or quality factor as the position of the readout laser is changed along the NW-axis. The data is shown in the Appendix Figures E.6 and E.7. In contrast to the previous section the readout laser is only moved approximately half way along the NW since the scanning window is smaller than the NW length at low temperature.

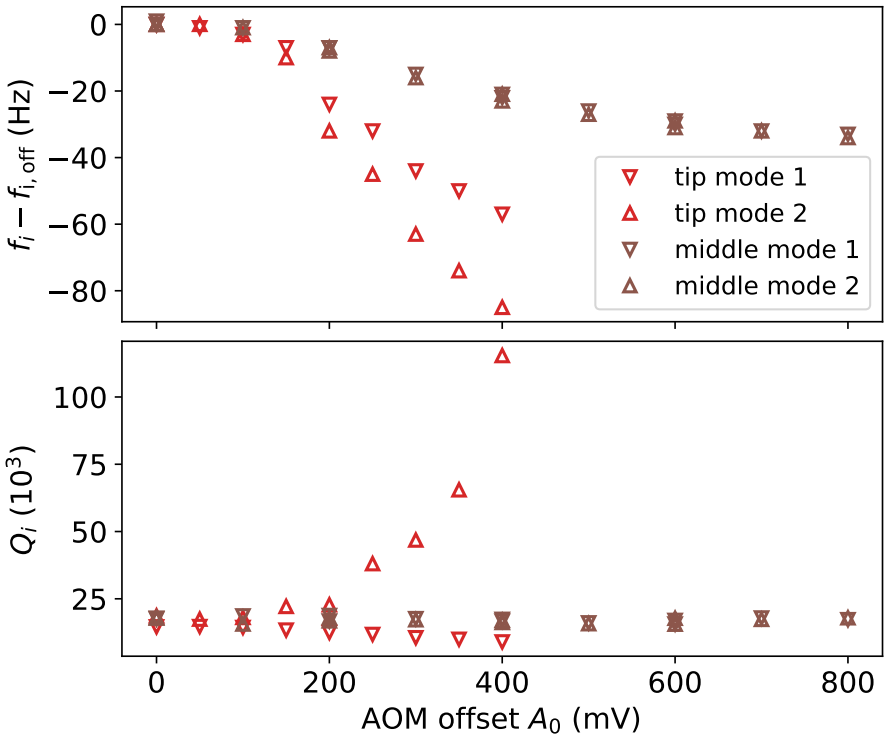

Figure 3.11. – **Heating effects of the driving laser at tip and working point** Resonance frequencies and quality factors for both modes (down and up triangles for lower and upper mode) at the tip and at the working point half-way to the substrate of the NW for different driving laser powers. At the tip (red) the behavior is vastly different between the two modes, pointing to a highly non-linear interaction with the driving laser. At the working point (brown) however the resonance frequencies decline in sync due to bolometric heating and the quality factors stay constant.

At LHe temperature however we observe a significant down shift in frequency of maximal about 100 Hz when moving from the Si shaft onto the tip of the NW as shown in Figure 3.10. As long as no light is incident on the Co FEBID tip the resonance frequency is stable. Once the tip becomes illuminated, light is absorbed by the tip deposit and leads to bolometric heating as discussed in Section 3.1.6. The change in Young's modulus leads to a down shift in the resonance frequencies. The quality factors seem to be affected negatively as well in this region decreasing by approximately two thirds in the worst case. During imaging operation the readout laser is, in any case, positioned about half-way between the tip and the substrate or even closer to the base, where both the resonance frequencies and quality factors are stable. This process avoids any significant bolometric heating effects as are present for the full Co FEBID NWs.

In order to investigate the influence of the driving laser on the NW properties we

moved to the tip and to the working point about half-way to the base of the NW. In these two positions the AOM offset A_0^{AOM} was varied and the corresponding data is presented in Figure 3.11. There is a clear difference between the two positions. At the tip with increasing driving laser power the modes exhibit a down shift in frequency which is expected from the bolometric heating effect. Interestingly both modes are not affected in the same way. For the second mode the down shift is stronger with more that 80 Hz at an AOM offset of 400 mV. The asymmetric behavior becomes fully apparent by taking into account the quality factor. The first mode is damped down while the second mode is subject to a substantial increase of the quality factor to more than 100 000. Since both resonance frequencies are not influenced in the same way this difference cannot be attributed to bolometric heating. Due to the asymmetry of the tip the most likely explanation is the presence of a strong non-linear coupling possibly mediated by strong optical gradients from the readout laser since the Co tip deposit exhibits different optical properties compared to the silicon. Unfortunately no further measurements at different positions inside the beam waist were taken to verify the above hypothesis.

At the working point the influence of the driving laser is less impactful. The resonance frequencies shift downwards compared to the value where the driving laser is switched off by an amount of roughly 30 Hz in both mode simultaneously. The fact that both modes are moving side by side indicates bolometric heating. The quality factors remain constant. We can conclude that at the working point, apart from a small heating induced overall shift of the resonance frequency, a scanning measurement should be undisturbed by the driving laser. Additionally this hints again to the nature of the driving mechanism at the shaft of the NW being mainly photothermal instead of radiation pressure based.

3.2.2. Magnetic properties

The magnetic properties of the Si NW with a Co tip grown by FEBID are assessed in very much the same way as in the previous section about the full Co FEBID NWs.

Magnetometry

The first measurement conducted was a magnetometry, sweeping the external magnetic field directed in parallel to the NW axis from −8 to 8 T and back while recording the resonance frequencies of both modes. The results are depicted in Figure 3.12 for two ranges of magnetic field. The coarse curve over the full field region follows a V-shaped form consistent with a uniform magnetization along the NW-axis, leading to a monotonic stiffening of the effective spring constant towards higher magnetic fields.

Zooming in to the low field region shown in the right hand side of Figure 3.12 we can extract the switching field, at which the magnetization reverses, to be between 60 to 80 mT. Repeatedly crossing this field region reveals that the switching field is spread out and not fixed to a constant value. An additional observation discriminating the current case from the full FEBID NWs is the hockey stick-like shape of the magnetometry data around the zero-field region. After crossing 0 T from either side the frequency starts to decrease at a slower rate and even rise a bit before finally switching to a fully reversed

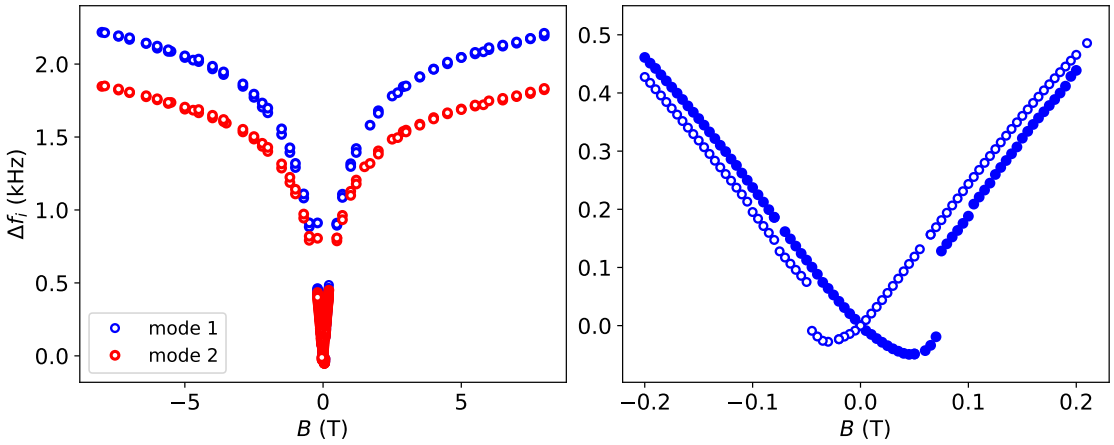

Figure 3.12. – **Magnetometry of a Si NW with Co FEBID tip**
The left hand side shows the full magnetometry data of a field sweep from −8 to 8 T and back. The V-shaped form is consistent with a cylindrical tip magnetized along its long axis. The right hand side zooms in to the low field data showing only the lower mode frequency shift (filled circles for up-sweep and empty circles for down-sweep). The switching field is between 60 to 80 mT. Interestingly the frequency starts to shift upwards already before the switching point, indicating instability in the magnetization already in small reverse fields.

state possibly even leaving the tip demagnetized at some stage. This behavior can be explained by parts of the tip magnetization already starting to change as soon as the tip experiences a reverse field. A beautiful illustration of this effect is shown in Figure 3.13 showing images of a current loop carrying a fixed current, imaged at a succession of different external fields crossing from positive to negative values.

The above behavior comes as no surprise because of the peculiar geometric shape of the tip. The shape anisotropy is not strong enough to hold the magnetization against the reverse field. A consequence for imaging is that discrimination of magnetic field contrast by simply switching the tip magnetization while simultaneously keeping the external field (almost) unchanged becomes nearly impossible, since the tip does not switch sharply to the opposite magnetization state. Inspecting the magnetometry data carefully, little jumps are also visible at some fields indicating further switching of small parts of the tip.

Biot-Savart field calibration

In order to estimate the imaging capabilities and the magnetic tip model we again performed a calibration with a known Biot-Savart field originating from a rectangular conductor (see Appendix C). The dimensions of the Au microwire used here were $h = 60\,\mathrm{nm}$ and $w = 1.1\,\mu\mathrm{m}$. Recording line cuts at different heights for a defined current running through the microwire gives field profiles similar to the full FEBID case, exhibiting a bell shape corresponding directly to the in-plane field profile expected from a rectangular conductor. This is a telltale sign of the magnetic imaging contrast being dominated by the monopole term of the point pole expansion in equation (1.148). The measured force data related to the amplitude response by equation (1.149) is depicted in the appendix Figure E.10 and subsequently fitted to the force expansion using only the monopole term.

The fit results reveal the values of the tip monopole charge q_{tip} and the monopole offset Δz_{mono} and are shown in Figure 3.14 for different tip-sample distances at zero field and 4 T. It is evident that the magnetic monopole charge is dependent on distance, increasing with smaller tip-sample separation, ruling out a perfect monopole behavior. The distance dependence can be explained by the changing size of the magnetic tip volume effectively interacting with the sample stray field. The closer the tip the bigger is the tip section measured from the apex that contributes meaningfully to the magnetic contrast formation.

A second observation is the divergence between the first and the second mode data becoming apparent at small tip-sample distance of 100 nm and below. Above this threshold the extracted values for q_{tip} agree well between the two modes. The deviation can be related to the largest tip diameter being roughly 150 nm. For the full FEBID NWs we also observed a significant change when the tip sample distance dropped below the NW diameter. This is to say that at tip-sample distances below the NW tip diameter the imaging transfer function becomes more convolved and is not explained easily by a simple geometric model as is well underlined by different responses along the two mode directions. Furthermore the data at zero field and 4 T are offset, with the high field

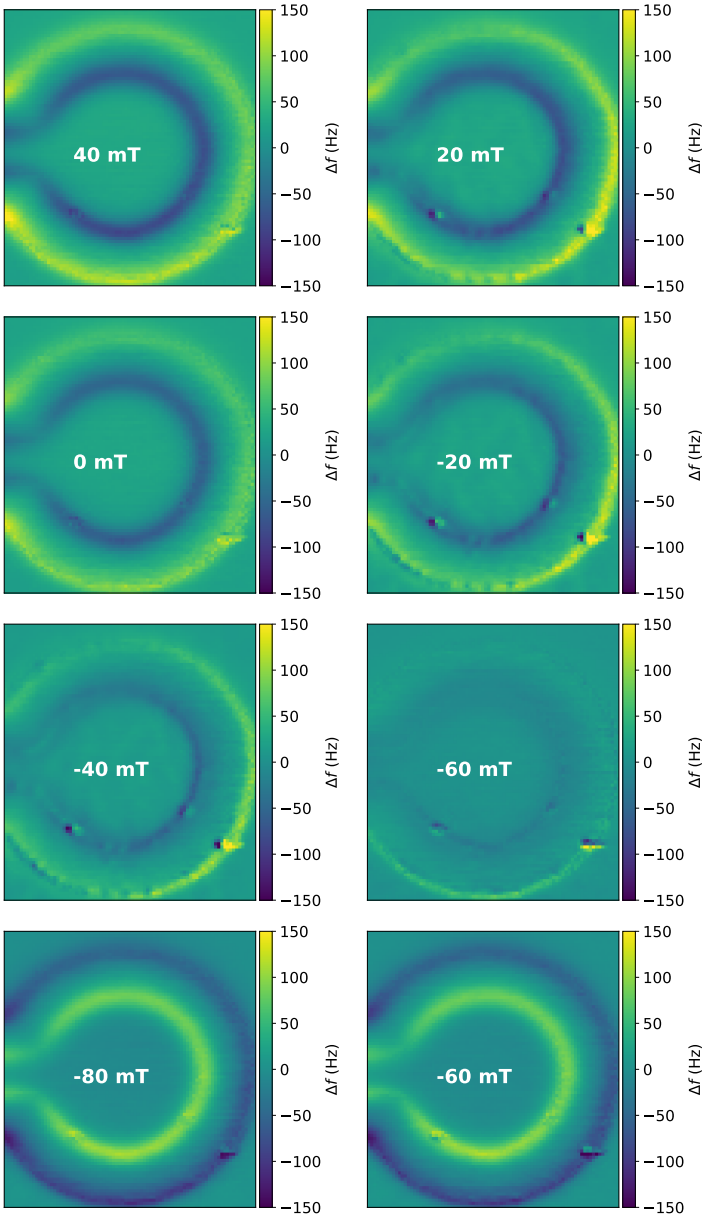

Figure 3.13. – **External field series of DC-current loop images**
The external field is swept from positive to negative fields while a fixed DC current of 70 µA is passed through the Au wire loop. The progression is left-to-right, top-to-bottom and the data shown is the combined normalized frequency shift of both modes. As the field is lowered and crosses into the reverse we loose imaging contrast. Shortly before the switching field (first image at −60 mT) almost no contrast is visible, pointing to a nearly demagnetized tip. Once the tip has switched (image at −80 mT and then back to the second image at −60 mT) the contrast is inverted and we recover the same magnitude as before at positive fields. The distance was 170 nm and for each image the background – acquired during a second scan with zero current passing through the loop – is subtracted.

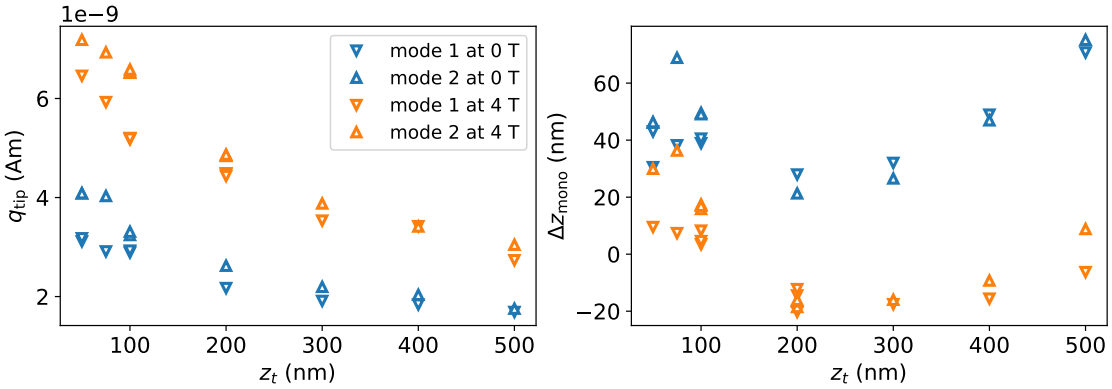

Figure 3.14. – Monopole fit of response to an AC Biot-Savart field at resonance for a Si NW with Co FEBID tip
The left plot shows the fitted monopole charge q_{tip} at different tip-sample distances z_t at zero field and 4 T. The value increases with decreasing tip-sample spacing. For the high field data we fit a slightly higher value. The right plot depicts the monopole offset $\Delta z_{mono} = z_{fit} - z_t$ as defined in Section 1.3.2. The data for both field values show the same U-shaped behavior. The y-axis might be subject to a systematic error introduced by the touch-point calibration procedure.

values for q_0 moved to higher values. Most likely the external field forces the tip magnetization to be more homogeneous at the surface regions of the tip structure thus leading to systematically higher value for the monopole charge.

One caveat to the absolute value of the monopole charge lies in fixing the mode shape at the working point along the NW axis where the data is taken. Since a satisfactory fit of the mode shape is obscured by the heating effect of the tip, we have to take an educated guess of the NW temperature in order to fit for the modeshape at the shaft of the NW. The NW temperature was fixed to $T_{NW} = 11$ K which is well supported by the mode shape values obtained further down the NW close to the base point and assuming the NW is well equilibrated with the rest of the microscope[7]. Thus the absolute value of q_{tip} can easily differ by an estimated 15 % considering also the uncertainties in tip-sample distance. In any case, comparing the found value to that of the full Co FEBID NWs we retrieve a smaller q_{tip} pointing to a lower Co concentration inside the tip deposit. This is very much expected as the growth conditions for the probes discussed here were not optimized for a high Co content but for obtaining a probe magnetized in a useful way, also having to reduce the beam current for deposition in order to avoid charging of the Si NWs. A lower Co content is further supported by an energy dispersive X-ray analysis (EDAX) performed on a different tip deposit on top of another NW yielding a Co content of about 44 % (see Appendix E.2).

[7]Without exchange gas and additional copper braids to the base plate, the system equilibrates at roughly 11 K. Higher temperatures here would result in smaller mode shapes and eventually higher values for q_{tip}.

The second value that can be extracted from the Biot-Savart field profile fit is the monopole offset Δz_{mono} and is depicted on the right hand side of Figure 3.14. It follows a U-shaped curve and describes the location of the fictive magnetic monopole with respect to the apex of the tip. The curves at the two fields are both again subject to an uncertainty of about 10 nm arising from the distance calibration procedure. Nonetheless we can state that the point monopole at 4 T is located closer to the tip apex than at zero field, which is again consistent with the magnetization of the surface layer of the tip deposit being forced into a more homogeneous state. Especially at the tip apex one would expect the magnetization at remanence to diverge from an axially aligned state up to a certain distance within the tip deposit where it would start following the shape anisotropy. Furthermore we observe a similar divergence of the two modes at tip-sample distances smaller than 100 nm that was already present for the q_{tip} fits.

We can conclude that the NW probe characterized above follows the monopole model well enough for a qualitative interpretation of frequency shift data. However extracting quantitative values for a measured stray field may prove difficult to be reliable across a range of different distances and spatial frequencies but are possible within large margins of errors.

3.2.3. Field sensitivity

Resonant field sensitivity

In order to gauge the sensitivity to an electrical current generating a Biot-Savart field we positioned the NW at the center of the rectangular conductor, where the in-plane field component exhibits a peak. The tip was retracted by 250 nm from the top surface of the Au microwire. Subsequently the driving current is lowered to zero and for each current its frequency is swept across the lower mode resonance recording amplitude and phase response. Fitting the sweep data with the harmonic oscillator line shape yields the peak amplitude at resonance which is plotted on the left hand side of Figure 3.15 against the different driving currents. As expected the response approaches the theoretical thermally limited value[8] of $r_{1,\mathrm{rms}}^{\mathrm{th}} = \sqrt{4k_B T BW/2\omega_1^2\Gamma_1} \approx 29\,\mathrm{pm}$ indicated by the dashed grey line, taking into account the measurement bandwitdh of $BW = 0.5\,\mathrm{Hz}$. The temperature was again taken to be 11 K based on the discussion in the previous section. The almost perfect agreement with the fits to the sweep data at zero driving currents underlines the validity of our assumptions and demonstrates a thermally limited measurement.

On the right hand side of Figure 3.15 the sweep data for zero current and 3.5 nA are plotted including their fits to the harmonic oscillator line shape. The signal at resonance is still by a factor of ≈ 1.4 above the thermal background. This is further illustrated by the phase data shown in the appendix Figure E.11. At zero driving current the the phase is completely incoherent, whereas as soon as it is switched on we observe that the characteristic π-shift starts to emerge.

In a last step we can estimate the sensitivity to magnetic field. For this we need to know the peak value of the Biot-Savart field component along the mode direction r_1 for

[8] The additional factor of $1/\sqrt{2}$ is due to the normalization to RMS-values.

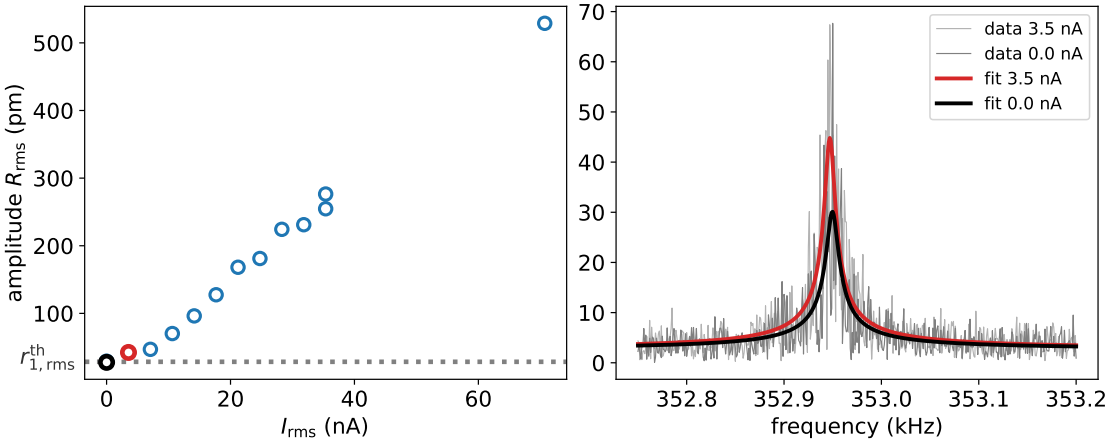

Figure 3.15. – Current sensitivity of Si NW with Co FEBID tip
The NW is positioned at the center of a Au microwire analog to the situation depicted in Figure 3.3, where the in-plane component of the Biot-Savart field is the strongest. The tip sample distance for all measurements is $z_t = 250\,\text{nm}$. The left hand side plot shows the peak amplitude response for different AC-current strength I_{rms} running through the microwire. The right hand side depicts two frequency sweeps at a current of $I_{\text{rms}} = 3.5\,\text{nA}$ (red) and no driving current at all (black) corresponding to purely thermally driven motion. Grey are the data and the solid colored lines represent the fits. Calculating the Biot-Savat field at a distance of 250 nm for a current of 3.5 nA gives a peak magnetic field of 1.97 nT, which is close to the thermally limited value of $B_{\text{min}} = 2.0\,\text{nT}$.

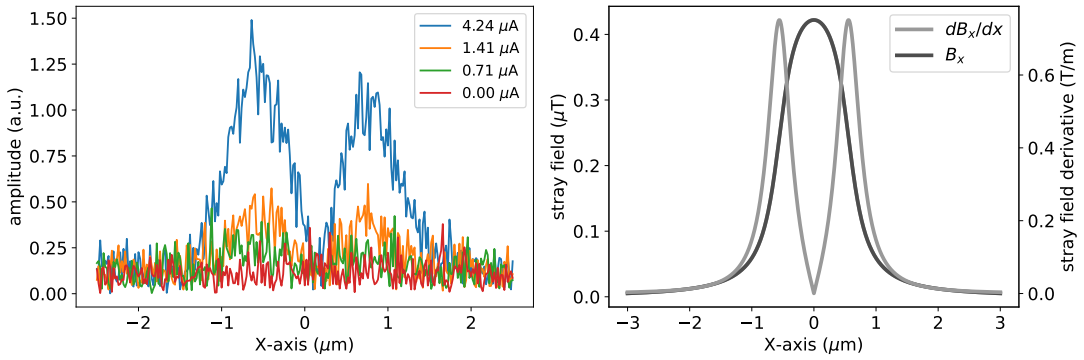

a. Quasi-DC linescans **b.** Simulation for 1 µA

Figure 3.16. – **Gradient sensitivity from quasi-DC Biot-Savart field**
A quasi-DC current is passed through the Au microwire. (a) Tandem-demodulated resonance frequency of the first mode at a frequency of $f_{\mathrm{ref}} = 80\,\mathrm{Hz}$ for different currents. Even at currents below 1 µA a signal can still be observed. (b) Simulated Biot-Savart field profile and the absolute value of its derivative for a reference current of 1 µA at a distance of 200 nm. The form of the derivative matches the data in (a) and we demonstrate a quasi-DC sensitivity to sub-micro tesla fields or gradients on the order of $1\,\mathrm{T\,m^{-1}}$.

a current of 3.5 nA at a tip-sample distance of 250 nm. Turning to Appendix Section C this value is $B_{\mathrm{B-S}} \approx 2.0\,\mathrm{nT}$. The theoretical force sensitivity on the other hand is given by equation (1.94) and yields[9] $F_{\mathrm{min}} \approx 3.4\,\mathrm{aN}$. By assuming a monopole charge of $q_{\mathrm{tip}} \approx 2 \times 10^{-9}\,\mathrm{A\,m}$ at 250 nm tip-sample distance (see Figure 3.14) we convert this to a thermally limited field sensitivity of $B_{\mathrm{min}} = F_{\mathrm{min}}/q_{\mathrm{tip}} \approx 1.7\,\mathrm{nT}$ (corresponding to $2.4\,\mathrm{nT}/\sqrt{\mathrm{Hz}}$ normalized to the bandwidth) and find that the experimental and theoretical value agree very well. Of course moving closer to the microwire would increase the value q_{tip} that has to be used. For example at a distance of 100 nm we have that $q_{\mathrm{tip}} \approx 3 \times 10^{-9}\,\mathrm{A\,m}$ and the theoretical thermally limited field sensitivity would equate to $B_{\mathrm{min}} \approx 1.6\,\mathrm{nT}/\sqrt{\mathrm{Hz}}$ normalized to the bandwidth.

DC field sensitivity

At last we assess the sensitivity to magnetic for two different cases close to DC since not every sample allows for modulating its magnetism at NW resonance frequencies of a few hundred kHz. First, we will use a quasi-DC field at a small frequency offset from DC, which simultaneously is a convenient way to separate the magnetic signal from unwanted force gradients e.g. arising through electrostatic interactions. Second, we will use a true DC current passing through a loop to demonstrate DC imaging.

[9] For a bandwidth of $BW = 0.5\,\mathrm{Hz}$

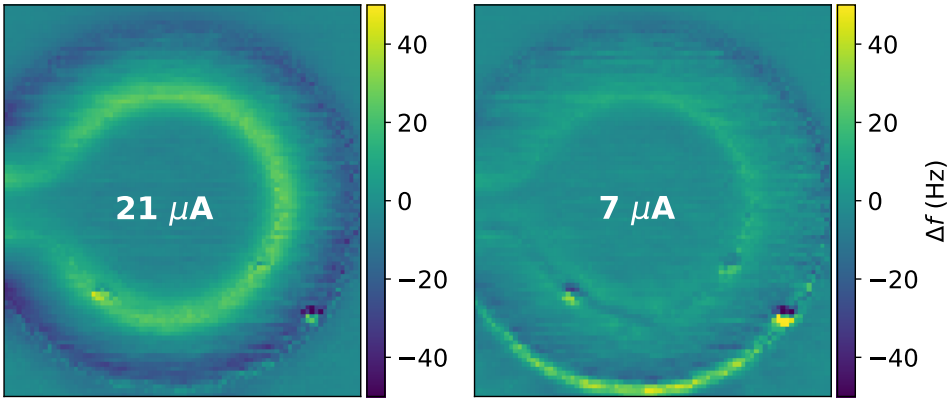

Figure 3.17. – DC imaging of a current loop
Images of an Au loop at a distance of 190 nm, passing DC currents of 21 µA and 7 µA. For each image the background is acquired in a second pass with zero current and subsequently subtracted. As scale reference, the inner diameter of the loop is 5.5 µm and the width of the wire 1.2 µm with a thickness of 60 nm.

Quasi-DC The NW tip is scanned across the same microwire as before at a distance of 200 nm. A current running at an arbitrary quasi-DC frequency within the PLL-bandwidth of $f_{\mathrm{ref}} = 80\,\mathrm{Hz}$ provides a slowly oscillating Biot-Savart field. The NWs first mode resonance frequency is locked with a PLL and then, during the line scan, demodulated a second time at f_{res} using a tandem demodulation scheme. The results for different current strengths are shown in Figure 3.16. From the doubly demodulated data (3.16a) we can obtain a limit for the field gradient at which the signal is just above the noise floor. At a current of 1.41 µA or slightly lower a response is still observed. Figure 3.16b shows the Biot-Savart field of a rectangular conductor at a distance of 200 nm and the absolute value of its derivative at a reference current of 1 µA. Thus the NW responds to fields slightly below 1 µT producing field gradients of the order of $1\,\mathrm{T\,m^{-1}}$.

True DC In order to gauge the sensitivity to true DC fields we are taking subsequent images of an Au loop patterned on a Si substrate, the first with a known current passing though the loop and the second with the current source switched off. This allows to subtract the two images and extract the magnetic contrast. Figure 3.17 shows the processed images, combining the shift of both modes, for DC currents of 21 µA and 7 µA. In the image with lower current the characteristic pattern of an up- and then down-shift when moving radially across the loop wire is still visible. This means even in DC we retain a sensitivity to fields of a few µT, or rather the gradients of a few

$\mathrm{T\,m^{-1}}$. For DC measurements an excellent long-term stability of the system is key since consequent measurements can easily take hours. In both images of Figure 3.17 we observe that at some points noise punches through and is visible in the processed image. This demonstrates very well the inherent challenges of imaging DC fields with MFM probes, since any topographic artifact or electrostatic instability[10] will contribute to the noise in the captured image. Hence it comes as no surprise that we slightly miss the theoretical thermally limited field gradient sensitivity of roughly[11] $1.3\,\mathrm{T\,m^{-1}}$ for an oscillation amplitude of $r_1 = 10\,\mathrm{nm}$ (see Table 1.1).

[10] Unfortunately we did not have the ability to set the tip to a known electrostatic potential with this specific probe.

[11] For a PLL bandwidth of 30 Hz.

4. Summary and Outlook

4.1. Summary

In the first chapter we developed the theoretical groundwork for employing NW resonators as scanning probes for NW-MFM. Specifically, we have investigated how to describe the magnetic imaging contrast formation following Hug and van Schendel [7, 8] and adapted their transfer function model to the case of NWs with magnetic tips in pendulum geometry. Equations (1.141) and (1.142) relate the measured frequency shifts of both modes to the stray field in two-dimensional Fourier space and allow for a quantitative interpretation of the stray field once the tip equivalent magnetic surface charge $\sigma^*_{\mathrm{tip}}(\mathbf{k})$ is fully characterized. This calibration requires measurements of a known stray field e.g. to empirically extract the form of $\sigma^*_{\mathrm{tip}}(\mathbf{k})$ as demonstrated by Hug and van Schendel on perpendicularly magnetized thin films [7, 8]. The approach we took in this work is to assume a point-pole model and using the Biot-Savart field of a known current flowing through a microwire to calibrate the tip parameters [12, 13, 72, 92, 93]. The advantage of this method is an easy implementation and the interpretation of the tip type (monopole- or dipole-like). However, it usually falls short of capturing a sufficient variety of spatial frequencies to fully characterize $\sigma^*_{\mathrm{tip}}(\mathbf{k})$ across the experimentally relevant region of $\mathbf{k}$. Furthermore, we summarized the theoretical thermally limited sensitivity of monopole and dipole tips to magnetic fields at resonance and in DC (Table 1.1)

The second chapter introduced the measurement apparatus and addressed a few recent additions such as a heater stage which can be used to control the sample temperature in the range of 5 to 50 K. We also swapped out polarization-maintaining optical fibers and objective for more robust single mode fibers and implemented porlarization control via paddle-polarizers at the laser outputs. This allows us to routinely work at fringe visibilities close to one with the Si NWs presented in Section 3.1. A major update included the addition of an optical driving laser at a spectrally separated wavelength from the readout laser. We assessed its performance and found a way better stability as compared to piezoelectric or capacitive actuation methods. The driving mechanism is most likely photothermal and will result in a small amount of heating of the NW resonator leading to a universal down shift of both modes that is not interfering with any scanning probe measurements.

The third chapter covers two NW probes that have been studied. The first part focuses on fully magnetic Co NWs grown by FEBID [13]. We found that they obey the monopole tip model with a magnetic surface charge of $q_{\mathrm{tip}} = 9.7(4)\times10^{-9}\,\mathrm{A\,m}$, ultimately achieving a sensitivity to magnetic field of $B_{\mathrm{min}} = 3\,\mathrm{nT}/\sqrt{\mathrm{Hz}}$. We also demonstrated a first example of magnetic imaging on permalloy disks. The second part presents the

combination of a Co FEBID tip and a state of the art Si NW in terms of force sensitivity [16] with the aim to retain a monopole tip and exploiting the excellent mechanical properties. This was partly achieved. Due to the deposition process the quality factor declined to about one third and the tip monopole is a factor of 3-4 smaller than in the full FEBID case, due to different deposition parameters and the peculiar geometric shape of the tip deposit. Nonetheless, the thermally limited field sensitivity turns out to be around $B_{\min} = 2.4\,\mathrm{nT}/\sqrt{\mathrm{Hz}}$ (at 250 nm tip-sample distance) in the same range of the full Co FEBID NWs.

At the end of the day we presented a versatile NW-MFM platform operating at room- and cryogenic temperatures with access to a wide range of sample temperatures at cryogenic operation. A large advantage compared to other ultra-sensitive magnetic scanning probe techniques such as scanning-SQUID or NV-center magnetometry is the de facto almost unlimited range of applicable external fields (in our system up to 8 T) and the robustness of operation[1]. On the other hand NW-MFM is slightly invasive to the sample scanned and features some geometrical constraints on sample geometry, mainly the necessity for it to be located at the chip edge. However, the presence of a tip stray field might even pave the way to highly interesting studies of magnetic dissipation effects and local magnetic susceptibility measurements in 2D-magnets e.g. revealing domain wall oscillations [103, 185].

4.2. Outlook

In general our NW-MFM platform is already well developed and enables nano-scale magnetic imaging with intriguing sensitivity and spatial resolution for a wide range of experimental parameters. A few aspects can be improved further:

Full Co FEBID NWs The full Co FEBID probes are a versatile probe with a surprisingly good field sensitivity. They suffer from heating effects, which result in a higher NW temperature loosing out on roughly a factor of two to three in sensitivity. A second property that could probably be improved is the quality factor with changes in the growth process and a possible annealing step.

Si NWs The Si NWs are a very stable platform to functionalize with a magnetic tip. Possible improvements are clearly retaining the high original quality factor of around 60 000 and a tip deposit that follows a thin cylindrical shape more closely. Additionally, a higher Co content can possibly be achieved pushing q_{tip} to a value similar to the full Co FEBID NWs. Assuming all values line up perfectly the expected thermally limited field sensitivity turns out to be an unprecedented value of[2] $B_{\min} \approx 200\,\mathrm{pT}/\sqrt{\mathrm{Hz}}$.

Other NW probes Possible other materials for very high mechanical quality NW resonators are GaN (quality factors of up to 400 000 at 17 K [122]) or SiC [35]. Interesting candidates are also hollow tubes out of aluminum oxide [186] or CNTs

[1] A single NW probe can be used for years and even survives soft crashes unscathed.
[2] $Q = 60\,000$, $q_{\mathrm{tip}} = 9 \times 10^{-9}\,\mathrm{A\,m}$ and $T_{\mathrm{NW}} = 4.5\,\mathrm{K}$.

[121], greatly improving the force sensitivity due to their low mass. Additionally it would be a great advantage to work with a conductive tip in order to mitigate the effects of electrostatic interactions.

Tip magnets Depending on the specific application a different material for the tip could be deposited or attached with a micromanipulator. Cobalt might not be the ideal material at high fields since it seems to increase natural dissipation at least when evaporated on a cantilever (see [168]). Co FEBID is also limited in the diameters that can be achieved on the lower end and the Co content tends to decrease for thinner deposits. In general for imaging purposes a hard magnet with a high saturation magnetization and a strong anisotropy along the external field axis is best suited for imaging.

Tip calibration The tip calibration procedure could greatly benefit from a calibration sample with a variety of spatial frequencies such as a multilayer thin-film or similar. With that an empirical form of $\sigma_{\mathrm{tip}}(\mathbf{k})$ can be calculated analog to Hug and van Schendel [7, 8].

Apparatus A major improvement to the NW apparatus would be to reiterate on the thermal management and lower the base temperature at high vacuum (without exchange gas) to LHe temperature by redesigning the thermal clamping points. Additionally, changes in material of the sample holder to a thermally more insulating material than titanium would make even higher sample temperatures accessible with a penalty on cooling rate.

AC/current density imaging The full advantage of eventually sub-nano tesla sensitivity at the resonance frequency of the NW sensor could be exploited to image very subtle current densities or gate tunable magnetism [187, 188], under the condition that the contact impedance of a given sample allows for modulation of the device current or electron density at a few hundred kHz.

Finally we are looking forward to explore the realm of 2D-magnets with nanometer scale resolution within the field and temperature range indicated above.

Bibliography

[1]G. Binnig, C. F. Quate, and C. Gerber, "Atomic force microscope", Physical Review Letters **56**, 930–933 (1986).

[2]G. Binnig, H. Rohrer, C. Gerber, and E. Weibel, "Surface studies by scanning tunneling microscopy", Physical Review Letters **49**, 57–61 (1982).

[3]Y. Martin and H. K. Wickramasinghe, "Magnetic imaging by "force microscopy" with 1000 å resolution", Applied Physics Letters **50**, 1455–1457 (1987).

[4]A. Wadas and P. Grütter, "Theoretical approach to magnetic force microscopy", Physical Review B **39**, 12013–12017 (1989).

[5]C. Schönenberger and S. F. Alvarado, "Understanding magnetic force microscopy", Zeitschrift für Physik B Condensed Matter **80**, 373–383 (1990).

[6]A. Wadas and H. J. Hug, "Models for the stray field from magnetic tips used in magnetic force microscopy", Journal of Applied Physics **72**, 203–206 (1992).

[7]H. J. Hug, B. Stiefel, P. J. A. v. Schendel, A. Moser, R. Hofer, S. Martin, H.-J. Güntherodt, S. Porthun, L. Abelmann, J. C. Lodder, G. Bochi, and R. C. O'Handley, "Quantitative magnetic force microscopy on perpendicularly magnetized samples", Journal of Applied Physics **83**, 5609–5620 (1998).

[8]P. J. A. v. Schendel, H. J. Hug, B. Stiefel, S. Martin, and H.-J. Güntherodt, "A method for the calibration of magnetic force microscopy tips", Journal of Applied Physics **88**, 435–445 (2000).

[9]Y. Feng, A.-O. Mandru, O. Yıldırım, and H. Hug, "Quantitative magnetic force microscopy: transfer-function method revisited", Physical Review Applied **18**, 024016 (2022).

[10]Y. Feng, P. M. Vaghefi, S. Vranjkovic, M. Penedo, P. Kappenberger, J. Schwenk, X. Zhao, A. .-. Mandru, and H. J. Hug, "Magnetic force microscopy contrast formation and field sensitivity", Journal of Magnetism and Magnetic Materials **551**, 169073 (2022).

[11]N. Rossi, F. R. Braakman, D. Cadeddu, D. Vasyukov, G. Tütüncüoglu, A. Fontcuberta i Morral, and M. Poggio, "Vectorial scanning force microscopy using a nanowire sensor", Nature Nanotechnology **12**, 150–155 (2017).

[12]N. Rossi, B. Gross, F. Dirnberger, D. Bougeard, and M. Poggio, "Magnetic force sensing using a self-assembled nanowire", Nano Letters **19**, 930–936 (2019).

[13]H. Mattiat, N. Rossi, B. Gross, J. Pablo-Navarro, C. Magén, R. Badea, J. Berezovsky, J. M. De Teresa, and M. Poggio, "Nanowire magnetic force sensors fabricated by focused-electron-beam-induced deposition", Physical Review Applied **13**, 044043 (2020).

[14]D. Vasyukov, Y. Anahory, L. Embon, D. Halbertal, J. Cuppens, L. Neeman, A. Finkler, Y. Segev, Y. Myasoedov, M. L. Rappaport, M. E. Huber, and E. Zeldov, "A scanning superconducting quantum interference device with single electron spin sensitivity", Nature Nanotechnology **8**, 639–644 (2013).

[15]E. Marchiori, L. Ceccarelli, N. Rossi, L. Lorenzelli, C. L. Degen, and M. Poggio, "Nanoscale magnetic field imaging for 2d materials", Nature Reviews Physics **4**, 49–60 (2022).

[16]P. Sahafi, W. Rose, A. Jordan, B. Yager, M. Piscitelli, and R. Budakian, "Ultralow dissipation patterned silicon nanowire arrays for scanning probe microscopy", Nano Letters **20**, 218–223 (2020).

[17]S. S. Rao, "Derivation of equations: variational approach", in *Vibration of continuous systems* (John Wiley & Sons, Ltd, 2019), pp. 87–124.

[18]S. Schmid, L. G. Villanueva, and M. L. Roukes, *Fundamentals of nanomechanical resonators* (Springer International Publishing, 2016).

[19]S. S. Rao, *Vibration of continuous systems* (John Wiley & Sons, Inc., Hoboken, NJ, USA, Mar. 6, 2019).

[20]S. S. Rao, "Transverse vibration of beams", in *Vibration of continuous systems* (John Wiley & Sons, Ltd, 2019), pp. 323–398.

[21]N. Rossi, "Force sensing with nanowires", Thesis (University of Basel, Basel, Switzerland, 2019), 136 Seiten.

[22]L. Meirovitch, *Fundamentals of vibrations*, McGraw-Hill International Edition, Mechanical Engineering Series (McGraw-Hill, Singapore, 2001).

[23]B. D. Hauer, C. Doolin, K. S. D. Beach, and J. P. Davis, "A general procedure for thermomechanical calibration of nano/micro-mechanical resonators", Annals of Physics **339**, 181–207 (2013).

[24]M. V. Salapaka, H. S. Bergh, J. Lai, A. Majumdar, and E. McFarland, "Multi-mode noise analysis of cantilevers for scanning probe microscopy", Journal of Applied Physics **81**, 2480–2487 (1997).

[25]A. N. Cleland, *Foundations of nanomechanics from solid-state theory to device applications* (Springer Berlin Heidelberg, Berlin, Heidelberg, 2003).

[26]A. N. Cleland and M. L. Roukes, "Noise processes in nanomechanical resonators", Journal of Applied Physics **92**, 2758–2769 (2002).

[27]A. Volodin and C. Van Haesendonck, "Low temperature force microscopy based on piezoresistive cantilevers operating at a higher flexural mode", Applied Physics A **66**, S305–S308 (1998).

[28]J. Yang, T. Ono, and M. Esashi, "Mechanical behavior of ultrathin microcantilever", Sensors and Actuators A: Physical **82**, 102–107 (2000).

[29]T. Ikehara, J. Lu, M. Konno, R. Maeda, and T. Mihara, "A high quality-factor silicon cantilever for a low detection-limit resonant mass sensor operated in air", Journal of Micromechanics and Microengineering **17**, 2491 (2007).

[30]Q. P. Unterreithmeier, T. Faust, and J. P. Kotthaus, "Damping of nanomechanical resonators", Physical Review Letters **105**, 027205 (2010).

[31]K. Yasumura, T. Stowe, E. Chow, T. Pfafman, T. Kenny, B. Stipe, and D. Rugar, "Quality factors in micron- and submicron-thick cantilevers", Journal of Microelectromechanical Systems **9**, 117–125 (2000).

[32]M. Imboden and P. Mohanty, "Dissipation in nanoelectromechanical systems", Physics Reports, Dissipation in nano-electromechanical systems **534**, 89–146 (2014).

[33]J. Yang, T. Ono, and M. Esashi, "Surface effects and high quality factors in ultrathin single-crystal silicon cantilevers", Applied Physics Letters **77**, 3860–3862 (2000).

[34]J. M. Nichol, E. R. Hemesath, L. J. Lauhon, and R. Budakian, "Displacement detection of silicon nanowires by polarization-enhanced fiber-optic interferometry", Applied Physics Letters **93**, 193110 (2008).

[35]F. Fogliano, B. Besga, A. Reigue, L. Mercier de Lépinay, P. Heringlake, C. Gouriou, E. Eyraud, W. Wernsdorfer, B. Pigeau, and O. Arcizet, "Ultrasensitive nano-optomechanical force sensor operated at dilution temperatures", Nature Communications **12**, 4124 (2021).

[36]F. R. Blom, S. Bouwstra, M. Elwenspoek, and J. H. J. Fluitman, "Dependence of the quality factor of micromachined silicon beam resonators on pressure and geometry", Journal of Vacuum Science & Technology B: Microelectronics and Nanometer Structures Processing, Measurement, and Phenomena **10**, 19–26 (1992).

[37]M. Nonnenmacher, J. Greschner, O. Wolter, and R. Kassing, "Scanning force microscopy with micromachined silicon sensors", Journal of Vacuum Science & Technology B: Microelectronics and Nanometer Structures Processing, Measurement, and Phenomena **9**, 1358–1362 (1991).

[38]P. Coleman, "Fluctuation–dissipation theorem and linear response theory", in *Introduction to many-body physics* (Cambridge University Press, Cambridge, 2015), pp. 292–331.

[39]M. C. Wang and G. E. Uhlenbeck, "On the theory of the brownian motion II", Reviews of Modern Physics **17**, 323–342 (1945).

[40]H. B. Callen and T. A. Welton, "Irreversibility and generalized noise", Physical Review **83**, 34–40 (1951).

[41]R. Kubo, "The fluctuation-dissipation theorem", Reports on Progress in Physics **29**, 255 (1966).

[42]D. Cadeddu, F. R. Braakman, G. Tütüncüoglu, F. Matteini, D. Rüffer, A. Fontcuberta i Morral, and M. Poggio, "Time-resolved nonlinear coupling between orthogonal flexural modes of a pristine GaAs nanowire", Nano Letters **16**, 926–931 (2016).

[43]F. R. Braakman, N. Rossi, G. Tütüncüoglu, A. F. i. Morral, and M. Poggio, "Coherent two-mode dynamics of a nanowire force sensor", Physical Review Applied **9**, 054045 (2018).

[44]A. P. Foster, J. K. Maguire, J. P. Bradley, T. P. Lyons, A. B. Krysa, A. M. Fox, M. S. Skolnick, and L. R. Wilson, "Tuning nonlinear mechanical mode coupling in GaAs nanowires using cross-section morphology control", Nano Letters, `10.1021/acs.nanolett.6b02994` (2016).

[45]S. Perisanu, T. Barois, A. Ayari, P. Poncharal, M. Choueib, S. T. Purcell, and P. Vincent, "Beyond the linear and duffing regimes in nanomechanics: circularly polarized mechanical resonances of nanocantilevers", Physical Review B **81**, 165440 (2010).

[46]L. M. de Lépinay, B. Pigeau, B. Besga, P. Vincent, P. Poncharal, and O. Arcizet, "A universal and ultrasensitive vectorial nanomechanical sensor for imaging 2d force fields", Nature Nanotechnology **12**, 156–162 (2017).

[47]E. Gil-Santos, D. Ramos, J. Martínez, M. Fernández-Regúlez, R. García, Á. San Paulo, M. Calleja, and J. Tamayo, "Nanomechanical mass sensing and stiffness spectrometry based on two-dimensional vibrations of resonant nanowires", Nature Nanotechnology **5**, 641–645 (2010).

[48]A. Gloppe, P. Verlot, E. Dupont-Ferrier, A. Siria, P. Poncharal, G. Bachelier, P. Vincent, and O. Arcizet, "Bidimensional nano-optomechanics and topological backaction in a non-conservative radiation force field", Nature Nanotechnology **9**, 920–926 (2014).

[49]A. Tavernarakis, A. Stavrinadis, A. Nowak, I. Tsioutsios, A. Bachtold, and P. Verlot, "Optomechanics with a hybrid carbon nanotube resonator", Nature Communications **9**, 662 (2018).

[50]O. Malvar, E. Gil-Santos, J. J. Ruz, D. Ramos, V. Pini, M. Fernandez-Regulez, M. Calleja, J. Tamayo, and A. San Paulo, "Tapered silicon nanowires for enhanced nanomechanical sensing", Applied Physics Letters **103**, 033101 (2013).

[51]I. Tsioutsios, A. Tavernarakis, J. Osmond, P. Verlot, and A. Bachtold, "Real-time measurement of nanotube resonator fluctuations in an electron microscope", Nano Letters **17**, 1748–1755 (2017).

[52]F. R. Braakman and M. Poggio, "Force sensing with nanowire cantilevers", Nanotechnology **30**, 332001 (2019).

[53]J. J. Sáenz, N. García, P. Grütter, E. Meyer, H. Heinzelmann, R. Wiesendanger, L. Rosenthaler, H. R. Hidber, and H.-J. Güntherodt, "Observation of magnetic forces by the atomic force microscope", Journal of Applied Physics **62**, 4293–4295 (1987).

[54]Y. Martin, D. Rugar, and H. K. Wickramasinghe, "High-resolution magnetic imaging of domains in TbFe by force microscopy", Applied Physics Letters **52**, 244–246 (1988).

[55]D. W. Abraham, C. C. Williams, and H. K. Wickramasinghe, "Measurement of in-plane magnetization by force microscopy", Applied Physics Letters **53**, 1446–1448 (1988).

[56]H. J. Mamin, D. Rugar, J. E. Stern, B. D. Terris, and S. E. Lambert, "Force microscopy of magnetization patterns in longitudinal recording media", Applied Physics Letters **53**, 1563–1565 (1988).

[57]P. Grütter, E. Meyer, H. Heinzelmann, L. Rosenthaler, H.-R. Hidber, and H.-J. Güntherodt, "Application of atomic force microscopy to magnetic materials", Journal of Vacuum Science & Technology A **6**, 279–282 (1988).

[58]D. Rugar, H. J. Mamin, R. Erlandsson, J. E. Stern, and B. D. Terris, "Force microscope using a fiber-optic displacement sensor", Review of Scientific Instruments **59**, 2337–2340 (1988).

[59]D. Rugar, H. J. Mamin, P. Guethner, S. E. Lambert, J. E. Stern, I. McFadyen, and T. Yogi, "Magnetic force microscopy: general principles and application to longitudinal recording media", Journal of Applied Physics **68**, 1169–1183 (1990).

[60]A. J. den Boef, "Preparation of magnetic tips for a scanning force microscope", Applied Physics Letters **56**, 2045–2047 (1990).

[61]P. Grütter, D. Rugar, H. J. Mamin, G. Castillo, S. E. Lambert, C.-J. Lin, R. M. Valletta, O. Wolter, T. Bayer, and J. Greschner, "Batch fabricated sensors for magnetic force microscopy", Applied Physics Letters **57**, 1820–1822 (1990).

[62]N. Amos, R. Ikkawi, R. Haddon, D. Litvinov, and S. Khizroev, "Controlling multidomain states to enable sub-10-nm magnetic force microscopy", Applied Physics Letters **93**, 203116 (2008).

[63]E. Meyer, R. Bennewitz, and H. J. Hug, "Magnetic force microscopy", in *Scanning probe microscopy: the lab on a tip*, edited by E. Meyer, R. Bennewitz, and H. J. Hug, Graduate Texts in Physics (Springer International Publishing, Cham, 2021), pp. 109–211.

[64]P. B. Fischer, M. S. Wei, and S. Y. Chou, "Ultrahigh resolution magnetic force microscope tip fabricated using electron beam lithography", Journal of Vacuum Science & Technology B: Microelectronics and Nanometer Structures Processing, Measurement, and Phenomena **11**, 2570–2573 (1993).

[65]I. Utke, P. Hoffmann, R. Berger, and L. Scandella, "High-resolution magnetic co supertips grown by a focused electron beam", Applied Physics Letters **80**, 4792–4794 (2002).

[66]L. M. Belova, O. Hellwig, E. Dobisz, and E. Dan Dahlberg, "Rapid preparation of electron beam induced deposition co magnetic force microscopy tips with 10 nm spatial resolution", Review of Scientific Instruments **83**, 093711 (2012).

[67]M. Jaafar, J. Pablo-Navarro, E. Berganza, P. Ares, C. Magén, A. Masseboeuf, C. Gatel, E. Snoeck, J. Gómez-Herrero, J. M. d. Teresa, and A. Asenjo, "Customized MFM probes based on magnetic nanorods", Nanoscale **12**, 10090–10097 (2020).

[68]M. Stiller, J. Barzola-Quiquia, P. D. Esquinazi, S. Sangiao, J. M. D. Teresa, J. Meijer, and B. Abel, "Functionalized akiyama tips for magnetic force microscopy measurements", Measurement Science and Technology **28**, 125401 (2017).

[69]Z. Deng, E. Yenilmez, J. Leu, J. E. Hoffman, E. W. J. Straver, H. Dai, and K. A. Moler, "Metal-coated carbon nanotube tips for magnetic force microscopy", Applied Physics Letters **85**, 6263–6265 (2004).

[70]H. Kuramochi, T. Uzumaki, M. Yasutake, A. Tanaka, H. Akinaga, and H. Yokoyama, "A magnetic force microscope using CoFe-coated carbon nanotube probes", Nanotechnology **16**, 24 (2004).

[71]Y. Lisunova, J. Heidler, I. Levkivskyi, I. Gaponenko, A. Weber, C. Caillier, L. J. Heyderman, M. Kläui, and P. Paruch, "Optimal ferromagnetically-coated carbon nanotube tips for ultra-high resolution magnetic force microscopy", Nanotechnology **24**, 105705 (2013).

[72]F. Wolny, T. Mühl, U. Weissker, K. Lipert, J. Schumann, A. Leonhardt, and B. Büchner, "Iron filled carbon nanotubes as novel monopole-like sensors for quantitative magnetic force microscopy", Nanotechnology **21**, 435501 (2010).

[73]S. Vock, F. Wolny, T. Mühl, R. Kaltofen, L. Schultz, B. Büchner, C. Hassel, J. Lindner, and V. Neu, "Monopolelike probes for quantitative magnetic force microscopy: calibration and application", Applied Physics Letters **97**, 252505 (2010).

[74]C. F. Reiche, S. Vock, V. Neu, L. Schultz, B. Büchner, and T. Mühl, "Bidirectional quantitative force gradient microscopy", New Journal of Physics **17**, 013014 (2015).

[75]F. Wolny, Y. Obukhov, T. Mühl, U. Weißker, S. Philippi, A. Leonhardt, P. Banerjee, A. Reed, G. Xiang, R. Adur, I. Lee, A. J. Hauser, F. Y. Yang, D. V. Pelekhov, B. Büchner, and P. C. Hammel, "Quantitative magnetic force microscopy on permalloy dots using an iron filled carbon nanotube probe", Ultramicroscopy **111**, 1360–1365 (2011).

[76]N. H. Freitag, C. F. Reiche, V. Neu, P. Devi, U. Burkhardt, C. Felser, D. Wolf, A. Lubk, B. Büchner, and T. Mühl, "Simultaneous magnetic field and field gradient mapping of hexagonal MnNiGa by quantitative magnetic force microscopy", Communications Physics **6**, 1–13 (2023).

[77]O. Kazakova, R. Puttock, C. Barton, H. Corte-León, M. Jaafar, V. Neu, and A. Asenjo, "Frontiers of magnetic force microscopy", Journal of Applied Physics **125**, 060901 (2019).

[78]S. L. Tomlinson and E. W. Hill, "Modelling the perturbative effect of MFM tips on soft magnetic thin films", Journal of Magnetism and Magnetic Materials **161**, 385–396 (1996).

[79]J. M. D. Coey, *Magnetism and magnetic materials* (Cambridge University Press, Cambridge, 2010).

[80]E. A. Lima and B. P. Weiss, "Obtaining vector magnetic field maps from single-component measurements of geological samples", Journal of Geophysical Research: Solid Earth **114**, B06102 (2009).

[81]T. van der Sar, F. Casola, R. Walsworth, and A. Yacoby, "Nanometre-scale probing of spin waves using single electron spins", Nature Communications **6**, 7886 (2015).

[82]Y. Dovzhenko, F. Casola, S. Schlotter, T. X. Zhou, F. Büttner, R. L. Walsworth, G. S. D. Beach, and A. Yacoby, "Magnetostatic twists in room-temperature skyrmions explored by nitrogen-vacancy center spin texture reconstruction", Nature Communications **9**, 2712 (2018).

[83]F. Casola, T. van der Sar, and A. Yacoby, "Probing condensed matter physics with magnetometry based on nitrogen-vacancy centres in diamond", Nature Reviews Materials **3**, 1–13 (2018).

[84]D. Broadway, S. Lillie, S. Scholten, D. Rohner, N. Dontschuk, P. Maletinsky, J.-P. Tetienne, and L. Hollenberg, "Improved current density and magnetization reconstruction through vector magnetic field measurements", Physical Review Applied **14**, 024076 (2020).

[85]S. Tan, Y. P. Ma, I. Thomas, and J. Wikswo, "Reconstruction of two-dimensional magnetization and susceptibility distributions from the magnetic field of soft magnetic materials", IEEE Transactions on Magnetics **32**, 230–234 (1996).

[86]S. Dreyer, J. Norpoth, C. Jooss, S. Sievers, U. Siegner, V. Neu, and T. H. Johansen, "Quantitative imaging of stray fields and magnetization distributions in hard magnetic element arrays", Journal of Applied Physics **101**, 083905 (2007).

[87]U. Hartmann, "The point dipole approximation in magnetic force microscopy", Physics Letters A **137**, 475–478 (1989).

[88]S. L. Tomlinson and A. N. Farley, "Micromagnetic model for magnetic force microscopy tips", Journal of Applied Physics **81**, 5029–5031 (1997).

[89]E. Hill, "Modelling damaged MFM tips using triangular charge sheets", IEEE Transactions on Magnetics **31**, 3355–3357 (1995).

[90]E. Meyer, R. Bennewitz, and H. J. Hug, "Force microscopy", in *Scanning probe microscopy: the lab on a tip*, edited by E. Meyer, R. Bennewitz, and H. J. Hug, Graduate Texts in Physics (Springer International Publishing, Cham, 2021), pp. 47–107.

[91]S. McVitie, R. P. Ferrier, J. Scott, G. S. White, and A. Gallagher, "Quantitative field measurements from magnetic force microscope tips and comparison with point and extended charge models", Journal of Applied Physics **89**, 3656–3661 (2001).

[92]J. Lohau, S. Kirsch, A. Carl, G. Dumpich, and E. F. Wassermann, "Quantitative determination of effective dipole and monopole moments of magnetic force microscopy tips", Journal of Applied Physics **86**, 3410–3417 (1999).

[93]T. Kebe and A. Carl, "Calibration of magnetic force microscopy tips by using nanoscale current-carrying parallel wires", Journal of Applied Physics **95**, 775–792 (2004).

[94]T. Göddenhenrich, H. Lemke, M. Mück, U. Hartmann, and C. Heiden, "Probe calibration in magnetic force microscopy", Applied Physics Letters **57**, 2612–2614 (1990).

[95]L. Kong and S. Y. Chou, "Quantification of magnetic force microscopy using a micronscale current ring", Applied Physics Letters **70**, 2043–2045 (1997).

[96]M. R. Koblischka, U. Hartmann, and T. Sulzbach, "Improving the lateral resolution of the MFM technique to the 10nm range", Journal of Magnetism and Magnetic Materials, Proceedings of the International Conference on Magnetism (ICM 2003) **272-276**, 2138–2140 (2004).

[97]J. Šoltýs, J. Feilhauer, I. Vetrova, J. Tóbik, K. Bublikov, T. Ščepka, J. Fedor, J. Dérer, and V. Cambel, "Magnetic-field imaging using vortex-core MFM tip", Applied Physics Letters **116**, 242406 (2020).

[98]S. Hosaka, A. Kikukawa, Y. Honda, H. K. H. Koyanagi, and S. T. S. Tanaka, "Simultaneous observation of 3-dimensional magnetic stray field and surface structure using new force microscope", Japanese Journal of Applied Physics **31**, L904 (1992).

[99]M. Jaafar, O. Iglesias-Freire, L. Serrano-Ramón, M. R. Ibarra, J. M. d. Teresa, and A. Asenjo, "Distinguishing magnetic and electrostatic interactions by a kelvin probe force microscopy–magnetic force microscopy combination", Beilstein Journal of Nanotechnology **2**, 552–560 (2011).

[100]L. Angeloni, D. Passeri, M. Reggente, D. Mantovani, and M. Rossi, "Removal of electrostatic artifacts in magnetic force microscopy by controlled magnetization of the tip: application to superparamagnetic nanoparticles", Scientific Reports **6**, 26293 (2016).

[101]C. Schönenberger, S. F. Alvarado, S. E. Lambert, and I. L. Sanders, "Separation of magnetic and topographic effects in force microscopy", Journal of Applied Physics **67**, 7278–7280 (1990).

[102]P. Grütter, Y. Liu, P. LeBlanc, and U. Dürig, "Magnetic dissipation force microscopy", Applied Physics Letters **71**, 279–281 (1997).

[103]Y. Liu and P. Grütter, "Theory of magnetoelastic dissipation due to domain wall width oscillation", Journal of Applied Physics **83**, 5922–5926 (1998).

[104]A. Labuda, K. Kobayashi, D. Kiracofe, K. Suzuki, P. H. Grütter, and H. Yamada, "Comparison of photothermal and piezoacoustic excitation methods for frequency and phase modulation atomic force microscopy in liquid environments", AIP Advances **1**, 022136 (2011).

[105]A. Labuda, Y. Miyahara, L. Cockins, and P. H. Grütter, "Decoupling conservative and dissipative forces in frequency modulation atomic force microscopy", Physical Review B **84**, 125433 (2011).

[106]M. Tortonese, R. C. Barrett, and C. F. Quate, "Atomic resolution with an atomic force microscope using piezoresistive detection", Applied Physics Letters **62**, 834–836 (1993).

[107]K. Karraï and R. D. Grober, "Piezo-electric tuning fork tip—sample distance control for near field optical microscopes", Ultramicroscopy, Selected Papers from the 3rd International Conference on Near-Field Optics and Related Techniques **61**, 197–205 (1995).

[108]F. J. Giessibl, "Advances in atomic force microscopy", Reviews of Modern Physics **75**, 949–983 (2003).

[109]F. J. Giessibl, "High-speed force sensor for force microscopy and profilometry utilizing a quartz tuning fork", Applied Physics Letters **73**, 3956–3958 (1998).

[110]G. Meyer and N. M. Amer, "Novel optical approach to atomic force microscopy", Applied Physics Letters **53**, 1045–1047 (1988).

[111]R. Erlandsson, G. M. McClelland, C. M. Mate, and S. Chiang, "Atomic force microscopy using optical interferometry", Journal of Vacuum Science & Technology A **6**, 266–270 (1988).

[112]D. Rugar, "Improved fiber-optic interferometer for atomic force microscopy", Applied Physics Letters **55**, 2588–2590 (1989).

[113]C. A. Regal, J. D. Teufel, and K. W. Lehnert, "Measuring nanomechanical motion with a microwave cavity interferometer", Nature Physics **4**, 555–560 (2008).

[114]J. Moser, J. Güttinger, A. Eichler, M. J. Esplandiu, D. E. Liu, M. I. Dykman, and A. Bachtold, "Ultrasensitive force detection with a nanotube mechanical resonator", Nature Nanotechnology **8**, 493–496 (2013).

[115]V. Sazonova, Y. Yaish, H. Üstünel, D. Roundy, T. A. Arias, and P. L. McEuen, "A tunable carbon nanotube electromechanical oscillator", Nature **431**, 284–287 (2004).

[116]S. Etaki, M. Poot, I. Mahboob, K. Onomitsu, H. Yamaguchi, and H. S. J. van der Zant, "Motion detection of a micromechanical resonator embedded in a d.c. SQUID", Nature Physics **4**, 785–788 (2008).

[117]D. Garcia-Sanchez, A. San Paulo, M. J. Esplandiu, F. Perez-Murano, L. Forró, A. Aguasca, and A. Bachtold, "Mechanical detection of carbon nanotube resonator vibrations", Physical Review Letters **99**, 085501 (2007).

[118]Y. Tsaturyan, A. Barg, E. S. Polzik, and A. Schliesser, "Ultracoherent nanomechanical resonators via soft clamping and dissipation dilution", Nature Nanotechnology **12**, 776–783 (2017).

[119]D. Hälg, T. Gisler, Y. Tsaturyan, L. Catalini, U. Grob, M.-D. Krass, M. Héritier, H. Mattiat, A.-K. Thamm, R. Schirhagl, E. C. Langman, A. Schliesser, C. L. Degen, and A. Eichler, "Membrane-based scanning force microscopy", Physical Review Applied **15**, L021001 (2021).

[120]A. Niguès, A. Siria, and P. Verlot, "Dynamical backaction cooling with free electrons", Nature Communications **6**, 8104 (2015).

[121]G. Gruber, C. Urgell, A. Tavernarakis, A. Stavrinadis, S. Tepsic, C. Magén, S. Sangiao, J. M. de Teresa, P. Verlot, and A. Bachtold, "Mass sensing for the advanced fabrication of nanomechanical resonators", Nano Letters **19**, 6987–6992 (2019).

[122]J. R. Montague, K. A. Bertness, N. A. Sanford, V. M. Bright, and C. T. Rogers, "Temperature-dependent mechanical-resonance frequencies and damping in ensembles of gallium nitride nanowires", Applied Physics Letters **101**, 173101 (2012).

[123]B. Sanii and P. D. Ashby, "High sensitivity deflection detection of nanowires", Physical Review Letters **104**, 147203 (2010).

[124]E. Gil-Santos, D. Ramos, V. Pini, J. Llorens, M. Fernández-Regúlez, M. Calleja, J. Tamayo, and A. S. Paulo, "Optical back-action in silicon nanowire resonators: bolometric versus radiation pressure effects", New Journal of Physics **15**, 035001 (2013).

[125]J. Molina, J. E. Escobar, D. Ramos, E. Gil-Santos, J. J. Ruz, J. Tamayo, Á. San Paulo, and M. Calleja, "High dynamic range nanowire resonators", Nano Letters **21**, 6617–6624 (2021).

[126]F. Fogliano, B. Besga, A. Reigue, P. Heringlake, L. Mercier de Lépinay, C. Vaneph, J. Reichel, B. Pigeau, and O. Arcizet, "Mapping the cavity optomechanical interaction with subwavelength-sized ultrasensitive nanomechanical force sensors", Physical Review X **11**, 021009 (2021).

[127]J. Doster, S. Hoenl, H. Lorenz, P. Paulitschke, and E. M. Weig, "Collective dynamics of strain-coupled nanomechanical pillar resonators", Nature Communications **10**, 5246 (2019).

[128]J. Molina, D. Ramos, E. Gil-Santos, J. E. Escobar, J. J. Ruz, J. Tamayo, Á. San Paulo, and M. Calleja, "Optical transduction for vertical nanowire resonators", Nano Letters **20**, 2359–2369 (2020).

[129]T. R. Albrecht, P. Grütter, D. Rugar, and D. P. E. Smith, "Low-temperature force microscope with all-fiber interferometer", Ultramicroscopy **42-44**, 1638–1646 (1992).

[130]A. Högele, S. Seidl, M. Kroner, K. Karrai, C. Schulhauser, O. Sqalli, J. Scrimgeour, and R. J. Warburton, "Fiber-based confocal microscope for cryogenic spectroscopy", Review of Scientific Instruments **79**, 023709 (2008).

[131]C. F. Bohren and D. R. Huffman, *Absorption and scattering of light by small particles*, 1st ed. (John Wiley & Sons, Ltd, 1998).

[132]L. Novotny and B. Hecht, "Propagation and focusing of optical fields", in *Principles of nano-optics* (Cambridge University Press, Sept. 2012), pp. 45–85.

[133]E. Hecht, "Kapitel 9: Interferenz", in *Optik* (De Gruyter, Mar. 19, 2018), pp. 761–874.

[134]F. L. Degertekin, B. Hadimioglu, T. Sulchek, and C. F. Quate, "Actuation and characterization of atomic force microscope cantilevers in fluids by acoustic radiation pressure", Applied Physics Letters **78**, 1628–1630 (2001).

[135]H. Yamashita, N. Kodera, A. Miyagi, T. Uchihashi, D. Yamamoto, and T. Ando, "Tip-sample distance control using photothermal actuation of a small cantilever for high-speed atomic force microscopy", Review of Scientific Instruments **78**, 083702 (2007).

[136]D. Ramos, J. Tamayo, J. Mertens, and M. Calleja, "Photothermal excitation of microcantilevers in liquids", Journal of Applied Physics **99**, 124904 (2006).

[137]T. Fukuma, "Wideband low-noise optical beam deflection sensor with photothermal excitation for liquid-environment atomic force microscopy", Review of Scientific Instruments **80**, 023707 (2009).

[138]S. Nishida, D. Kobayashi, H. Kawakatsu, and Y. Nishimori, "Photothermal excitation of a single-crystalline silicon cantilever for higher vibration modes in liquid", Journal of Vacuum Science & Technology B: Microelectronics and Nanometer Structures Processing, Measurement, and Phenomena **27**, 964–968 (2009).

[139]V. Pini, B. Tiribilli, C. M. C. Gambi, and M. Vassalli, "Dynamical characterization of vibrating AFM cantilevers forced by photothermal excitation", Physical Review B **81**, 054302 (2010).

[140]M. Vassalli, V. Pini, and B. Tiribilli, "Role of the driving laser position on atomic force microscopy cantilevers excited by photothermal and radiation pressure effects", Applied Physics Letters **97**, 143105 (2010).

[141]X. Z. Yu, Y. Onose, N. Kanazawa, J. H. Park, J. H. Han, Y. Matsui, N. Nagaosa, and Y. Tokura, "Real-space observation of a two-dimensional skyrmion crystal", Nature **465**, 901–904 (2010).

[142]K. C. Nowack, E. M. Spanton, M. Baenninger, M. König, J. R. Kirtley, B. Kalisky, C. Ames, P. Leubner, C. Brüne, H. Buhmann, L. W. Molenkamp, D. Goldhaber-Gordon, and K. A. Moler, "Imaging currents in HgTe quantum wells in the quantum spin hall regime", Nature Materials **12**, 787–791 (2013).

[143]L. Thiel, Z. Wang, M. A. Tschudin, D. Rohner, I. Gutiérrez-Lezama, N. Ubrig, M. Gibertini, E. Giannini, A. F. Morpurgo, and P. Maletinsky, "Probing magnetism in 2d materials at the nanoscale with single-spin microscopy", Science **364**, 973–976 (2019).

[144]L. Embon, Y. Anahory, Ž. L. Jelić, E. O. Lachman, Y. Myasoedov, M. E. Huber, G. P. Mikitik, A. V. Silhanek, M. V. Milošević, A. Gurevich, and E. Zeldov, "Imaging of super-fast dynamics and flow instabilities of superconducting vortices", Nature Communications **8**, 85 (2017).

[145]A. Uri, Y. Kim, K. Bagani, C. K. Lewandowski, S. Grover, N. Auerbach, E. O. Lachman, Y. Myasoedov, T. Taniguchi, K. Watanabe, J. Smet, and E. Zeldov, "Nanoscale imaging of equilibrium quantum hall edge currents and of the magnetic monopole response in graphene", Nature Physics **16**, 164–170 (2020).

[146]C. W. Hicks, L. Luan, K. A. Moler, E. Zeldov, and H. Shtrikman, "Noise characteristics of 100nm scale GaAs/AlxGa1-xAs scanning hall probes", Applied Physics Letters **90**, 133512 (2007).

[147]P. Maletinsky, S. Hong, M. S. Grinolds, B. Hausmann, M. D. Lukin, R. L. Walsworth, M. Loncar, and A. Yacoby, "A robust scanning diamond sensor for nanoscale imaging with single nitrogen-vacancy centres", Nature Nanotechnology **7**, 320–324 (2012).

[148]S. J. Randolph, J. D. Fowlkes, and P. D. Rack, "Focused, nanoscale electron-beam-induced deposition and etching", Critical Reviews in Solid State and Materials Sciences **31**, 55–89 (2006).

[149]W. F. van Dorp and C. W. Hagen, "A critical literature review of focused electron beam induced deposition", Journal of Applied Physics **104**, 081301 (2008).

[150]I. Utke, P. Hoffmann, and J. Melngailis, "Gas-assisted focused electron beam and ion beam processing and fabrication", Journal of Vacuum Science & Technology B: Microelectronics and Nanometer Structures Processing, Measurement, and Phenomena **26**, 1197–1276 (2008).

[151]M. Huth, F. Porrati, C. Schwalb, M. Winhold, R. Sachser, M. Dukic, J. Adams, and G. Fantner, "Focused electron beam induced deposition: a perspective", Beilstein Journal of Nanotechnology **3**, 597–619 (2012).

[152]I. Utke, S. Moshkalev, and P. Russell, eds., *Nanofabrication using focused ion and electron beams: principles and applications* (Oxford University Press, Oxford, New York, May 24, 2012), 840 pp.

[153]T. J. Gannon, G. Gu, J. D. Casey, C. Huynh, N. Bassom, and N. Antoniou, "Focused ion beam induced deposition of low-resistivity copper material", Journal of Vacuum Science & Technology B: Microelectronics and Nanometer Structures Processing, Measurement, and Phenomena **22**, 3000–3003 (2004).

[154]H. Wu, L. A. Stern, D. Xia, D. Ferranti, B. Thompson, K. L. Klein, C. M. Gonzalez, and P. D. Rack, "Focused helium ion beam deposited low resistivity cobalt metal lines with 10 nm resolution: implications for advanced circuit editing", Journal of Materials Science: Materials in Electronics **25**, 587–595 (2014).

[155]J. M. D. Teresa, A. Fernández-Pacheco, R. Córdoba, L. Serrano-Ramón, S. Sangiao, and M. R. Ibarra, "Review of magnetic nanostructures grown by focused electron beam induced deposition (FEBID)", Journal of Physics D: Applied Physics **49**, 243003 (2016).

[156]E. S. Sadki, S. Ooi, and K. Hirata, "Focused-ion-beam-induced deposition of superconducting nanowires", Applied Physics Letters **85**, 6206–6208 (2004).

[157]M. Esposito, V. Tasco, M. Cuscunà, F. Todisco, A. Benedetti, I. Tarantini, M. D. Giorgi, D. Sanvitto, and A. Passaseo, "Nanoscale 3d chiral plasmonic helices with circular dichroism at visible frequencies", ACS Photonics **2**, 105–114 (2015).

[158]T. Bret, T. Hofmann, and K. Edinger, "Industrial perspective on focused electron beam-induced processes", Applied Physics A **117**, 1607–1614 (2014).

[159]L. A. Giannuzzi and F. A. Stevie, "A review of focused ion beam milling techniques for TEM specimen preparation", Micron **30**, 197–204 (1999).

[160]G. Nanda, E. van Veldhoven, D. Maas, H. Sadeghian, and P. F. A. Alkemade, "Helium ion beam induced growth of hammerhead AFM probes", Journal of Vacuum Science & Technology B **33**, 06F503 (2015).

[161]C. H. Schwalb, C. Grimm, M. Baranowski, R. Sachser, F. Porrati, H. Reith, P. Das, J. Müller, F. Völklein, A. Kaya, and M. Huth, "A tunable strain sensor using nanogranular metals", Sensors **10**, 9847–9856 (2010).

[162]R. Córdoba, A. Ibarra, D. Mailly, and J. M. De Teresa, "Vertical growth of superconducting crystalline hollow nanowires by he+ focused ion beam induced deposition", Nano Letters **18**, 1379–1386 (2018).

[163]J. Pablo-Navarro, D. Sanz-Hernández, C. Magén, A. Fernández-Pacheco, and J. M. d. Teresa, "Tuning shape, composition and magnetization of 3d cobalt nanowires grown by focused electron beam induced deposition (FEBID)", Journal of Physics D: Applied Physics **50**, 18LT01 (2017).

[164]B. Gross, D. P. Weber, D. Rüffer, A. Buchter, F. Heimbach, A. Fontcuberta i Morral, D. Grundler, and M. Poggio, "Dynamic cantilever magnetometry of individual CoFeB nanotubes", Physical Review B **93**, 064409 (2016).

[165]A. Vansteenkiste, J. Leliaert, M. Dvornik, M. Helsen, F. Garcia-Sanchez, and B. Van Waeyenberge, "The design and verification of MuMax3", AIP Advances **4**, 107133 (2014).

[166]L. Exl, S. Bance, F. Reichel, T. Schrefl, H. Peter Stimming, and N. J. Mauser, "LaBonte's method revisited: an effective steepest descent method for micromagnetic energy minimization", Journal of Applied Physics **115**, 17D118 (2014).

[167]A. Mehlin, B. Gross, M. Wyss, T. Schefer, G. Tütüncüoglu, F. Heimbach, A. Fontcuberta i Morral, D. Grundler, and M. Poggio, "Observation of end-vortex nucleation in individual ferromagnetic nanotubes", Physical Review B **97**, 134422 (2018).

[168]B. C. Stipe, H. J. Mamin, T. D. Stowe, T. W. Kenny, and D. Rugar, "Magnetic dissipation and fluctuations in individual nanomagnets measured by ultrasensitive cantilever magnetometry", Physical Review Letters **86**, 2874–2877 (2001).

[169]M. J. Martínez-Pérez, J. Pablo-Navarro, B. Müller, R. Kleiner, C. Magén, D. Koelle, J. M. de Teresa, and J. Sesé, "NanoSQUID magnetometry on individual as-grown and annealed co nanowires at variable temperature", Nano Letters **18**, 7674–7682 (2018).

[170]A. Mehlin, F. Xue, D. Liang, H. F. Du, M. J. Stolt, S. Jin, M. L. Tian, and M. Poggio, "Stabilized skyrmion phase detected in MnSi nanowires by dynamic cantilever magnetometry", Nano Letters **15**, 4839–4844 (2015).

[171]G. Shirane, V. J. Minkiewicz, and R. Nathans, "Spin waves in 3d metals", Journal of Applied Physics **39**, 383–390 (1968).

[172]S. P. Vernon, S. Lindsay, and M. B. Stearns, "Brillouin scattering from thermal magnons in a thin co film", Physical Review B **29**, 4439–4442 (1984).

[173]R. Krishnan, "FMR studies in compositionally modulated co-nb and co films", Journal of Magnetism and Magnetic Materials **50**, 189–192 (1985).

[174]X. Liu, M. M. Steiner, R. Sooryakumar, G. A. Prinz, R. F. C. Farrow, and G. Harp, "Exchange stiffness, magnetization, and spin waves in cubic and hexagonal phases of cobalt", Physical Review B **53**, 12166–12172 (1996).

[175]Y. Zhu, ed., *Modern techniques for characterizing magnetic materials* (Springer US, 2005).

[176]E. Berganza, M. Jaafar, J. A. Fernandez-Roldan, M. Goiriena-Goikoetxea, J. Pablo-Navarro, A. García-Arribas, K. Guslienko, C. Magén, J. M. D. Teresa, O. Chubykalo-Fesenko, and A. Asenjo, "Half-hedgehog spin textures in sub-100 nm soft magnetic nanodots", Nanoscale **12**, 18646–18653 (2020).

[177]M. Poggio and C. L. Degen, "Force-detected nuclear magnetic resonance: recent advances and future challenges", Nanotechnology **21**, 342001 (2010).

[178]R. Badea, J. A. Frey, and J. Berezovsky, "Magneto-optical imaging of vortex domain deformation in pinning sites", Journal of Magnetism and Magnetic Materials **381**, 463–469 (2015).

[179]U. Gysin, S. Rast, P. Ruff, E. Meyer, D. W. Lee, P. Vettiger, and C. Gerber, "Temperature dependence of the force sensitivity of silicon cantilevers", Physical Review B **69**, 045403 (2004).

[180]J. B. Wachtman, W. E. Tefft, D. G. Lam, and C. S. Apstein, "Exponential temperature dependence of young's modulus for several oxides", Physical Review **122**, 1754–1759 (1961).

[181]G. R. Stewart, "Measurement of low-temperature specific heat", Review of Scientific Instruments **54**, 1–11 (1983).

[182]A. Reiser, L. Koch, K. A. Dunn, T. Matsuura, F. Iwata, O. Fogel, Z. Kotler, N. Zhou, K. Charipar, A. Piqué, P. Rohner, D. Poulikakos, S. Lee, S. K. Seol, I. Utke, C. van Nisselroy, T. Zambelli, J. M. Wheeler, and R. Spolenak, "Metals by micro-scale additive manufacturing: comparison of microstructure and mechanical properties", Advanced Functional Materials **30**, 1910491 (2020).

[183]D. Zhang, J.-M. Breguet, R. Clavel, L. Philippe, I. Utke, and J. Michler, "In situ tensile testing of individual co nanowires inside a scanning electron microscope", Nanotechnology **20**, 365706 (2009).

[184]D. Halbertal, J. Cuppens, M. B. Shalom, L. Embon, N. Shadmi, Y. Anahory, H. R. Naren, J. Sarkar, A. Uri, Y. Ronen, Y. Myasoedov, L. S. Levitov, E. Joselevich, A. K. Geim, and E. Zeldov, "Nanoscale thermal imaging of dissipation in quantum systems", Nature **539**, 407–410 (2016).

[185]Y. Liu and P. Grütter, "Magnetic dissipation force microscopy studies of magnetic materials (invited)", Journal of Applied Physics **83**, 7333–7338 (1998).

[186]L. M. Vogl, P. Schweizer, L. Pethö, A. Sharma, J. Michler, and I. Utke, "From metal nanowires to ultrathin crystalline ALD nanotubes: process development and mechanism revealed by in situ TEM heating experiments", Nanoscale, `10.1039/D3NR01185B` (2023).

[187]Y. Deng, Y. Yu, Y. Song, J. Zhang, N. Z. Wang, Z. Sun, Y. Yi, Y. Z. Wu, S. Wu, J. Zhu, J. Wang, X. H. Chen, and Y. Zhang, "Gate-tunable room-temperature ferromagnetism in two-dimensional fe3gete2", Nature **563**, 94–99 (2018).

[188]Y. Lee, S. Che, J. J. Velasco, X. Gao, Y. Shi, D. Tran, J. Baima, F. Mauri, M. Calandra, M. Bockrath, and C. N. Lau, "Gate-tunable magnetism and giant magnetoresistance in suspended rhombohedral-stacked few-layer graphene", Nano Letters **22**, 5094–5099 (2022).

A. Microscope

A.1. Images

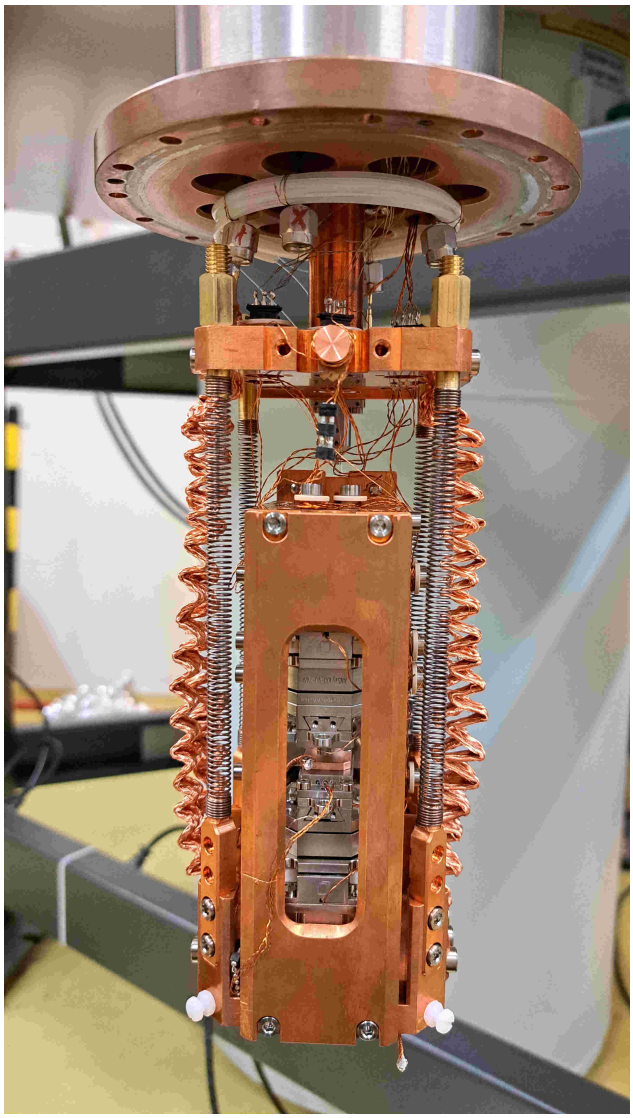

Figure A.1. – Front view of the NW scanning probe microscope

A.2. Acousto-Optic modulator

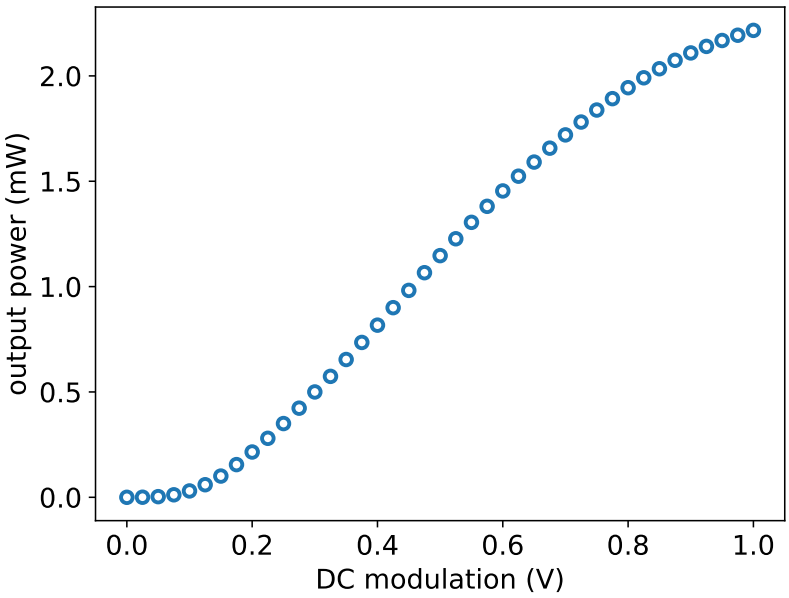

Figure A.2. – **AOM power output**
Output power of the AOM depending on the DC input voltage for an operating frequency of 10 MHz and an input power of 10 mW.

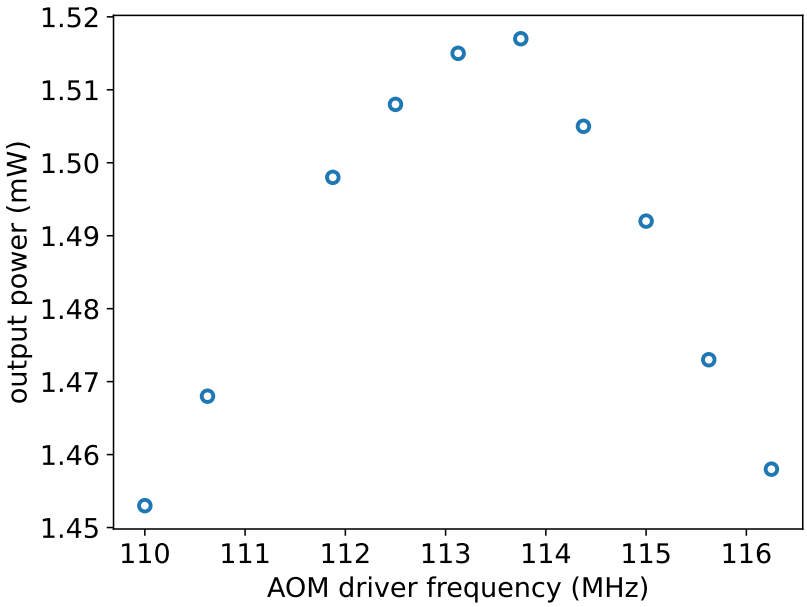

Figure A.3. – **AOM operating frequency**
Output power of the AOM depending on the operating frequency for an input power of 10 mW and a DC modulation of 0.6 V.

B. Mie scattering

Following section 8.4 of [131] the amplitude scattering matrix relating the incoming light to the scattered far field of a cylinder of radius R and infinite length L is given by

$$\begin{bmatrix} E_{\parallel s} \\ E_{\perp s} \end{bmatrix} = e^{i3\pi/4} \sqrt{\frac{2}{\pi k r \sin\zeta}}\; e^{ik(r\sin\zeta - z\cos\zeta)} \begin{bmatrix} T_1 & T_4 \\ T_3 & T_2 \end{bmatrix} \begin{bmatrix} E_{\parallel i} \\ E_{\perp i} \end{bmatrix} \tag{B.1}$$

where we have adopted the coordinate system shown Figure 8.3 of [131]. The cylinder is aligned with the z-axis and the incident light without loss of generality either polarized parallel (case I) or perpendicular (case II) to the xz-plane. ζ is the angle between the z-axis and the propagation direction of the incoming beam in the xz-plane ($\zeta = 90°$ corresponds to normal incidence). The incoming field is expressed as

$$\begin{gathered} \mathbf{E}_i = \left(E_{\parallel i}\hat{\mathbf{e}}_{\parallel i} + E_{\perp i}\hat{\mathbf{e}}_{\perp i}\right) e^{i\mathbf{k}\cdot\mathbf{x}}, \\ \hat{\mathbf{e}}_{\parallel i} = \sin\zeta\hat{\mathbf{e}}_z - \cos\zeta\hat{\mathbf{e}}_x, \quad \hat{\mathbf{e}}_{\perp i} = -\hat{\mathbf{e}}_y, \quad \hat{\mathbf{e}}_{\perp i} \times \hat{\mathbf{e}}_{\parallel i} = \hat{\mathbf{e}}_i \end{gathered}$$

and the scattered field in terms of cylindrical coordinates for a constant azimuthal angle ϕ ($\phi = 0°$ corresponds to backscattering) as follows

$$\begin{gathered} \mathbf{E}_s = E_{\parallel s}\hat{\mathbf{e}}_{\parallel s} + E_{\perp s}\hat{\mathbf{e}}_{\perp s}, \\ \hat{\mathbf{e}}_{\parallel s} = \cos\zeta\hat{\mathbf{e}}_r + \sin\zeta\hat{\mathbf{e}}_z, \quad \hat{\mathbf{e}}_{\perp s} = -\hat{\mathbf{e}}_\phi, \quad \hat{\mathbf{e}}_{\perp s} \times \hat{\mathbf{e}}_{\parallel s} = \hat{\mathbf{e}}_s. \end{gathered}$$

For normal incidence the amplitude scattering matrix equation (B.1) simplifies to

$$\begin{bmatrix} E_{\parallel s} \\ E_{\perp s} \end{bmatrix} = e^{i3\pi/4} \sqrt{\frac{2}{\pi k r}}\; e^{ikr} \begin{bmatrix} T_1 & 0 \\ 0 & T_2 \end{bmatrix} \begin{bmatrix} E_{\parallel i} \\ E_{\perp i} \end{bmatrix} \tag{B.2}$$

and becomes diagonal which means that there is no mixing between the two polarization directions. The matrix elements T_1 and T_2 are given as

$$\begin{aligned} T_1 &= b_0 + 2\textstyle\sum_{n=1}^{\infty} b_n \cos(n\Theta), \\ T_2 &= a_0 + 2\textstyle\sum_{n=1}^{\infty} a_n \cos(n\Theta) \end{aligned}$$

with $\Theta = \pi - \phi$ and he scattering coefficients are

$$\begin{aligned} a_n &= \frac{mJ_n'(x)J_n(mx) - J_n(x)J_n'(mx)}{mJ_n(mx)H_n^{(1)\prime}(x) - J_n'(mx)H_n^{(1)}(x)}, \\ b_n &= \frac{J_n(mx)J_n'(x) - mJ_n'(mx)J_n(x)}{J_n(mx)H_n^{(1)\prime}(x) - mJ_n'(mx)H_n^{(1)}(x)} \end{aligned}$$

where J_n and Y_n are the Bessel functions of first and second kind, $H_n^{(1)} = J_n + iY_n$ the Hankel functions, $m = N_1/N_2 = n + ik$ (k denoting here the absorption coefficient) the

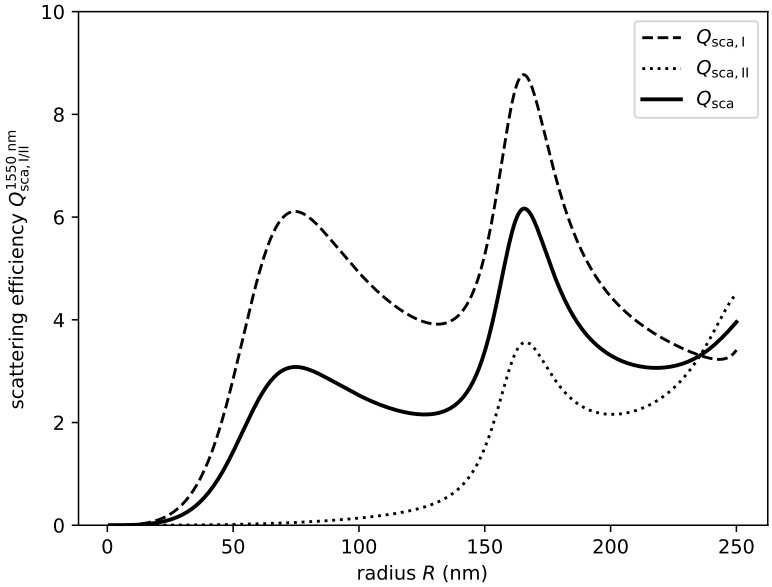

Figure B.1. – Scattering efficiencies $Q_{\mathrm{sca,I}}$, $Q_{\mathrm{sca,II}}$ and $Q_{\mathrm{sca}} = \frac{1}{2}\left(Q_{\mathrm{sca,I}} + Q_{\mathrm{sca,II}}\right)$ up to third order for the refractive index of Si ($n = 3.48 + 0i$) and a wavelength of $\lambda = 1550\,\mathrm{nm}$. At small radii compared to the wavelength only the first two orders contribute significantly and scattering is clearly enhanced if the polarization of the incoming light is aligned with the NW axis.

relative refractive index, $x = kR$ ($k = 2\pi/\lambda$), and λ the wavelength of the incoming light.

Knowing the scattered field one can compute the Poynting vector of the sum of incident an scattered field. It can be written as

$$\mathbf{S} = \mathbf{S}_i + \mathbf{S}_s + \mathbf{S}_{\mathrm{ext}},$$
$$\mathbf{S}_i = \tfrac{1}{2}\Re\left(\mathbf{E}_i \times \mathbf{H}_i^*\right), \quad \mathbf{S}_s = \tfrac{1}{2}\Re\left(\mathbf{E}_s \times \mathbf{H}_s^*\right), \quad \mathbf{S}_{\mathrm{ext}} = \tfrac{1}{2}\Re\left(\mathbf{E}_i \times \mathbf{H}_s^* + \mathbf{E}_s \times \mathbf{H}_i^*\right).$$

Integrating the scattered part $\mathbf{S}_s$ over a closed surface of length L around the cylinder, one gets the rate of energy absorbed by the surface per unit length as

$$W_s = RL \int_0^{2\pi} (\mathbf{S}_s)_r d\phi \tag{B.3}$$

From this the scattering efficiencies, normalized to the intensity I_i of the incoming light, are defined as

$$Q_{\mathrm{sca,I}} = \frac{W_{s,\mathrm{I}}}{2RLI_i} = \frac{2}{x}\left(|b_0|^2 + 2\sum_{n=1}^{\infty}|b_n|^2\right) \tag{B.4}$$
$$Q_{\mathrm{sca,II}} = \frac{W_{s,\mathrm{II}}}{2RLI_i} = \frac{2}{x}\left(|a_0|^2 + 2\sum_{n=1}^{\infty}|a_n|^2\right) \tag{B.5}$$

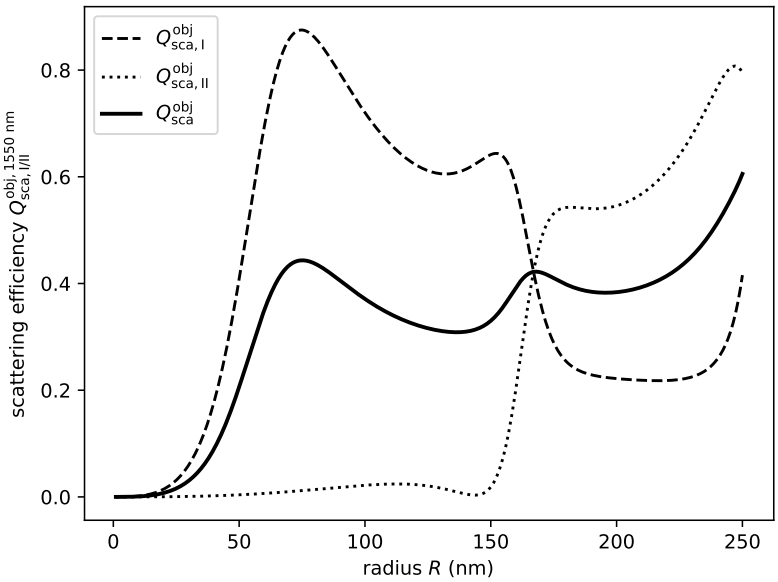

Figure B.2. – Integrated differential scattering efficiencies for our objective with an acceptance angle of 2α for the refractive index of Si ($n = 3.48 + 0i$) and a wavelength of $\lambda = 1550\,\mathrm{nm}$.

for normal incidence and the two cases of polarization. For unpolarized light the following holds

$$Q_{\mathrm{sca}} = \frac{1}{2}\left(Q_{\mathrm{sca,I}} + Q_{\mathrm{sca,II}}\right). \tag{B.6}$$

Another useful quantity can be found by looking at the integrand of B.3 and using equation (B.2) to identify the differential scattering efficiencies

$$\frac{dQ_{\mathrm{sca,I}}}{d\phi} = \frac{1}{\pi x}|T_1(\Theta)|^2 \tag{B.7}$$

$$\frac{dQ_{\mathrm{sca,II}}}{d\phi} = \frac{1}{\pi x}|T_2(\Theta)|^2. \tag{B.8}$$

Integrating the differential scattering efficiencies for backscattering over the acceptance angle $2\alpha = 2\arcsin(\mathrm{NA}) = 2\arcsin(0.44)$ of our objective from $\pi - \alpha$ to $\pi + \alpha$ results in Figure B.2. Clearly the backscattering is enhanced for NWs with radii below 150 nm for the polarization direction along the NW axis. As an example the same integrated differential scattering efficiencies are plotted in Figure B.3 for a wavelength of 635 nm and show a much richer dependence on the NW radius.

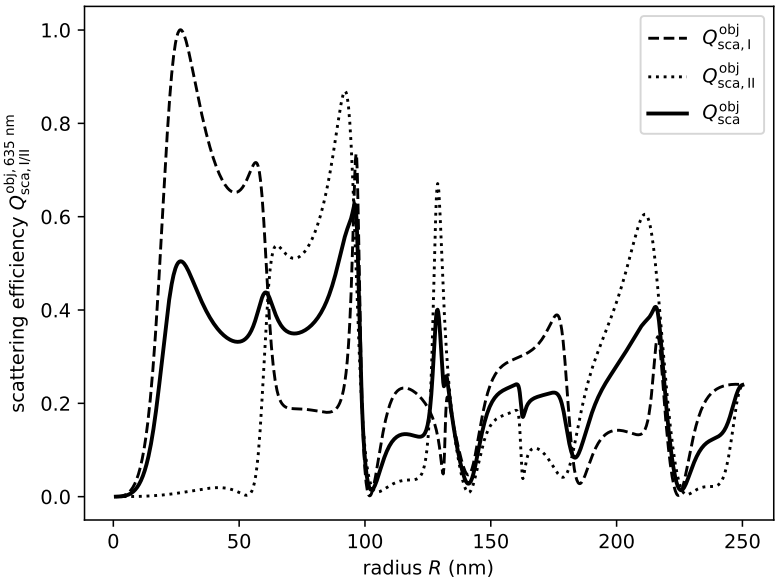

Figure B.3. – Integrated differential scattering efficiencies for our objective with an acceptance angle of 2α for the refractive index of Si ($n = 3.86 + 0.016i$) and a wavelength of $\lambda = 635\,\text{nm}$.

C. Biot-Savart field of a rectangular conductor

The magnetic field of an infinitely long conductor with rectangular cross section of width w, height h and a uniform current $I = j_y wh$ flowing in y-direction (see Figure C.1), where j_y is the current density along the y-direction, can be calculated using the two-dimensional Biot-Savart law

$$B_x(x,z) = \frac{\mu_0 I}{2\pi wh} \int_s \frac{z' - z}{[x' - x]^2 + [z' - z]^2} dS' \tag{C.1}$$

$$B_z(x,z) = \frac{\mu_0 I}{2\pi wh} \int_s \frac{x' - x}{[x' - x]^2 + [z' - z]^2} dS' \tag{C.2}$$

where S is its cross-sectional area. Solving the surface integrals with the center of the coordinate system aligned with the geometrical center of the conductor yields (see also Refs. [93, 94])

$$\begin{aligned} B_x(x,z) = \frac{\mu_0 I}{4\pi wh} \Bigg\{ & [w/2 - x] \log \frac{[w/2 - x]^2 + [h/2 - z]^2}{[w/2 - x]^2 + [h/2 + z]^2} \\ & + [w/2 + x] \log \frac{[w/2 + x]^2 + [h/2 - z]^2}{[w/2 + x]^2 + [h/2 + z]^2} \\ & + 2[h/2 - z] \left[\arctan \frac{w/2 - x}{h/2 - z} + \arctan \frac{w/2 + x}{h/2 - z} \right] \\ & - 2[h/2 + z] \left[\arctan \frac{w/2 - x}{h/2 + z} + \arctan \frac{w/2 + x}{h/2 + z} \right] \Bigg\} \end{aligned} \tag{C.3}$$

and a similar expression for $B_z(x,z)$.

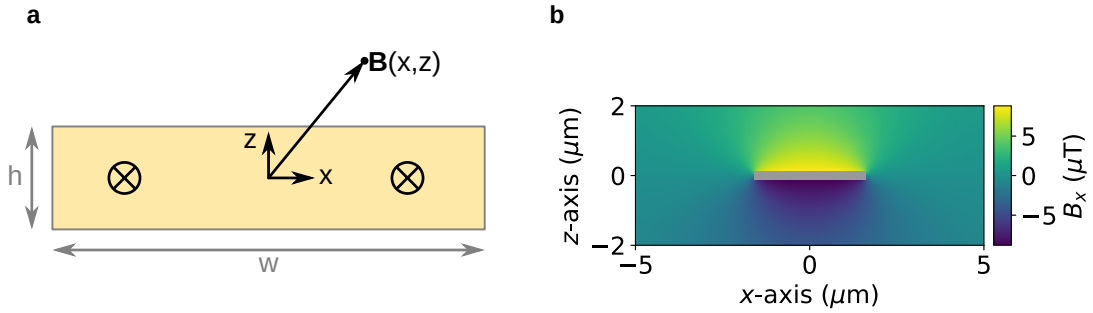

Figure C.1. – **Biot-Savart of a rectangular conductor**
a) Cross section of an infinitely long rectangular conductor with width w and height h. **b**) Plot of $B_x(x, z)$ according to equation (C.3) for $w = 3.2\,\mu\text{m}$, $h = 240\,\text{nm}$ and a current of $I = 47\,\mu\text{A}$.

D. Co FEBID NW

D.1. Data

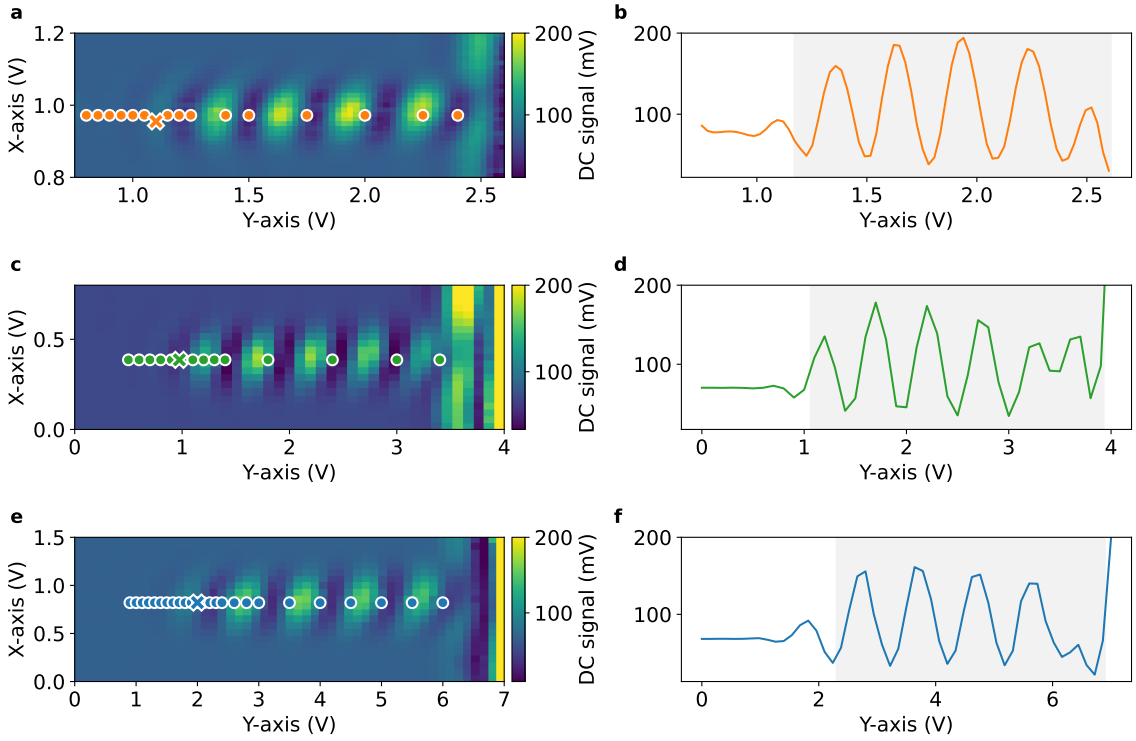

Figure D.1. – **Measurement positions at different temperatures**
a, **c**, **e** Scanning interferometer image of NW 4 at T_{bath} = 295, 77 and 4.2 K, with the spots marked at which the laser power dependence measurements are taken. The position marked by a cross (X) corresponds to the measurement position for the data shown in Figures D.2 and 3.6. Points correspond to measurement positions for data shown in Figure 3.8. **b**, **d**, **f** Line scan along the long axis of the NW. The gray box highlights the extent of the NW. Interference fringes are visible in the images because either the z-piezo scanner movement has a small additional component along the x-direction and/or the NW is tilted by a small amount with respect to the z-axis.

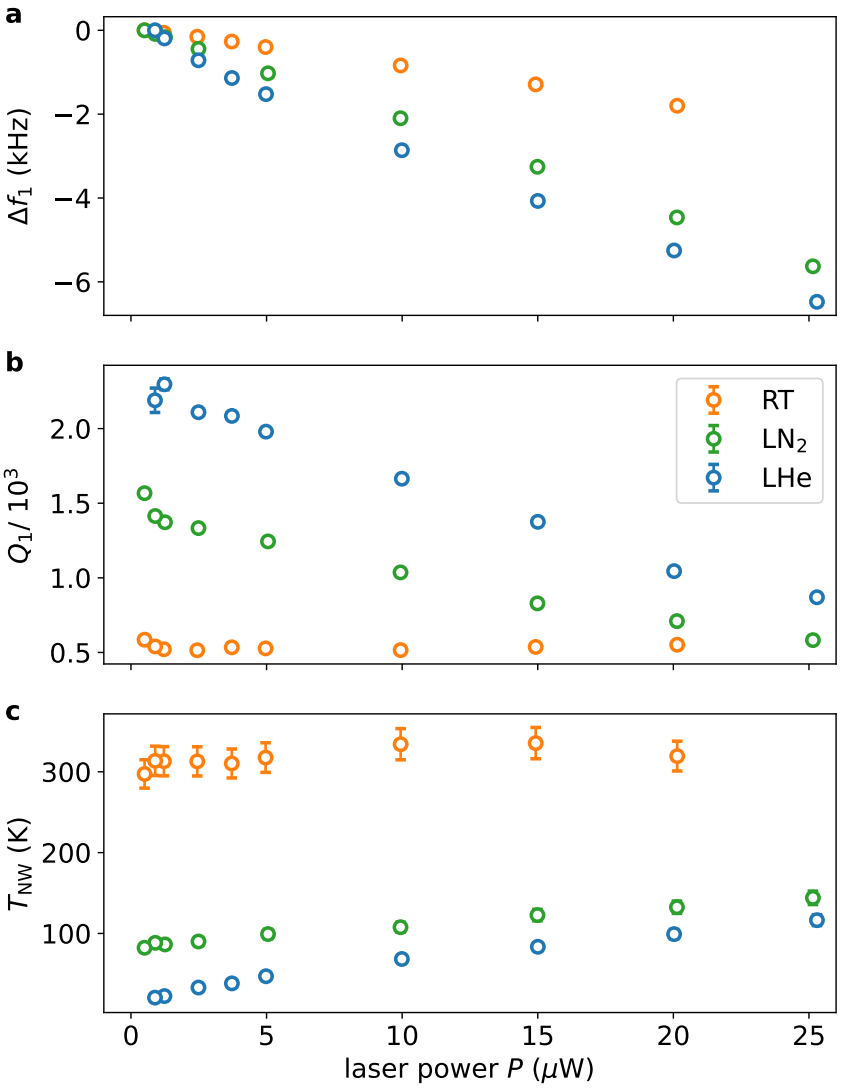

Figure D.2. – **Laser power dependence of mechanical properties**
Resonance frequency shift **a**, quality factor **b** and NW temperature **c** at $T_{\text{bath}} = 293\,\text{K}$ (orange), 77 K (green), and 4.2 K (blue) for different laser powers. These power dependences are measured with the laser aligned to the tip of the NW, corresponding to the cross (X) in Figure D.1 a.

E. Si NW

E.1. SEM

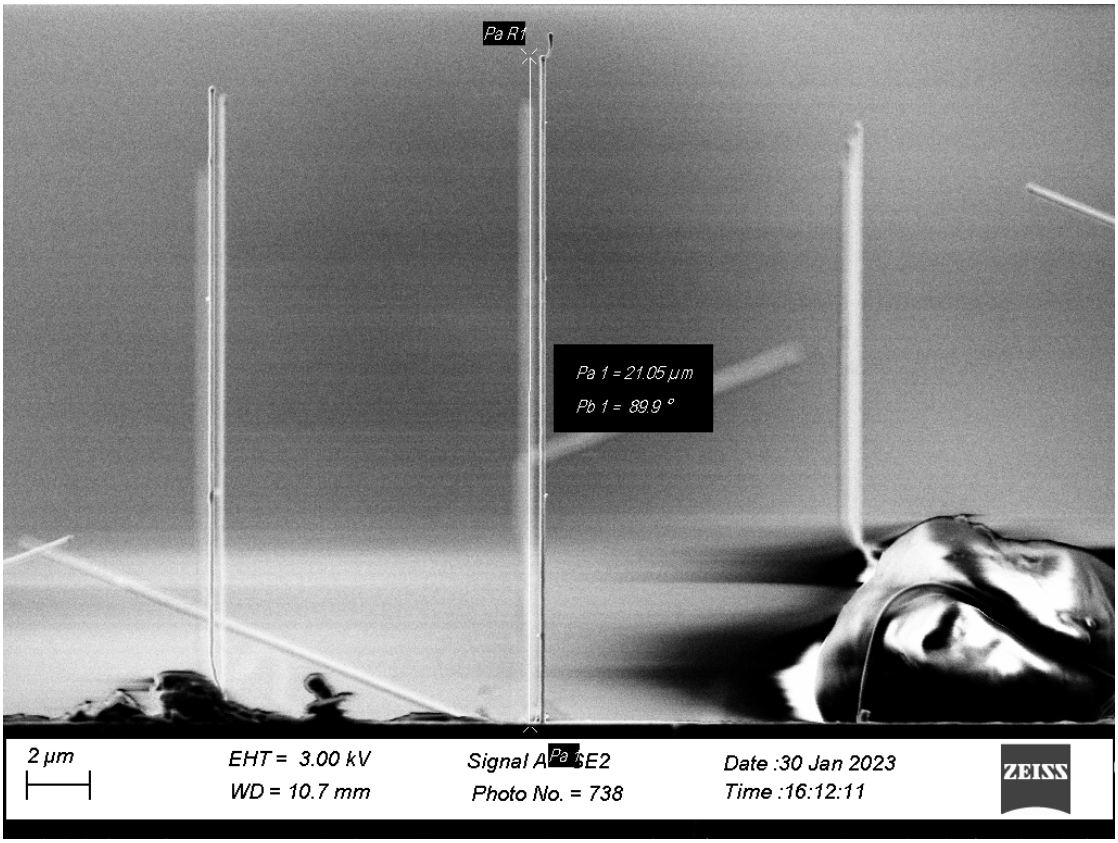

Figure E.1. – SEM of full NW with Co FEBID tip

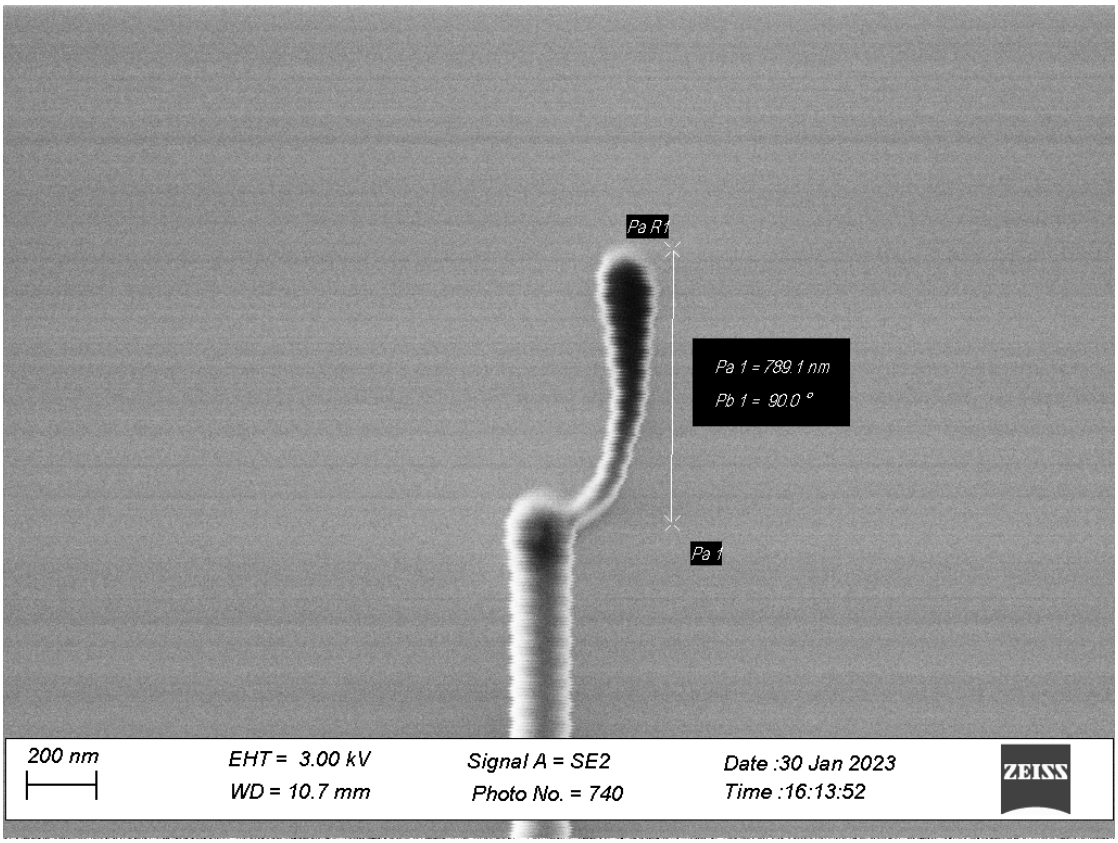

Figure E.2. – SEM of Si NW Co FEBID tip length

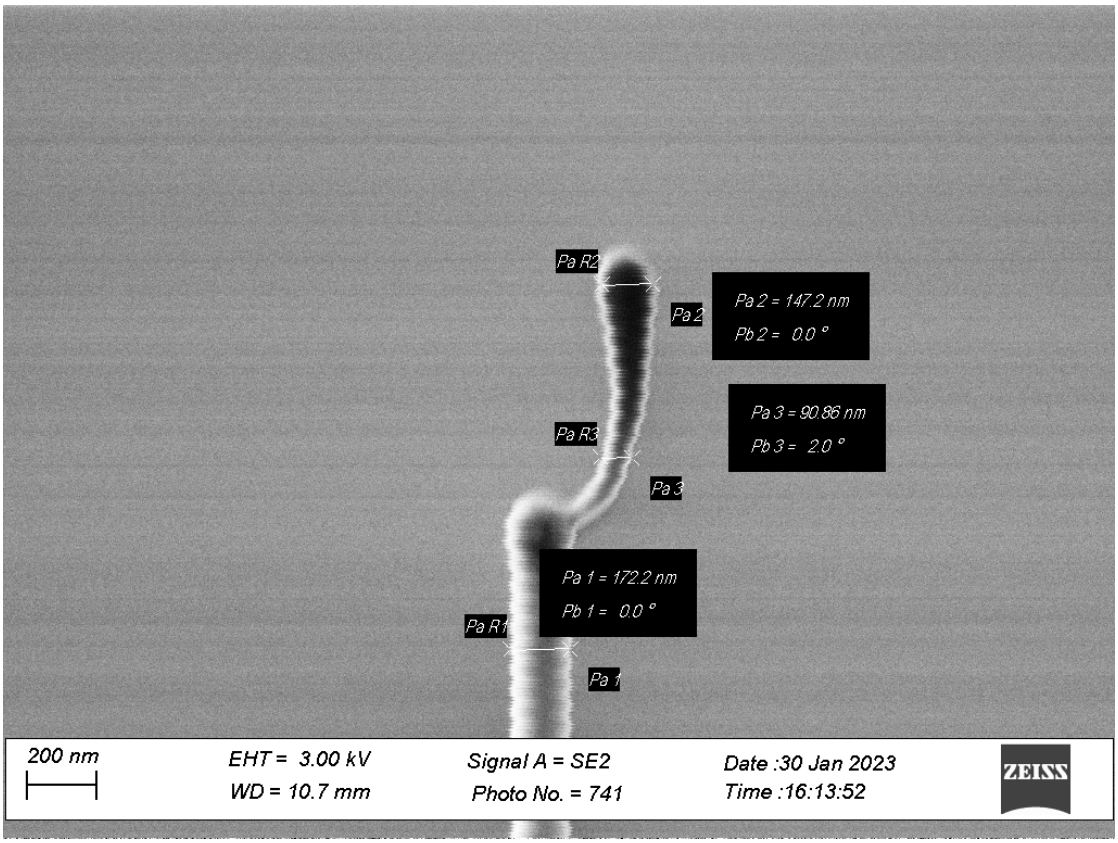

Figure E.3. – SEM of Si NW Co FEBID tip width

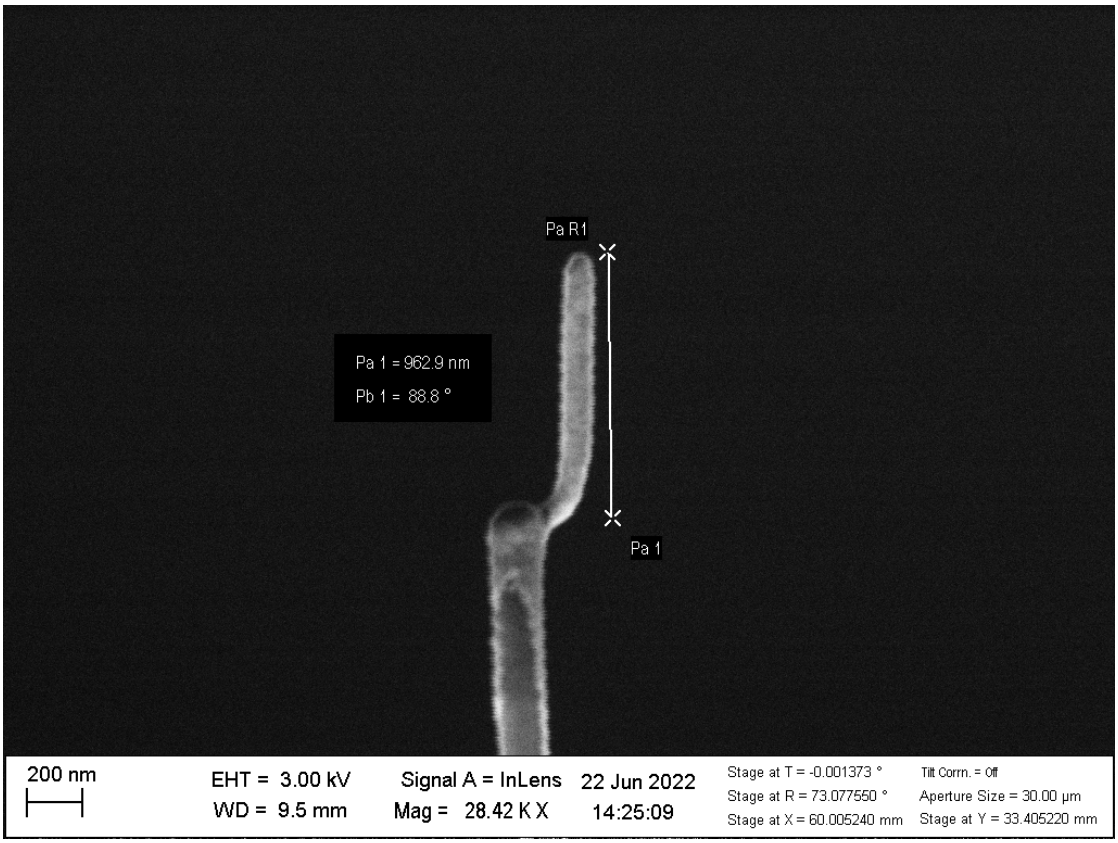

Figure E.4. – SEM of a different Si NW with Co FEBID tip showing side wall deposition

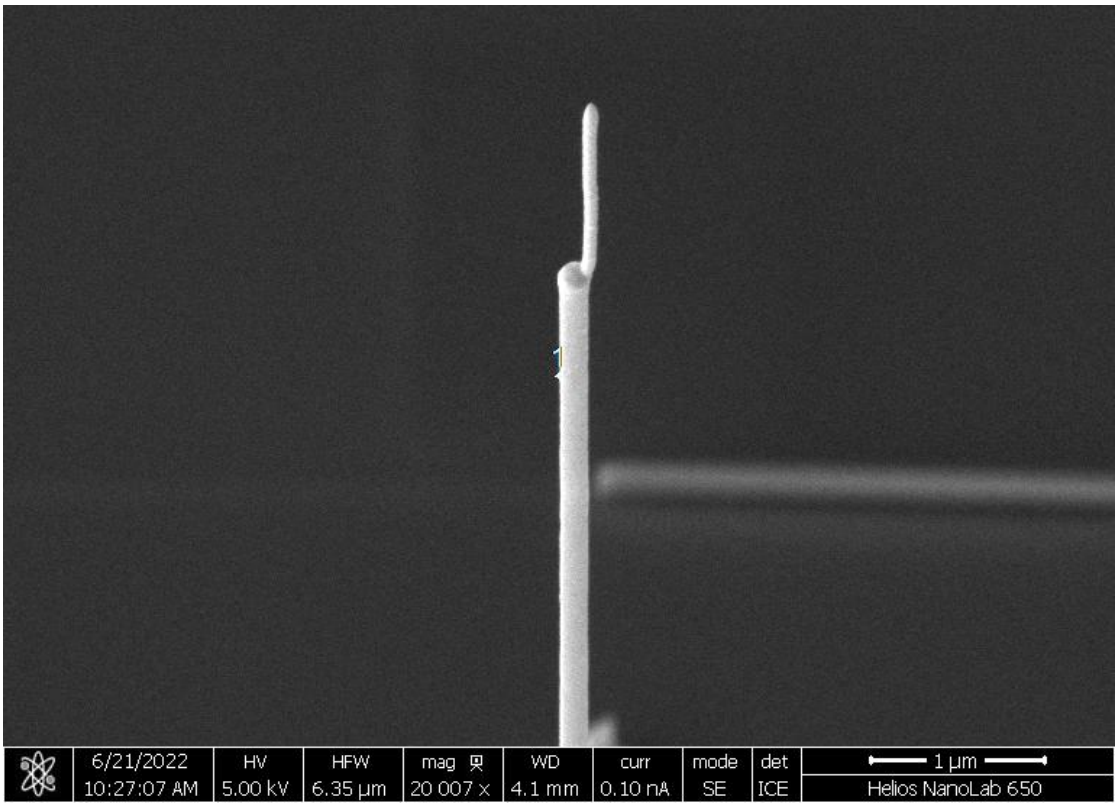

Figure E.5. – **SEM of a different Si NW with Co FEBID tip** This deposit was subject to the EDX measurement shown in the next page E.2 yielding a Co content of about 44 %.

E.2. EDAX

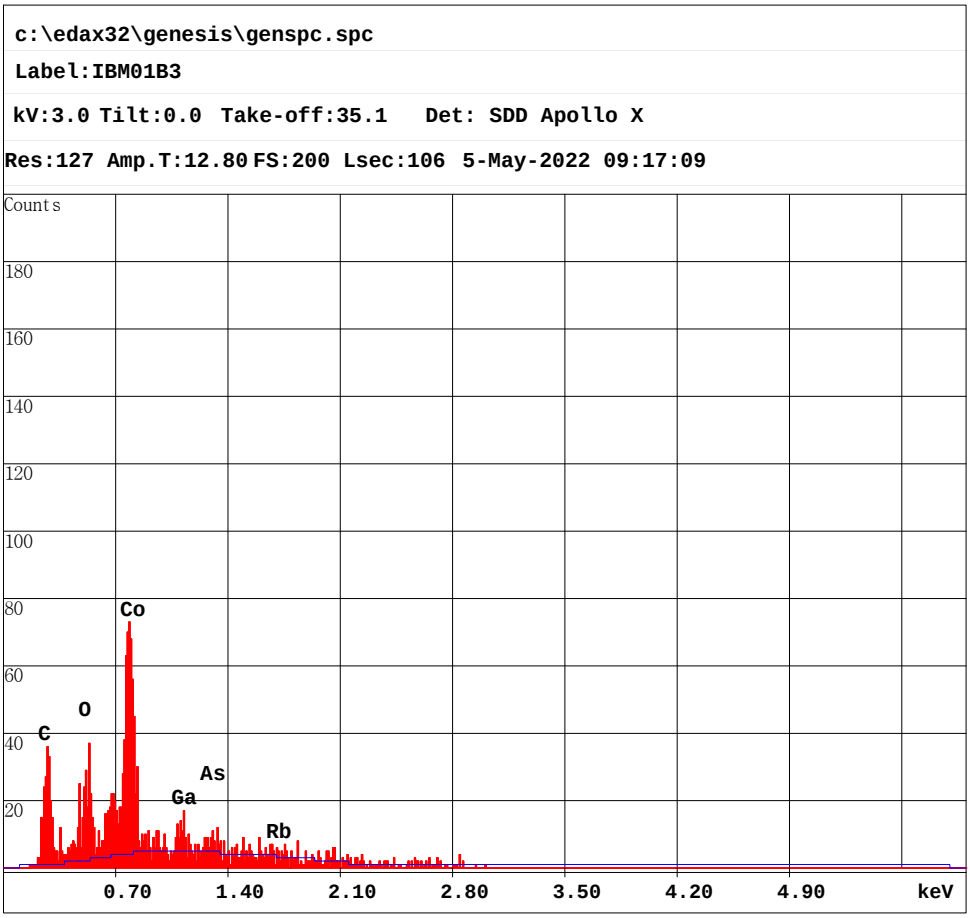

EDAX ZAF Quantification (Standardless)
Element Normalized
SEC Table : User D:\EDAX_Savecalib_21062012_install\SEC Genesis\BCNOF_21062012.sec

Element	Wt %	At %	K-Ratio	Z	A	F
C K	8.52	27.98	0.0895	1.3859	0.7574	1.0001
O K	7.51	18.52	0.0922	1.3427	0.9128	1.0011
CoL	65.53	43.85	0.6047	0.9409	0.9806	1.0002
GaL	7.52	4.25	0.0609	0.8777	0.9219	1.0002
AsL	5.60	2.95	0.0452	0.8530	0.9460	1.0001
RbL	5.31	2.45	0.0419	0.8057	0.9784	1.0000
Total	100.00	100.00				

Element	Net Inte.	Bkgd Inte.	Inte. Error	P/B
C K	1.27	0.05	8.92	27.00
O K	1.24	0.12	9.52	10.15
CoL	3.23	0.23	5.76	14.33
GaL	0.43	0.33	23.43	1.31
AsL	0.24	0.38	39.60	0.65
RbL	0.09	0.26	81.24	0.36

E.3. Data

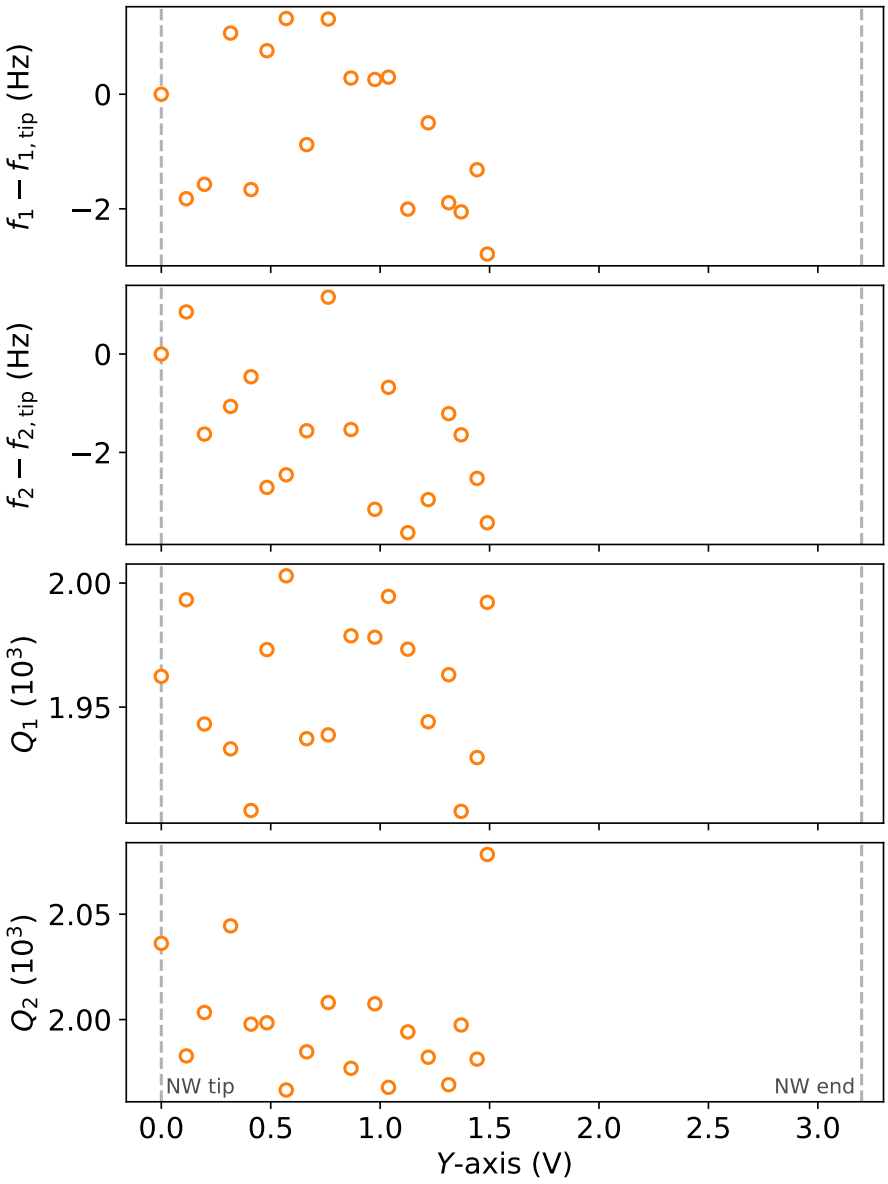

Figure E.6. – **Si NW along axis at room temperature**
No influence of the tip position is found on the mechanical NW properties.

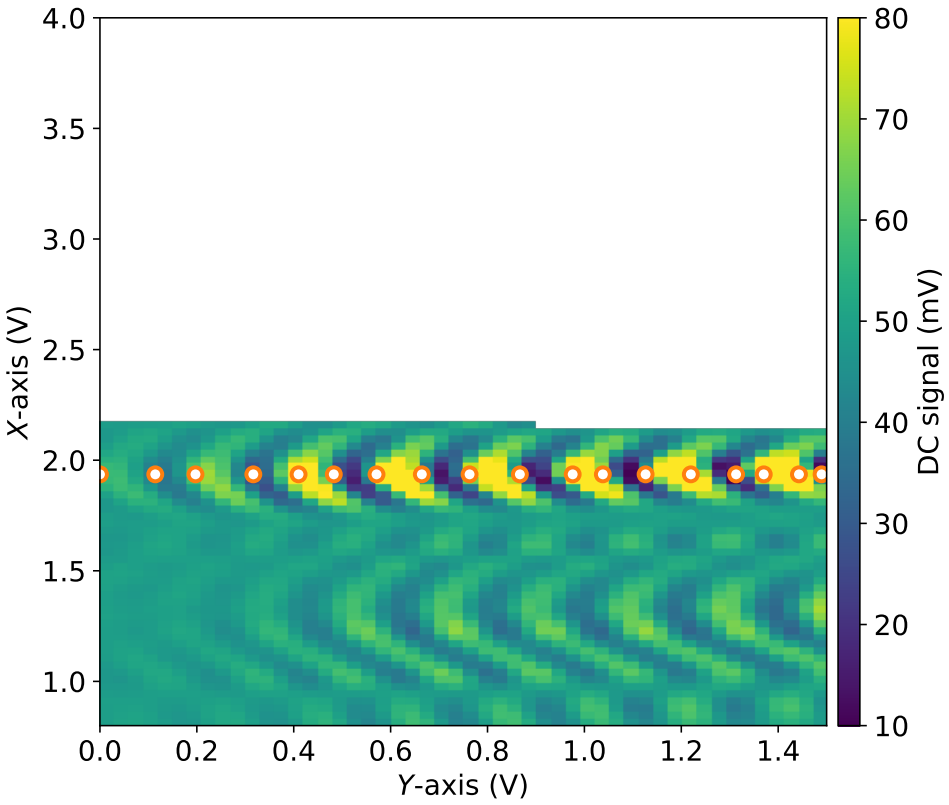

Figure E.7. – Interference image of Si NW at room temperature
Marked are the points at which the thermal noise PSDs are taken for the data in Figure E.6.

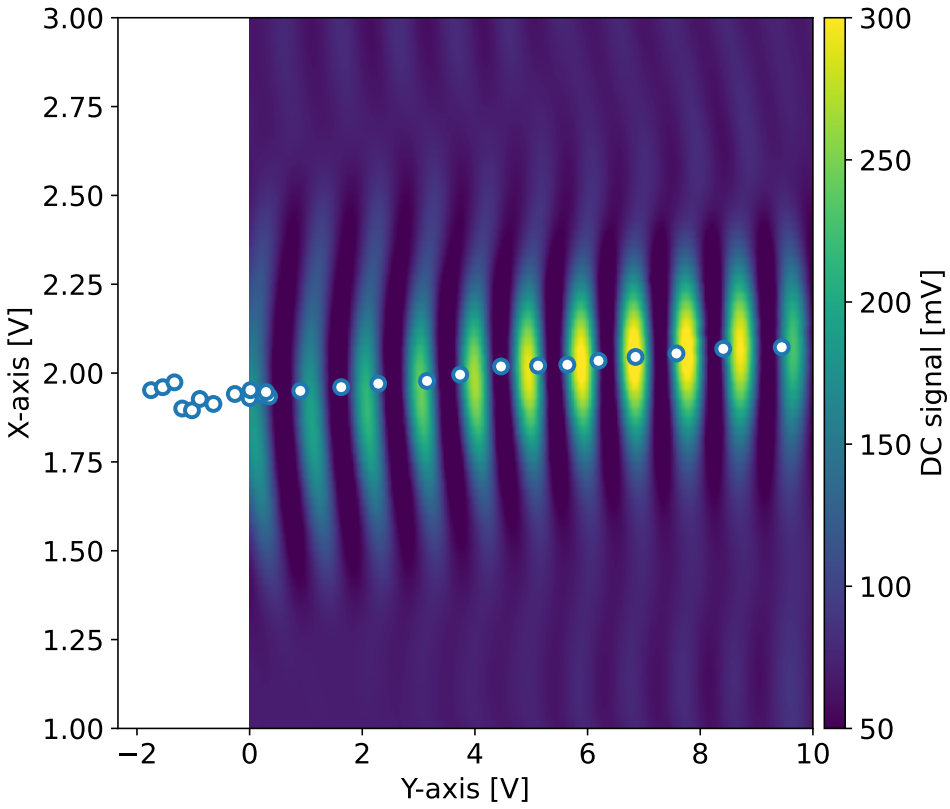

Figure E.8. – **Interference image of Si NW at LHe temperature**
Marked are the points at which the thermal noise PSDs are taken for the data in Figure 3.10. The offset at 0 V is due to stepping and stitching since the NW length exceeded the range of the piezo-positioner.

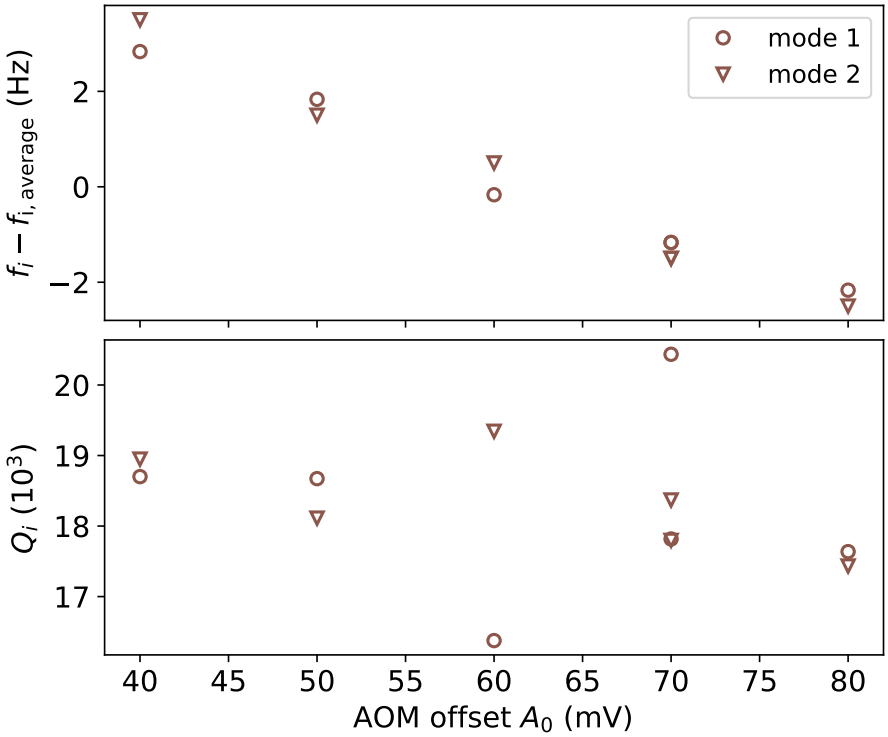

Figure E.9. – **Laser power dependence at the working point at LHe temperature**

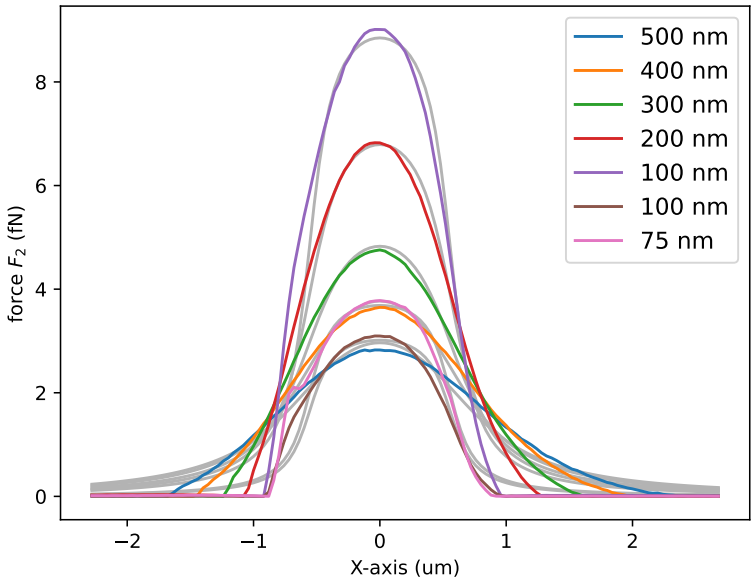

Figure E.10. – Biot-Savart tip calibration for Si NW with Co FEBID tip Measured resonant Biot-Savart field profiles at different tip sample distances (color). In grey are the fits according to the Biot-Savart field profile of a rectangular conductor, using only the monopole term of the point pole force expansion. The fits directly reveal q_{tip} and the monopole offset Δz_{mono} which are shown in Figure 3.14 for the different tip sample distances.

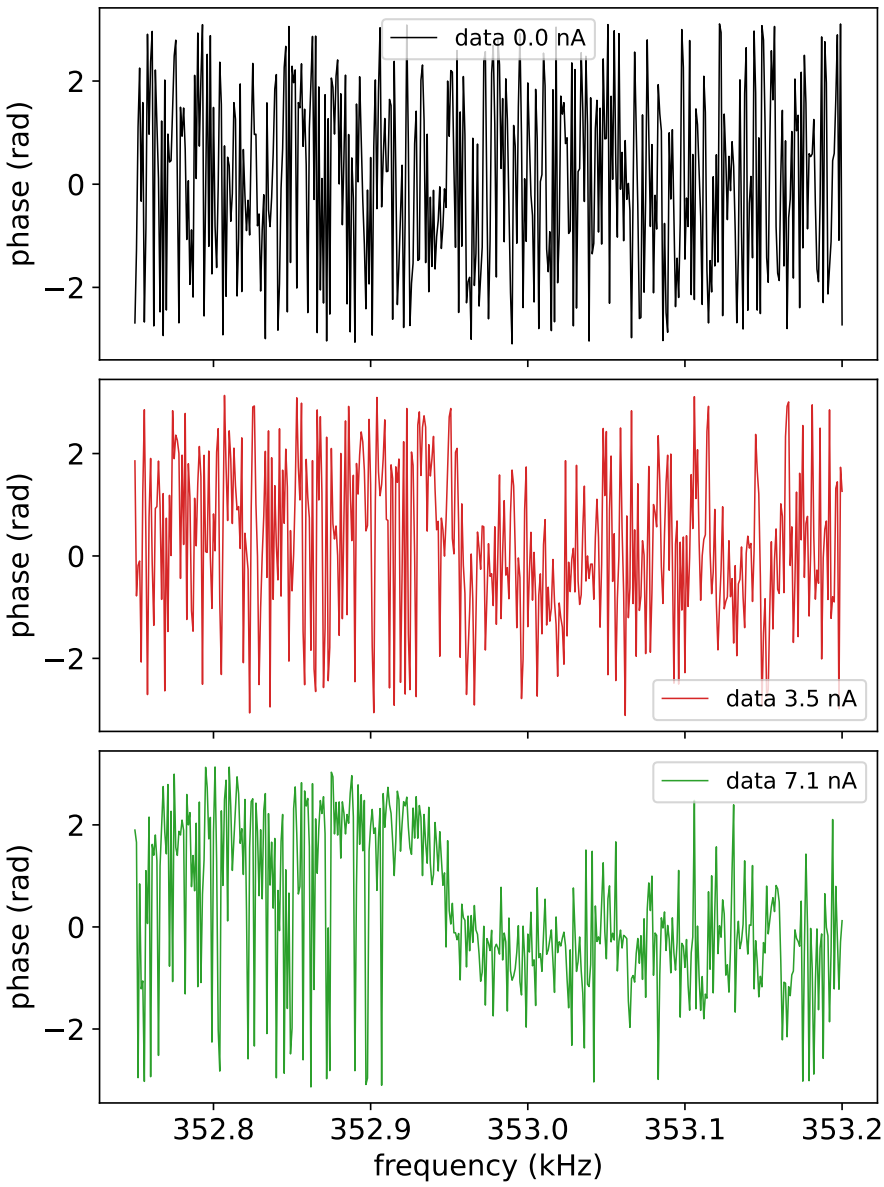

Figure E.11. – Phase data of the sweeps used to determine the current sensitivity
Shown is the phase data of current sweeps for values of the Biot-Savart current of 0.0, 3.5 and 7.1 nA. Passing no current the phase is entirely randomized. With rising current it becomes more coherent and the characteristic π-shift across the resonance emerges.

Acknowledgements

First and foremost I would like to thank Prof. Martino Poggio for the possibility to conduct my research in the Poggio Lab. His extraordinary support over the past couple of years was invaluable on so many levels. Thank you also to Prof. Richard Warburton for being my second supervisor and Dr. Thomas Mühl for completing my doctoral committee as external referee.

Of course, my PhD thesis would not have been possible without the assistance, backing and encouragement of the people at Poggio Lab. When I joined the nanowire team it consisted of Nicola and Davide, both of whom started off the project with incredible pioneering work. Among their excellent scientific inputs I have great memories of Nicola teaching me the in and outs of clearing out nanowire forests and praying to the LightField gods for support with Davide. Later on Lukas joined the NW team, first as Master student later as fellow PhD candidate. His persistence and originality helped tremendously to push the project forward. Lukas, it was a pleasure working with you. Furthermore I would like to thank Boris for his laid-back attitude and great support regarding micromagnetic simulations and Francesco for his expertise in many fields (not only NWs) and always taking the time for fruitful discussions.

Special thanks go out to Giulio, my long-time desk and cycling mate. Initiated by Nicola to the road cycling world, the three of us would roam the streets around Basel[1] on countless occasions, enjoying beautiful summer sunsets or almost loosing extremities during the winter months. Moreover I have to mention the support of Estefani, who was always around with a helping hand and Floris with his uncomplicated way and genuine interest in the NW project. Marcus deserves a special shout-out for welcoming me warmly into the group, furious squash and badminton battles and his outstanding assistance with FEBID at the Nano Imaging Lab. David is entitled to a special mentioning for sharing his deep knowledge about mechanical resonators and his support during the writing process, being on the same schedule as myself. Additionally I want to cordially thank the rest of the former Poggio Lab, that is Lorenzo, Thibaud, Simon, and overlapping by just two weeks Denis, as well as the present line-up Kousik, Andriani, Daniel, Luca, Mathias, Liza, Aurèle, and Aris for a wonderful time and a great collective spirit. May your research be always successful in the future!

Many collaborations have been set up during the time of my PhD, which were absolutely essential to my work. In-house I had the great pleasure to learn everything about 2D vdW materials fabrication from Nadine Leisgang. Even though our efforts proved to be a bit too ambitious at that time, they were vital to realize the shortcomings of our system and put the experiment in the state that it is now. I am especially proud

[1] Big thanks also to the members of the infamous KGB

of the method we have developed for stacking vdW structures close to 5 µm of a chip edge. Next up in Basel I have to thank Patrick Reiser for openly sharing his knowledge about and samples of $EuGe_2$ in what would become a productive cooperation on shining light onto the magnetism of this material system from different angles. Outside of Basel Prof. José María de Teresa and his expertise in FEBID sparked the whole project of magnetic NW probes for imaging and his contributions were priceless to our efforts. In the same way Prof. Raffi Budakian's more than excellent Si NWs enabled the way to the most sensitive magnetic NW probes ever build in our lab. Without these two contributions my project would not have been possible.

Additionally, I have to acknowledge the magnificent support from the infrastructure teams. In particular Sascha Martin and his team from the mechanical workshop materialized all our imagined and sometimes too dreamy probe parts in no time and with absolute precision and provided liquid helium whenever needed. Gerard Gadea and Arnold Lücke offered the fundamental service of a functioning clean room and in administrative matters Claudia Wirth – charming as ever – took care of things before you even would notice.

During my time at the Physics Department I have been lucky to meet a lot of wonderful people, among them Martin, Olivier, Carlo, Diego, the Warburton group and many others, who majorly contributed to creating a beautiful and unforgettable atmosphere during and especially outside of working hours. Thank you for that. Aside from university a special thank you has to go to the 3-Rosen X-fit crew[2] and my fieldhockey team, the Basler Hockeyclub, for providing ample of opportunity to relieve stress and see things from a different perspective. On the same note thanks Martino for all the morning track sessions.

Finally, with the warmest regards, I want to thank my friends Marlen, David (×2), Martina, Flaviano, Nadine, Jonathan, Elena, Eric, Saskia, Denes, Alain, Nina, Sven, Leonie, Max, Sara and Rebi for standing by my side throughout the past years. Last but not least I am eternally grateful to my family for their unconditional love and support as we navigated our way through the ups and downs of the recent past. I want to close with the person nearest to me, always cheering me up and bringing a smile to my face. Thank you, Nadège.

— *Hinrich*

[2] You guys are awesome!